CONSTRAINING ABOVE- AND BELOWGROUND UNCERTAINTIES IN TROPICAL MONTANE BIOGEOCHEMISTRY

A DISSERTATION
SUBMITTED TO THE FACULTY OF THE GRADUATE SCHOOL
OF THE UNIVERSITY OF MINNESOTA
BY

Nathaniel T. Looker

IN PARTIAL FULFILLMENT OF THE REQUIREMENTS
FOR THE DEGREE OF
DOCTOR OF PHILOSOPHY

Advisors Randy Kolka and Ed Nater

August 2021

Acknowledgements

This dissertation was made possible by the generous support and enthusiasm of my colleagues, collaborators, friends, and family in Mexico and the US over the course of five years. The following is an incomplete list and an understatement of my gratitude to each and every one of these individuals and institutions.

Thanks to my co-advisors, Randy Kolka and Ed Nater, and committee members, Heidi Asbjornsen, Stephen Sebestyen, and John Baker, for your trust, patience, and guidance as my effort to understand soils led me across disciplines and spatial scales, from my first field surveys of soil hydrophysical properties to my later lab forays into environmental magnetometry and density fractionation. I am deeply grateful for the time and resources you have invested in my education, and I look forward to continuing our collaborations in the coming years. Extra thanks to Heidi, both for kickstarting my research career as an undergraduate at Iowa State and for the invitation to join the CH2ILES project that initially brought me to Veracruz.

Mil gracias a los propietarios y otros habitantes de la cuenca del Río Pixquiac. Estas investigaciones se llevaron a cabo gracias a su apoyo, y dependieron mucho de los conocimientos que me compartieron. En particular, les quisiera agradecer a Claudia Gallardo Hernández, Don Luis, Doña Leticia, Don Félix, Don Felipe, Don Honésimo, Don Camerino, Doña Clara, Don Lucio, Don Demetrio, Don Crispín, Don Juan, y los varios dueños de los cerros de piedra caliza por darme la oportunidad de conocer su paisaje tan único. Nosotros que estamos rodeados de los monocultivos de maíz y soya tenemos mucho que aprender de su ejemplar manejo integral de los recursos.

Gracias también a los amigos que trabajaron juntos conmigo en campo y después en el manejo de las muestras infinitas. Gracias especiales a Mariana Quetzalli Vizcaíno Bravo por enseñarme tanto y por tener la mejor actitud en todas la condiciones (hasta en las sesiones de terapia de zarzamora). Les agradezco también a Perla Ortiz Colín, Aspen Ward, León

Gómez Aguilar, Alonso Cortés-Pérez, Marcos Carmona Saldaña, Benny Carmona Saldaña, Carlos Lezama, Valérie Tchang, Jorge Cortinas, Jenny Morales Baizabál, y Karen Fabre. Qué afortunado me siento haber podido convivir con ustedes allá en la media montaña.

Many thanks to my friends and collaborators whose work informed and complemented mine spatially and thematically: Sergio López Ramírez, Juan José Von Thaden Ugalde, Pierre Mokondoko Delgadillo, Humberto Romero Uribe, Gina Vidriales Chan, Luisa Paré, María Luisa León, Susana Alvarado Barrientos, Robert Manson, Gina Zapet, Claudia Gallardo Hernández, Lupe Williams-Linera, Daniel Geissert, Isabelle Barois, Sandra Rocha Ortíz, Ninfa López Portilla, Lourdes Cruz Huerta, Rosario Landgrave Ramírez, Victor Vásquez Reyes, Javier Tolomé, Adolfo Campos C., Beatriz Marín Castro, Patricia Gerez Fernández, Lyssette Muñoz Villers, Friso Holwerda, Sophie Ávila Foucat, David Torrez, Jake Salcone, Carter Berry, Xoco Shinbrot, Erin Pischke, Theresa Selfa, Alex Mayer, Leo Sáenz, Andrés Urcuqui Bustamente, Kelly Jones, Carmen Maganda, Harlan Koff, Russ Congalton, Diana Cordoba, Shadi Atallah, and Catherine Ashcraft. Thanks for sharing your experiences and perspectives. It's been a great privilege to work with you all.

Gracias a la Toña y a toda la familia Berruezo por cuidarme y aceptarme como un hijo más. Será un honor recibirlos en casa algún día pronto.

Gracias a Doña Rebeca y Doña Rosa por proporcionarme el regalo de Mayahuel, y a Valeria, Mike, y toda la banda de la Brújula por sus obras y por el ambiente que han construido.

I can't begin to thank all of the friends who kept me afloat during my time at the University of Minnesota, but I must make an attempt. Heartfelt thanks to my classmates, especially Persephone Ma, Adrian Wackett, Kat Labine, Jennifer Nicklay, Benja Davies, Al Lohese, Tyler Nigon, Tamás Varga, Mike Sousa, Hava Blair, Caroline Pierce, Leanna Leverich, Cadan Cummings, and Jon Alexander, and to my friends at the U beyond SWAC, including Sharon Perrone, David Burge, Maggie Shanahan, Mara McPartland, Héctor Morales, Dylan Piatt, Mariana Walther, Joe Kendrick, and Cam Meyers. Thanks, too, to Charlie Elverson. I hope there are some exquisite mountains wherever you are now.

Thanks to my friends and housemates Dave Kelly, Phill Anton, Heather Winter, Nancy Douglas, Leigh Douglas, and Don Washington for sustaining me during the most stressful phases of writing and for tolerating much heavy sighing.

Many, many thanks to Kari Jarcho, Carl Rosen, Marjorie Bonse, Nicole Jones, Dylan Millet, David Mulla, and Stacy Nordstrom for your tireless assistance, especially for helping me

navigate the administrative dimensions of academia.

Thanks to the team of exceptional undergrads who worked alongside me in the lab: Cole Stenberg, Matt Lundberg, Claire Benton, Eli Craine, Ethan Barton, and Wystan Duhn.

Thanks to the University of Minnesota faculty and staff who lent me a hand, inspired my work, and took the time to brainstorm with me: Chad Babcock, Nic Jelinski, Jessica Gutknecht, Carol Loopstra, Brandy Toner, Kyungsoo Yoo, Jay Bell, Brent Dalzell, Diana Karwan, Xue Feng, Josh Feinberg, Dario Bilardello, Mike Jackson, and Peat Solheid.

Thanks to the team at the Center for Accelerator Mass Spectrometry at Lawrence Livermore National Laboratory, especially my mentor, Karis McFarlane, as well as Kimber Moreland, Irene Tunno, Tayor Broek, Kari Finstad, Allegra Mayer, Susan Zimmerman, and Tom Brown. I was incredibly fortunate to have the chance to work with you all as my Ph.D. drew to a close, and I deeply appreciate the energy you invested in my success.

Thanks to my collaborators Andrew Margenot at the University of Illinois Urbana-Champaign, Alain Plante and Liz Williams at the University of Pennsylvania, and Esperanza Muñoz Salinas and Miguel Castillo at la Universidad Nacional Autónoma de México for their critical contributions to projects related to the work featured here.

Thanks to my partner, Juliana, to my parents, Dan and Joan, to my sisters, Colleen and Maureen, and to the rest of my family for your relentless support and compassion.

This work was financially supported by National Science Foundation Coupled Human and Natural Systems Grant No. 1313804, NSF Graduate Research Fellowship Grant No. DGE-1049562, the Graduate Research Opportunities Worldwide Program jointly sponsored by the NSF and CONACyT (Mexico), the University of Minnesota Doctoral Dissertation Fellowship, and the Department of Energy Office of Science Graduate Student Research Program.

Dedication

To Ellen Eleanor Looker and Katie and Maddie Kieffer

Abstract

Sustaining water resources and soil organic carbon (SOC) storage in the face of global change requires understanding how vegetation and soils function across landscapes. Field-based characterization of vegetation and soils is increasingly complemented or substituted by the use of satellite imagery or geospatial products derived from statistical models. This dissertation comprises three studies presenting strategies for drawing inferences on vegetation and soils from field-, satellite-, and model-based sources of information while quantifying associated uncertainties and biases. All studies focused on a mountainous region in central Veracruz, Mexico.

The first study evaluated parameter uncertainty in satellite-based analysis of the seasonality, or phenology, of tropical montane vegetation. Phenological parameters and uncertainties were estimated using imagery with high spatial resolution (5 m) but low temporal resolution. The double-logistic phenology model performed well for cloud forest vegetation but poorly characterized the dynamics of other land-cover types, as reflected in large parameter uncertainties. Significant trends were detected in cloud forest phenology across gradients of topoclimate and forest composition. Accounting for parameter uncertainty was critical to the unbiased quantification of these trends.

The second study assessed potential improvements in landscape-specific SOC predictions through the integration of regional-to-global statistical models and local soil data. Off-the-shelf models underestimated SOC stocks by a factor of three, on average. Calibration using local soil data included within global databases corrected this linear bias, while calibration using a more representative dataset corrected disproportionate underestimation in SOC storage hotspots. The calibration approach permitted joint prediction of top- and subsoil SOC storage and can accommodate auxiliary field data to reduce prediction uncertainties.

The third study quantified bias in SOC stocks and radiocarbon activity due to soil volume change across land-use gradients, using novel and existing approaches to estimate volume

change. Ignoring volume change associated with deforestation and grazing inflated SOC stocks and introduced a previously unrecognized negative bias in radiocarbon activity, causing SOC appear to older. *Post hoc* adjustments for volume change, using the same data required to calculate SOC stocks, may improve confidence in estimates of land-use impacts on SOC dynamics.

Collectively, these results underscore the importance of accounting for uncertainty when integrating multiple information sources to characterize the spatial and temporal heterogeneity of vegetation and soils in complex landscapes.

Table of Contents

List of Tables

List of Figures

List of Abbreviations and Symbols

$\mathbf{^{14}C}$ radiocarbon

$\alpha_{\mathbf{1}}$ seasonal minimum EVI

$\alpha_{\mathbf{2}}$ seasonal amplitude of EVI

$\alpha_{\mathbf{3}}$ maximum greenup rate

$\alpha_{\mathbf{4}}$ greenup inflection point (day of maximum greenup)

$\alpha_{\mathbf{5}}$ mid-growing season EVI slope

$\alpha_{\mathbf{6}}$ maximum senescence rate

$\alpha_{\mathbf{7}}$ autumn inflection point (day of maximum senescence)

$\mathcal{B}$ beta distribution

δ day of year on which spring and autumn phenology functions are equal

$\mathbf{\Delta^{14}C}$ ratio of ^{14}C to ^{12}C corrected for mass-dependent fractionation and expressed relative to decay-corrected OX1 standard

Δz_i thickness of soil layer i

ϵ strain (proportional volume change)

σ^2 error variance

$\mathbf{A_t}$ autumn phenology function (EVI on day *t* in autumn)

AI aridity index (ratio of mean annual potential evapotranspiration to mean annual precipitation)

Al_o oxalate-extractable aluminum

AVHRR Advanced Very High Resolution Radiometer

$c_{x,i}$ mass fraction of soil component *x* in layer i

CMS NASA Carbon Monitoring System

EoS end of growing season

ESM equivalent soil mass

EVI enhanced vegetation index

FAO Food and Agriculture Organization of the United Nations

Fe_d dithionite-extractable iron

Fe_o oxalate-extractable iron

$\bar{g}_x$ mass-weighted mean of mass-normalized variable g

G_t phenology step function (EVI on day of year *t*)

GSL growing season length

GSOCmap Global Soil Organic Carbon Map

H' Shannon-Wiener index

I_x cumulative inventory of soil component *x* from the soil surface to a specified depth

INEGI Instituto Nacional de Estadística y Geografía

ISRaD International Soil Radiocarbon Database

ISRIC–World Soil Information International Soil Reference and Information Centre

LSP land surface phenology

LUC land-use change

MAP mean annual precipitation

MAT mean annual temperature

MCMC Markov chain Monte Carlo

MODIS Moderate Resolution Imaging Spectroradiometer

NIR near–infrared

OM organic matter

$\mathbf{p_{decid}}$ abundance-weighted proportion of deciduous tree species

$\mathbf{P_{ret}}$ phosphorus retention

PTF pedotransfer function

pXRF portable X-ray fluorescence

RMSE root-mean-square error

$\mathbf{S_t}$ spring phenology function (EVI on day t in spring)

$\mathbf{S_{x,\,i}}$ stock of soil component x in layer i

$\mathbf{Si_o}$ oxalate-extractable silicon

SOC soil organic carbon

SoS start of growing season

sPCA sparse principle components analysis

sPLS sparse partial least squares

SRE spatial random effects

Ti titanium

Unif uniform distribution

$\mathbf{V_{ref}}$ volume of a reference soil assumed to have undergone no volume change

$\mathbf{V_{str}}$ volume of a soil that has undergone volume change

WoSIS World Soil Information Service

$\mathbf{z_{ExM}}$ depth in a soil that has undergone volume change at which the cumulative mass inventory of soil component x is equal to the inventory of x at a specified depth in a reference soil that has not undergone volume change

$\mathbf{z_{nom}}$ nominal depth for comparisons across soils

Zr zirconium

Chapter 1

Introduction

Globally, montane landscapes play a disproportionate role in providing ecosystem services. Montane ecosystems store vast amounts of organic carbon in biomass and soils (Ward et al., 2014; Cuni-Sanchez et al., 2021) and generally serve as net carbon sinks (Fehse et al., 2002; Boisvenue & Running, 2010; Oliveras et al., 2014). In terms of biodiversity, 85% of mammal, bird, and amphibian species (Rahbek et al., 2019) reside in montane regions, though mountains only occupy 25% of the terrestrial surface (Meybeck et al., 2001). Montane catchments are critical sources of freshwater for human society: between the approximately one billion people living in montane areas (Körner et al., 2017) and the inhabitants of downstream lowland areas, more than half the global population relies on water flowing from mountains (Ariza et al., 2013). At low latitudes, greater water availability, milder temperatures, and greater soil fertility can make montane landscapes hotspots of crop and livestock productivity relative to surrounding lowlands (Massawe et al., 2017; Minda et al., 2018).

Predicting the effects of changes in land use and climate on ecosystem service provision in montane landscapes requires understanding the spatial variation of vegetation and soil functioning (Turner et al., 2012; Mokondoko et al., 2018; Liu et al., 2019; Berry et al., 2020). Substantial spatial heterogeneity in vegetation and soil characteristics is driven by biophysical variables that often vary profoundly over relatively short distances (e.g., 1 m–10 km) in montane landscapes. Sharp gradients in energy and water availability set the stage for much of this variation (Pelletier et al., 2013). Elevation and the morphology and orientation of the land surface mediate incoming solar radiation and hydroclimate, giving rise to patterns in vegetation composition, structure, and productivity, (McNab, 1989; Toledo-Garibaldi & Williams-Linera, 2014; Rasmussen et al.,

2015; Martin et al., 2017), microbial activity (Whitaker et al., 2014; Nottingham et al., 2019), and soils and landforms (Egli et al., 2003; Green et al., 2006; Vacca et al., 2009; Dixon et al., 2009; Rasmussen et al., 2017). Natural and anthropogenic disturbances may amplify, dampen, or reconfigure altitudinal and topoclimatic patterns, imparting additional complexity to some biophysical variables and homogenizing others (Kuriakose et al., 2009; Chaplot et al., 2009; Sierra & Causeret, 2018; Nolè et al., 2018; Minor et al., 2019). The effects of anthropogenic and biophysical factors on vegetation and soils are likely to be especially intertwined in regions where the majority of the population lives in high-relief areas, such as Mexico and Central America (Restrepo & Alvarez, 2006).

Satellite imagery and geospatial products derived from statistical models have emerged over recent decades as powerful tools for characterizing vegetation and soils from landscape to global scales (Krpec et al., 2020; Demattê et al., 2020; Poggio et al., 2021). The low cost and scalability of these information sources compared to field data make them particularly appealing in montane environments (Streher et al., 2017), where readily available field data on vegetation and soils are often scarce relative to spatial heterogeneity. This dissertation draws upon these three information sources—satellite imagery, off-the-shelf predictions from statistical models, and field-based observations—to infer the responses of vegetation and soil properties to anthropogenic and biophysical factors in a montane landscape in central Veracruz, Mexico. Portions of this work were conducted as part of a broader interdisciplinary research program quantifying trade-offs among ecosystem services in the study area (Asbjornsen et al., 2017; Berry et al., 2020; López-Ramírez et al., 2020). While the following three chapters concern distinct phenomena and spatial scales, the analyses in each chapter address their respective questions with a unifying focus on uncertainty and/or bias.

In Chapter 2, I assess the seasonal signals of different land-cover types using a land-surface phenology model applied to fine-grained (5-m) satellite imagery in conjunction with field-based forest inventories. Phenological parameters characterizing the seasonal dynamics of vegetation can serve as ecological indicators and input for hydrologic and biogeochemical models (López-Ramírez et al., 2021). Phenological analysis of fine-grained imagery holds great potential for applications in tropical montane landscapes, as recent improvements in spatial resolution make it possible to resolve the seasonal dynamics of individual land-cover types and remove the effects of small clouds. However, the number of usable fine-grained images in a given landscape can often be low, and it is unclear whether phenological parameters can be reliably estimated in

such cases. Using a Bayesian framework, I estimate phenological parameters and their uncertainties and evaluate how parameter uncertainty affects inferences on landscape-level variation in seasonality.

In Chapter 3, I critically examine predictions of soil organic carbon (SOC) storage across the study area from statistical soil models developed at regional to global scales, and I assess the potential for improving model predictions using field-based estimates of SOC stocks. This analysis is focused on reducing landscape-specific bias in model predictions for end-users of soil data who do not wish to engage in the development of new models (e.g., researchers and practitioners outside of soil science). Model calibrations and prediction uncertainties using different soil datasets and parameterizations are contrasted and interpreted relative to anthropogenic and biophysical gradients across the landscape.

Chapter 4 focuses on quantifying and correcting biases introduced in SOC estimates by the common practice of comparing soils on the basis of fixed depth intervals. Taking 16 soil profiles in the central Veracruz cloud forest belt as an example, I compare novel and existing approaches to estimating soil volume changes associated with land-use change. In addition to estimating errors in SOC stocks incurred when soil volume change is ignored, I evaluate potential bias introduced in radiocarbon activity (a proxy for SOC turnover) and the inferential consequences for comparisons across forest successional stages. Finally, I present graphical tools for diagnosing possible changes in soil mass and volume in observational settings.

Chapter 5 provides a concise overview of the preceding three chapters and their implications for understanding ecosystem service provision.

Chapter 2

Tropical montane land surface phenology: Incorporating parameter uncertainty into ecological inferences

Abstract

The seasonal dynamics of canopy leaf area and photosynthetic capacity are intimately coupled to the magnitude and timing of terrestrial fluxes of water, carbon, and nutrients. Parametric land–surface phenology models (LSP) summarize these dynamics as estimated from remotely sensed time series in terms of interpretable metrics (e.g., start of growing season [SoS] and end of growing season [EoS]). Parameters from LSP models can help to diagnose spatiotemporal variation in ecosystem responses to global change and can serve as inputs for subsequent analyses. Applications of LSP modeling have been restricted in environments with frequent cloud cover and/or where land–surface characteristics, such as topography and land-use/cover type, vary dramatically over tens to hundreds of meters. In such settings (e.g., tropical montane landscapes), the first issue may be addressed by compositing images across years, and the second by using imagery with finer spatial resolution. I evaluated the inferential utility of LSP parameter estimates obtained with these strategies for a mountainous landscape in eastern Mexico. I estimated LSP parameters at 5–m spatial resolution, using a Bayesian hierarchical model to quantify parameter uncertainty. I also demonstrated how the Bayesian framework facilitates propagation

of parameter uncertainty through downstream analyses in which LSP parameters play different roles, including analyses involving direct inference on parameters and their combinations (growing season length, estimated as EoS - SoS), the use of LSP parameters as response variables (change in SoS with elevation), and the use of LSP parameters as predictors of field data (spring greenup rate as a predictor of tree species biodiversity and deciduousness). LSP parameter estimates were best constrained for the closed–canopy broadleaf cover type, which included tropical montane cloud forests and related secondary forests. Systematic landscape-level patterns in LSP parameters were detected for closed–canopy broadleaf pixels and persisted after accounting for parameter uncertainty. Mapping parameter uncertainty revealed areas for which the existing data were poorly represented by the model and the strategy of image compositing may be inappropriate, including for land–cover types with greater relative abundance of herbaceous species. These findings underscore that LSP modeling can support ecological inferences in tropical montane landscapes despite frequent cloud cover and that propagating parameter uncertainty through downstream analyses can reduce inferential bias more broadly.

2.1 Introduction

Temporal oscillations in plant canopy structure arise through the interplay of climate and species traits and exhibit important feedbacks with energy and water balances and biogeochemical cycles. Quantification of the intraannual dynamics of vegetation as observed with air- or spaceborne sensors is referred to as land surface phenology (LSP). The *land surface* qualifier distinguishes LSP from in situ observations of seasonality of plant growth by acknowledging that each pixel of a remotely sensed dataset may represent a mixture of multiple plant species, photosynthetic and dead foliage, woody biomass, bare soil, rocks, water, and/or built surfaces, each with distinct spectral properties and temporal dynamics (de Beurs & Henebry, 2010).

Most LSP studies involve quantifying temporal dynamics throughout space, often to obtain variables for subsequent analyses. Conceivably, any multitemporal remotely sensed dataset containing phenological information (e.g., microwave, radar, solar-induced fluorescence; Guan et al., 2014; Zeng et al., 2020; Wang et al., 2020) could serve as the basis for a LSP study, though the vast majority have focused on reflectance in visible and near-infrared bands. Typically, reflectance values for each pixel and date are used to calculate a vegetation index that

more closely correlates with vegetation attributes (e.g., leaf area index and photosynthetic capacity) than does reflectance itself. Phenological metrics (e.g., start and end of growing season, minimum and maximum greenness) are then extracted for the vegetation index time series of each pixel using various empirical techniques (de Beurs & Henebry, 2010; Zeng et al., 2020). Hence, LSP modeling serves as a dimensionality reduction procedure, by which spectral and temporal variation (e.g., three reflectance bands on tens to hundreds of dates) are summarized by a small number (typically <10) of phenological metrics.

Despite fundamental differences in scale, metrics derived from LSP models have shown reasonably good agreement with *in situ* phenologies (Hwang et al., 2014). This correspondence and the broader spatial coverage of remotely sensed datasets relative to *in situ* phenologies make LSP metrics useful surrogates for plant canopy dynamics in spatially extensive analyses. For example, analyses of LSP metrics have revealed how climatic, topographic, and biological factors interact to control the seasonality of leaf flushing and senescence (Fisher et al., 2006; Elmore et al., 2012; Hwang et al., 2014; Guan et al., 2014; Lapenis et al., 2017). Other studies have leveraged LSP metrics as spatially distributed predictors of ecosystem properties (e.g., biodiversity, Waring et al., 2006; soil water-holding capacity, Araya et al., 2016; and land-use type, Nguyen & Henebry, 2019). These analyses all involve the aggregation of information across the temporal domain prior to statistical inference across the spatial domain. Ignoring the information lost through temporal aggregation, represented in part by the pixel-level uncertainty of the LSP metrics, may contribute bias to inferred spatial relationships and increase the probability of committing type I errors.

As the acquisition frequency and accessibility of multispectral imagery with high spatial resolution improves, LSP techniques become increasingly useful for analyzing an even broader range of landscapes and phenomena. For instance, fine-grained satellite imagery (10-m resolution or finer) has made it possible to map crop fields of smallholder farmers (Stratoulias et al., 2017) and characterize different vegetation types in urban environments (Tigges et al., 2013; Miller et al., 2018).

Simultaneous improvements in spatial and temporal resolution also allow for novel integration of LSP-derived metrics with field data. Fine-grained LSP metrics can now be directly

related to field data on meter-scale variation in canopy structure (e.g., gaps from selective logging, Pinagé et al., 2016) and species composition (Tigges et al., 2013). Similarly, hillslopes and valleys, which can co-occur within a single pixel of the satellite imagery traditionally used for LSP analyses (250-500 m for the Moderate Resolution Imaging Spectroradiometer [MODIS] or 1-8 km for the Advanced Very High Resolution Radiometer [AVHRR]) can be discerned using fine-grained imagery. Improved spatial resolution thus expands the possibilities to investigate feedbacks between phenology and hydrogeomorphic processes measured *in situ* (e.g., streamflow, Hwang et al., 2014; soil erosion, Möller et al., 2017).

Applications of fine-grained LSP require systematic handling of pixel-level uncertainty, particularly when temporal resolution is sparse and if LSP-derived metrics are estimated as inputs for downstream analyses (e.g., LSP-based mapping, correlation with field data). Quantifying the uncertainty of LSP parameters and derived metrics is especially important in tropical montane landscapes, where frequent cloud cover reduces the usability of already temporally sparse imagery. Furthermore, high spatial variability of LSP in such environments due to inherent biophysical complexity and short-range variation in land use underscores the need for a fine-grained approach to understanding canopy dynamics.

Bayesian modeling approaches hold great potential for LSP given their capacity to quantify parameter uncertainty and constrain parameter estimation to plausible ranges (Senf et al., 2017). While Bayesian models also facilitate propagation of parameter uncertainty to subsequent analyses, LSP research has yet to capitalize on this capability (Lunn et al., 2013; Taylor-Rodriguez et al., 2019). Furthermore, the substantial computational resources required to fit Bayesian models complicate scalability with increasing scene size and image resolution, impeding the adoption of Bayesian techniques for spatially continuous, fine-grained LSP applications (Senf et al., 2017). In this study, I build on previous efforts at Bayesian LSP modeling by developing a model of the full annual trajectory of greenness that is scalable for landscape–level coverage at high spatial resolution. Using 5-m resolution satellite imagery of a 196-km^2 area in Veracruz, Mexico, I present three use cases to illustrate the utility of a Bayesian modeling approach for propagating uncertainty. First, I estimate growing season length as a combination of model parameters and map its uncertainty across the landscape. Then, I demonstrate how the uncertainty

of LSP metrics can be accounted for in secondary statistical models using two ecological applications, one estimating the effects of topoclimate on the start of the growing season (LSP metric as response variable) and the other predicting tree biodiversity and deciduousness (LSP metrics as predictors). In each use case, I assess whether ecological inferences are robust to the uncertainty of estimated LSP parameters.

2.2 Materials and methods

2.2.1 Study area

The study area centers on the Pixquiac and Gavilanes catchments, which drain from the eastern slopes of the Cofre de Perote (4282 m), an inactive *shield-like* volcano at the eastern limit of the Trans-Mexican Volcanic Belt, into the larger Antigua basin en route to the Gulf of Mexico (Fig. 2.1). The Pixquiac and Gavilanes catchments exhibit pronounced topographic relief, with mean slope gradients greater than 30°) between 1800 and 3000 m and above 3200 m. Mean annual temperature declines from 19.3°C at 1188 m to 9.5°C at 3102 m (Servicio Meterológico Nacional, 2017). Mean annual precipitation at the same elevations is 1755 and 1708 mm, respectively (Servicio Meterológico Nacional, 2017). Annual precipitation at intermediate elevations may be twice as high in some years (Muñoz-Villers et al., 2012). Rainfall is highly seasonal, with up to 80% of the annual total falling between June and September (Fig. 2.1; Muñoz-Villers et al., 2012). Fog immersion contributes to the water balance at higher elevations through interception (Holwerda et al., 2010; Ponette-González et al., 2010) and suppression of transpiration (Alvarado-Barrientos et al., 2014). Deep, highly permeable volcanic soils mantle most of the study area (Geissert et al., 1994) and store rainwater that plants use throughout the dry season (Muñoz-Villers et al., 2020; Goldsmith et al., 2012).

Tropical montane cloud forest fragments featuring broadleaved tree species extend from 1000 to 2300 m. Cloud forest fragments are differentiated into lower montane and upper montane types on the basis of the relative abundance of tropical versus temperate tree species, with a sharp decline in tropical species abundance at approximately 1800 m (Williams-Linera et al., 2013). From 2300 to 3000 m, upper montane cloud forest grades into an assemblage of oaks (>10 *Quercus* species) and pines (*Pinus patula*, *P. ayacahuite*, *P. pseudostrobus*). Vegetation above

3000 m consists of a mosaic of coniferous forest (*P. ayacahuite*, *P. pseudostrobus*, *P. montezumae*, *P. hartwegii*, *Abies religiosa*; Vázquez Ramírez, 2014) and native grasses. Sugarcane and coffee plantations have largely replaced forest below 1200 m, and coffee co-occurs with cloud forest fragments up to 1500 m. Pasture and maize-dominated cropping systems are interspersed with forest fragments from 1300 to 3200 m. Patches undergoing secondary forest succession after logging or cessation of agricultural activities occur along the entire elevation gradient and often feature an increased abundance of shade-intolerant species (e.g., *Liquidambar styraciflua* L. below 1800 m, *Alnus acuminata* from 1800 to 3000 m, and *Alnus jorullensis* above 3000 m). Most active reforestation efforts have prioritized pine species, even within the cloud forest belt.

2.2.2 Remote sensing data

2.2.2.1 Preprocessing

I used a fully open-source pipeline to preprocess imagery and develop time series of the enhanced vegetation index (EVI), to which I later fit the Bayesian LSP model. I obtained five-band, 5–m resolution imagery from the RapidEye satellite constellation (Level 3A, orthorectified and radiometrically corrected) for all available dates with <40% cloud cover from March 2009 to May 2019 (n = 33; Planet Team, 2017). I manually masked clouds, haze, smoke, and adjacent contaminated pixels in QGIS 3.4.4 (QGIS Development Team, 2018) to restrict my analysis to pixels with the clearest possible view of the land surface (Fig. 2.2). Each scene was atmospherically corrected to surface reflectance using the 6S algorithm (Vermote et al., 1997) within the ARCSI Python package (Clewley et al., 2014). Variation in scene alignment across observation dates was mitigated via local coregistration with AROSICS software, also written in Python (Scheffler et al., 2017). The three individual tiles within each scene were histogram matched using the RStoolbox package (Leutner et al., 2019) in R version 3.5.2 (R Core Team, 2018) and mosaicked using the Geospatial Data Abstraction Library (GDAL/OGR contributors, 2020). I adjusted each scene for the effects of topography and solar geometry on illumination with the "C" correction method (Teillet et al., 1982) using the topCor function in the RStoolbox package and the Shuttle Radar Topography Mission digital elevation model, which was bilinearly interpolated to the resolution of the RapidEye imagery (NASA JPL, 2017). With each resulting

five-band raster of surface reflectance, I calculated EVI as a proxy for photosynthetic biomass:

$$EVI = \frac{G(NIR - Red)}{NIR + C_1 Red - C_2 Blue + L}, \tag{2.1}$$

where NIR, Red, and $Blue$ are reflectance in the near–infrared, red, and blue bands (760–850, 630–685, 440–510 nm, respectively) and G = 2.5, C_1 = 6, C_2 = 7.5, and L = 1 following Huete et al. (1997). In comparison to the more widely used normalized difference vegetation index, EVI saturates at higher leaf area indices, making it more suitable for the forests in the study area (Huete et al., 2002). I cropped the EVI rasters for all 33 dates to a 196-km^2 area encompassing the two study catchments and a convex hull containing the forest inventory sites analyzed in use case 3 (Fig. 2.1).

2.2.2.2 Land-use/cover mapping

Land-use/cover mapping was not an objective of the present study but was a necessary step in assessing how the uncertainty in growing season length varies across canopy types (use case 1) and to restrict the analysis of start of season to broadleaf forest types (use case 2). I trained a random forest classifier (Liaw & Wiener, 2002) on a pair of images from January and May 2017 to differentiate the following cover types: needleleaf (i.e., fully coniferous forest), closed-canopy broadleaf (cloud forest and oak-pine forest), open-canopy broadleaf (including coffee, secondary cloud forest, and secondary oak-pine forest), grass, row crop, and rock/infrastructure. I included oak-pine forest within the open- and closed-canopy broadleaf cover types because the spectral properties and phenological dynamics of oak-pine areas were more similar to cloud forest than to fully coniferous forest. Out-of-bag accuracy of the resulting land-use/cover map was 94%. To restrict my analyses to vegetated surfaces, I developed a complementary mask of rocks and infrastructure through an object-based analysis of a WorldView-2 image acquired in January 2017 (Maxar Technologies Inc.). The eight-band image was segmented in GRASS GIS 7.6 (GRASS Development Team, 2018), and the resulting objects were classified as vegetated or non–vegetated, again using a random forest algorithm (Liaw & Wiener, 2002). RapidEye pixels that intersected non–vegetated objects were excluded from LSP analyses.

2.2.3 Phenology model description

I modeled EVI dynamics for each vegetated pixel using a hierarchical Bayesian framework described in detail in Babcock et al. (2021), which builds on the methods of Melaas et al. (2013)

and Senf et al. (2017). Spring and autumn phenology are modeled using two logistic functions (Fig. 2.3; Elmore et al., 2012; Zhang et al., 2003). The spring function is

$$S_{\mathrm{t}} = \alpha_1 + \frac{\alpha_2 - \alpha_5 t}{1 + e^{-\alpha_3 (t - \alpha_4)}}, \tag{2.2}$$

where α_1 is seasonal minimum EVI, α_2 is the seasonal amplitude, α_3 is the maximum greenup rate, α_4 is the greenup inflection point, and α_5 controls the mid-growing season EVI trajectory. Time (t) is measured in days and ranges from 1 to 365. The autumn function is

$$A_{\mathrm{t}} = \alpha_1 + \frac{\alpha_2 - \alpha_5 t}{1 + e^{-\alpha_6 (\alpha_7 - t)}}, \tag{2.3}$$

where α_6 is the maximum senescence rate and α_7 is the autumn inflection point. A step function combines (2.2) and (2.3):

$$G_{\mathrm{t}} = \begin{cases} S(t) & 1 \leq t \leq \delta \\ A(t) & \delta < t \leq 365 \end{cases} \tag{2.4}$$

where δ is the time (t) at which $S(t) = A(t)$, i.e., $\delta = (\alpha_3 \alpha_4 + \alpha_6 \alpha_7)/(\alpha_3 + \alpha_6)$. The parameters of (2.4) are estimated via Bayesian inference as follows. The probability model is defined as

$$y(t) \sim \mathcal{B}(G(t), \sigma^2), \tag{2.5}$$

where $y(t)$ is EVI at time t and σ^2 is the error variance for a given pixel. $\mathcal{B}(\cdot, \cdot)$ is a beta distribution with its shape defined in terms of the mean ($G(t)$) and variance (σ^2). Note that $\mathcal{B}(\cdot, \cdot)$ can be parameterized multiple ways (e.g., $\mathcal{B}(\cdot, \cdot)$ may be defined in terms of two shape parameters; Cribari-Neto & Zeileis, 2010). The beta distribution is bounded between zero and one, making it an especially useful distribution for modeling response variables that can only take on values within that bound (e.g., EVI over vegetated surfaces). Using a beta distribution ensures that any predictions of EVI using the fitted model will be between zero and one.

Bayesian estimation of the seven α parameters and the error variance σ^2 requires prescribing prior distributions for each parameter. In this analysis, I specified vague informative prior distributions to restrict parameter estimates to plausible ranges while allowing the data (rather than the priors) to play a dominant role in parameter estimation. I selected the following prior distributions for each of the unknown parameters:

$$\alpha_1 \sim \text{Unif}(0, 1) \tag{2.6}$$

$$\alpha_2 \sim \text{Unif}(0, 1 - \alpha_1) \tag{2.7}$$

$$\alpha_3 \sim \text{Unif}(0, 1) \tag{2.8}$$

$$\alpha_4 \sim \text{Unif}(1, \alpha_7) \tag{2.9}$$

$$\alpha_5 \sim \text{Unif}(0, 0.001) \tag{2.10}$$

$$\alpha_6 \sim \text{Unif}(0, 1) \tag{2.11}$$

$$\alpha_7 \sim \text{Unif}(1, 365) \tag{2.12}$$

$$\sigma^2 \sim IG(0.001, 0.001) \tag{2.13}$$

where Unif(*a*,*b*) indicates a uniform distribution between values *a* and *b* and IG(*c*, *d*) is an with shape and scale hyperparameters *c* and *d*, respectively. The selected bounds for each of the uniform distributions ensured that modeled EVI was between zero and one (e.g., $\alpha_1 + \alpha_2 \leq 1$) and that spring greenup preceded autumn senescence (i.e., $\alpha_4 < \alpha_7$). The inverse-Gamma distribution has support for all real numbers and is commonly employed as a vague informative prior distribution of variance parameters (Finley et al., 2015).

2.2.4 Model implementation

I implemented the model using the `rsBayes` package for the `R` statistical computing environment (Finley & Babcock, 2020; R Core Team, 2018). This package includes a function for estimating the parameters of (2.4) and their uncertainty via Markov chain Monte Carlo (MCMC) sampling (Gelman et al., 1995). `rsBayes` also provides a flexible platform for propagating parameter uncertainty to downstream statistical analyses. I estimated the parameters of the model described in Section 2.2.3 individually for each of the 9 960 456 pixels in the study area. Due to limited image availability in each individual year, EVI values were pooled across years to obtain an annual composite, with 23 to 33 valid observations per pixel depending on cloud frequency. For each pixel-level model, a single MCMC chain was run for 20 000 iterations. The first 10 000 iterations were discarded as burn-in. The remaining 10 000 iterations were thinned to 1000 by selecting every tenth iteration and discarding the rest. Thinning was performed to reduce data storage needs to a reasonable level (Link & Eaton, 2012).

2.2.5 Use cases

2.2.5.1 Mapping growing season length and its uncertainty

Because ecologically meaningful LSP metrics are often obtained as functions of model parameters, the ease with which the uncertainty of these parameter combinations is determined in a Bayesian framework is a major advantage over more widely used approaches (namely, nonlinear least squares algorithms). Growing season length (GSL) provides a straightforward example of particular ecological importance, as GSL is a proxy for the annual duration of carbon uptake (Churkina et al., 2005). GSL is simply calculated as the difference (in days) between the start and end of the growing season (SoS and EoS, respectively; Reed et al., 1994). Researchers have adopted different strategies for defining and estimating SoS and EoS (reviewed by de Beurs & Henebry (2010) and Zeng et al. (2020)). For this analysis, I define SoS as the day of maximum greenup rate and EoS as the day of maximum senescence due to the sparsity of the EVI data and to maintain the simplicity of the example. However, the uncertainty propagation procedure can be applied to more complex formulations of seasonal transitions provided they are derived from model parameters (e.g., change in curvature following Zhang et al., 2003). As defined here, SoS and EoS are represented in the double-logistic model as α_4 and α_7, so GSL = α_7 - α_4. I generated samples from the posterior distribution of GSL at each pixel via composition sampling, subtracting paired α_7 and α_4 samples (Fig. 2.4). I then mapped the central tendency and uncertainty of GSL across the landscape by summarizing each pixel's GSL distribution in terms of the median and standard deviation.

2.2.5.2 Estimating topoclimatic effects on the start of season

To quantify environmental and land-use effects on canopy seasonality, LSP metrics are empirically modeled as functions of spatially (and sometimes temporally) varying covariates (e.g., Elmore et al., 2012; Lapenis et al., 2017). The pixel-level uncertainty of LSP metrics has generally been disregarded in such analyses, jeopardizing the statistical basis for inference. I demonstrate how the Bayesian LSP model facilitates accounting for this uncertainty with an example analysis of how the start of the growing season (SoS) varies along topoclimatic gradients. Estimating the rate of change in SoS with elevation (a component of Hopkins' Bioclimatic Law; Hopkins, 1918) is particularly important for monitoring and predicting climate change impacts on species distributions and ecosystem functioning (Liang, 2016; Vitasse et al., 2018).

I fit three models with increasingly complex relationships between SoS and topoclimate in an additive quantile regression framework (Fasiolo et al., 2017). I used this approach rather than a simpler analysis (e.g., multiple linear regression) for two reasons. Quantile regression allowed me to focus my analysis on the earliest possible SoS for a given combination of topoclimatic conditions by modeling the fifth percentile (rather than the mean) of the conditional distribution. Modeling early SoS rather than average SoS helped exclude delays in SoS caused by variables not included in the model (Cade & Noon, 2003). The generalized additive model (GAM) dimension of the framework provided estimates of nonlinear relationships while penalizing model complexity and constraining functional forms. For instance, modeling the effect of aspect with a cyclic cubic spline ensured continuity at $0/2\pi$ radians. I restricted my modeling to the effects of elevation and aspect after preliminary models failed to demonstrate systematic relationships between SoS and a broader range of terrain attributes (slope gradient, local relief, flow accumulation, plan and profile curvature). The simplest model included an intercept term and a linear relationship between the fifth percentile of SoS and elevation. The intermediate complexity model added a cyclic cubic term for aspect. The most complex model replaced the linear elevation term with a penalized B-spline, a nonlinear smoother composed of multiple polynomial functions (Eilers & Marx, 1996). SoS lapse rates with elevation were assessed in terms of slope coefficients from the first two models and the first derivative of the spline from the third model. Aspect effects were evaluated by examining fitted values, holding elevation constant. All models were fit to a subset of 19 736 pixels extracted by randomly sampling 0.5% of pixels classified as closed-canopy broadleaf within 10-m elevation bands from 1200 to 2800 m. Elevation and terrain attributes were obtained from the Continuo de Elevaciones Mexicano digital elevation model (version 3.0, INEGI, 2013b).

Using the `qgam` package (Fasiolo et al., 2017) in `R`, I first fit each model in conventional mode (assuming zero uncertainty in SoS) and used the median α_4 at each pixel as the response variable. Then, to assess the sensitivity of model parameter estimates to the pixel-level uncertainty in SoS, I iteratively fit the three topoclimate models for each α_4 in the 150 MCMC samples. Uncertainty of topoclimate model coefficients was propagated by randomly sampling from a normal distribution (with standard deviation = standard error of the parameter estimate) ten times for each of the 150 fittings. I report estimated coefficients and standard errors for

models ignoring the uncertainty of SoS and median coefficients and 95% credible intervals (CI) for the uncertainty propagation procedures.

2.2.5.3 Predicting tree biodiversity and deciduousness

Pixel-level parameter uncertainty has been overlooked in many of the studies that have used LSP metrics to predict independent ecological variables (e.g., Araya et al., 2016). I evaluated how the uncertainty of LSP metrics may affect their usefulness as predictors of tree biodiversity and deciduousness using species composition data from two sets of forest inventory plots in the study area. One set of plots spanned the elevation gradient (Williams-Linera et al., 2013), whereas the second set represented a range of successional stages (Vizcaíno-Bravo et al., 2020; Berry et al., 2020). The studies that established these plots employed different sampling designs, with one consisting of ten square (10 x 10 m) subplots per site and the other with four circular (11.28-m radius) subplots per site. I used data from a subset of sites (13 and 9 sites per study, respectively) for this analysis. Note that only one subplot was measured in each of the 9 successional gradient sites analyzed in this study. In both sets of plots, all individuals greater than five cm diameter at breast height were identified to family at a minimum and to genus or species when possible.

I estimated the tree biodiversity for each site with the Shannon-Wiener index,

$$H' = -\sum_{i=1}^{R} p_i \, ln \, p_i, \tag{2.14}$$

where p_i is the proportion of individuals of the ith species and R is the number of species in the site. H' ranges from zero for the case of a monospecific stand to $ln(R)$ for the case of a community with all species equally abundant. Leaf habit of each species was classified as evergreen, deciduous, or semi-deciduous based on personal observation (G. Williams-Linera, C. Gallardo, and J. Tolomé of the Instituto de Ecología, A.C., Xalapa, Veracruz). The leaf habit of individuals that were only identified to family or genus was unclassified. I quantified the *deciduousness* of each site, p_{decid}, as the abundance-weighted proportion of deciduous or semi-deciduous species within each site. A logit transformation (i.e., $logit(p_{decid}) = log(\frac{p_{decid}}{1-p_{decid}})$) was applied to p_{decid} prior to modeling to constrain back-transformed predictions to the interval [0,1].

I modeled H' and $logit(p_{decid})$ as follows. After conducting F-tests on preliminary models including multiple LSP parameters and site elevation as covariates, I selected the maximum

spring greenup rate, α_3, as a parsimonious predictor of H' and $logit(p_{decid})$ across the study area (Fig. 2.5). I then fit the simple linear models

$$ln(H') = \beta_0 + \beta_1\alpha_3 + \epsilon_1 \tag{2.15}$$

$$logit(p_{decid}) = \beta_2 + \beta_3 ln(\alpha_3) + \epsilon_2 \tag{2.16}$$

to predict H' and $logit(p_{decid})$ without considering the uncertainty in α_3. The median of the 150 thinned MCMC samples of α_3 for each pixel was used for these "exact x" models (i.e., ignoring the uncertainty in the predictor variable). This approach is analogous to the common practice of using LSP metrics obtained through frequentist parameter estimation as exact predictors in subsequent models (Nguyen & Henebry, 2019). Finally, I assessed how the uncertainty in α_3 affected its usefulness as a predictor by iteratively taking one MCMC sample of α_3 as the x value for each pixel and then fitting the same simple linear models. I compared the posterior distributions of the slope coefficients (β_1 and β_3) from the "exact x" and "uncertain x" models to evaluate changes in central tendency and spread due to the uncertainty in α_3.

2.3 Use case results

2.3.1 Mapping growing season length and its uncertainty

Growing season length (GSL), defined here using the day of maximum greenup and the day of maximum senescence as the start and end of season (SoS and EoS), respectively, exhibited substantial spatial variation and pixel-level uncertainty. Pixel-level median GSL ranged from 0.4 to 360 days across all vegetated pixels, with an overall median of 165 days. The map of pixel-level median GSL suggests that land-cover type is a first-order control on the duration of net primary production in this landscape, with greater estimated GSL for closed-canopy broadleaf cover compared to grass, crops, needleleaf, and open-canopy broadleaf cover types (Fig. 2.6). However, pixel-level median GSL generally varied inversely with the spread of the GSL posterior distribution. In other words, shorter GSLs were more poorly constrained (Fig. 2.7). Simultaneously assessing pixel–level GSL and its uncertainty indicated areas where vegetation dynamics significantly deviated from the assumptions of intraannual unimodality (e.g., due to double-cropping) or interannual stationarity (e.g., due to land-cover change or climatic differences among years).

2.3.2 Estimating topoclimatic effects on the start of season

Clear trends in the onset of the growing season, SoS, across elevations and aspects were evident and quantifiable, despite the pixel-level uncertainty of SoS and considerable heterogeneity within the broadleaf cover type (cloud forest and oak-pine forest; Fig. 2.8). The simplest model, which assumed that the earliest day of maximum spring greenup changes linearly with elevation, yielded an estimated lapse rate of 1.0±0.1 days per 100 m when the uncertainty of SoS was ignored and a median of 0.8 days per 100 m (95% credible interval from 0.6 to 1.1 days per 100 m) when the model was iteratively fit for each of the 150 MCMC samples. The model of intermediate complexity gave similar results for elevation after accounting for the effect of aspect (Fig. 2.9; identical within rounding error if the uncertainty of SoS was ignored; median of 0.9 days per 100 m [95% CI: 0.7 to 1.2] for MCMC fits). The most complex model provided evidence that the lapse rate itself (not only SoS) depends on elevation, ranging from -5.8±2 days per 100 m at 1200 m to 5.2±0.5 days per 100 m at 2560 m (Fig. 2.10). Accounting for the uncertainty of SoS narrowed the range of median lapse rates (-4.5 days per 100 m (95% CI: -9.4 to -0.5) at 1200 m and 4.85 days per 100 m (95% CI: 0.62 to 8.2) at 2755 m) while providing additional confidence that portions of the elevation gradient feature nonzero lapse rates.

Results from the two models that included an aspect term suggested that SoS occurs earlier on north-facing slopes and later on south-facing aspects (Fig. 2.11). For example, after accounting for the pixel-level uncertainty of SoS and the nonlinear effect of elevation with the third model, SoS was estimated to occur 3.1 days earlier (95% CI: 0.8 to 5 days) at an aspect of 6.03 radians (346.1°, north-by-west exposure) and 2.2 days later (95% CI: 1.1 to 3.4 days) at an aspect of 3.46 radians (198.2°, south-southwest exposure), compared to eastern or western exposures with zero estimated aspect effect.

2.3.3 Predicting tree biodiversity and deciduousness

Across the cloud forest inventory sites (Fig. 2.1), estimated maximum greenup rate, α_3, varied negatively with the Shannon-Wiener index, H', and positively with the proportion of deciduous species within a site, p_{decid} (Fig. 2.5). Three sites with divergent land-use histories (e.g., former management as coffee plantations) were graphically identified as outliers in scatterplots of α_3 versus the response variables (Fig. 2.5). One of these sites was excluded in predicting H', and

two were excluded in predicting $logit(p_{decid})$. Because I also detected a negative relationship between site elevation and α_3 (not shown), I considered site elevation itself as a predictor of H' and p_{decid} in preliminary Bayesian models. These elevation-based models suggested systematic altitudinal change in p_{decid} (12.0% decrease in the probability of a deciduous individual per 100 m increase in elevation, 95% credible interval [CI] from 0.2 to 22.4%) but not in H' (1.6% change in H' per 100 m increase in elevation, 95% CI from -1.9 to 5%). The final parsimonious models used to predict H' and p_{decid} across the study area included α_3 only, assuming that this variable integrates species composition responses to both coarse-grained altitudinal variation and finer-grained (site-level) heterogeneity. Medians and 95% credible intervals of parameters estimated for (2.15) and (2.16) are listed in Table 2.1. Accounting for the site-level uncertainty in α_3 within the model-fitting procedure caused slope coefficient posterior distributions to widen and shift towards zero (i.e., a lower median slope coefficient in the p_{decid} model and a less negative median slope coefficient in the H' model; Fig. 2.12). Using these "uncertain x" models to predict H' and p_{decid} for pixels classified as closed-canopy broadleaf generated spatially distributed predictions that simultaneously reflect the uncertainty of α_3 at the forest inventory sites, the strength of the relationship between α_3 and the response variables, and the uncertainty of α_3 at each new location (Fig. 2.13). In general, prediction uncertainty (expressed in terms of relative standard deviation) was lower for H' than for p_{decid}. Furthermore, while the uncertainty of H' predictions was not consistently related to the magnitude of predictions across the study area, p_{decid} predictions in the range of 0.55-0.65 tended to be more uncertain than were more extreme predictions (Fig. 2.14).

2.4 Discussion

Improving the spatial resolution and handling of uncertainty in land-surface phenology (LSP) research enhances the potential to gain ecological understanding from multitemporal satellite imagery. Progress on both fronts is particularly critical to LSP studies in tropical montane landscapes, where frequent cloud cover reduces temporal resolution and short-range variation in topography and land use/cover contribute to major land-surface heterogeneity within a single pixel of the most widely used satellite products (e.g., MODIS or AVHRR). I estimated the parameters of a widely used LSP model at 5-m resolution across a 196-km^2 area in the highlands of

central Veracruz, Mexico, using a Bayesian hierarchical approach to generate parameter distributions for each pixel. Furthermore, I demonstrated how a Bayesian approach makes it possible to account for the uncertainty of LSP parameters in subsequent analyses through three use cases. My findings affirm that fine-grained LSP modeling can provide a reliable basis for ecological inference in complex landscapes, even with a small number of images (e.g., 23-33 cloud-free observations per pixel). In these temporally sparse contexts, as well as in LSP research more generally, quantifying confidence in model-based inferences requires systematic consideration of parameter uncertainty. This study illustrates that a Bayesian framework facilitates this task by producing samples of the posterior distribution of parameter estimates and derived quantities, which can be easily incorporated into downstream analyses.

The use cases exemplify three types of analyses often conducted after fitting an LSP model: simple calculation using LSP model parameters, empirical modeling with an LSP parameter as the response variable, and empirical modeling with an LSP parameter as the predictor variable. While previous studies have demonstrated the sensitivity of inferences to the methodology used to extract LSP metrics (White et al., 2009; Cong et al., 2013), the statistical consequences of parameter uncertainty have received little attention (Elmore et al., 2012). This source of uncertainty reflects the disconnect between LSP observations and model parameters and has direct implications for key applications of LSP research (e.g., response of growing season length to climate change; Zhu et al., 2012). With the three use cases, I evaluated how considering parameter uncertainty would change the nature of and/or confidence in inferences drawn from each type of downstream analysis.

2.4.1 Dependence of growing season length on land-cover type

In the first use case, I mapped growing season length (GSL) across the study area and investigated the factors driving its spatial variability. Notably, I estimated longer growing seasons for the closed-canopy broadleaf cover type (primarily cloud forest) than for the other cover types (Fig. 2.6 and 2.7). This difference may arise due to a combination of internal (i.e., organismal) and environmental factors (Reich, 1995; Borchert et al., 2005). Because the arboreal cover types (i.e., open- and closed-canopy broadleaf and needleleaf) occupy largely distinct altitudinal ranges in the study area, the direct effects of cover type (e.g., due to species composition) are superimposed onto the effects of temperature, precipitation, and soil type on GSL. The high

spatial resolution of this analysis makes it possible to disentangle the effects of land cover and elevation-dependent environmental factors, as it allows comparison of GSL between neighboring patches of different cover types at a sufficiently fine grain that differences in temperature, precipitation, and soil type can be disregarded. Fine-grained variations in GSL underscore the importance of land-cover type as a primary driver of GSL in this landscape.

However, accounting for the uncertainty of the LSP parameters from which GSL was calculated (i.e., α_4 and α_7) revealed that GSL differs among land-cover types not only in terms of the distribution of pixel-level medians, but also in pixel-level uncertainty (Fig. 2.7). In many parts of the landscape, poorly constrained estimates of the start of season (α_4) and/or end of season (α_7) contributed to pixel-level posterior distributions of GSL that were too broad to support any conclusive inference (e.g., coffee pixel in Fig. 2.4). Pixels with low median GSL estimates tended to have the greatest uncertainty; these were relatively common in all cover types other than closed-canopy broadleaf (Fig. 2.7). I attribute these high-uncertainty cases to departures from the trajectory of photosynthetic biomass (i.e., as inferred from EVI) implicit in the model structure and to noise introduced through image compositing. As parameterized here, the double-logistic model assumes that minimum EVI occurs at the beginning and end of the calendar year, with a single period of increased biomass and/or elevated photosynthetic activity in between. For some locations with coffee and pasture, I posit that minimum EVI may shift from the period of minimum temperature (December-January) to that of minimum soil moisture (April-May) due to more frequent periods of soil moisture limitation in those cover types (driven by alteration of soil hydraulic properties and microclimate and/or differences in hydraulic traits across species). This delay in minimum EVI and the absence or presence of multiple periods of enhanced greenness (probable in coniferous forest and croplands, respectively) may all contribute to short and uncertain GSL estimates. Additionally, I do not expect that LSP parameters estimated on a composite dataset of images collected over 11 years are meaningful in areas that experienced major interannual change in greenness (e.g., due to climatic variation and/or physical alteration of the land surface due to anthropogenic or natural disturbance). Mapping the uncertainty of GSL served to flag these various model-data discrepancies and helped prioritize model refinements (e.g., flexible timing of minimum EVI).

2.4.2 Nonlinear response of spring phenology to topoclimate

In the second use case, I quantified the effects of topoclimate on LSP with and without considering parameter uncertainty. I focused on the effects of elevation and aspect on the start of season (SoS) to assess how spring phenology varies along gradients of energy availability within the broadleaf cover type (cloud forest and oak-pine forest) in the tropical montane study area. The rate of change in SoS with elevation embeds complex ecophysiological and climatic signals (Liang, 2016) and is an invaluable tool for diagnosing and predicting species- and ecosystem-level responses to climate change (Vitasse et al., 2018; Xia et al., 2019). In mid-latitude landscapes, SoS tends to occur later in the year with increasing elevation due to the overarching influence of adiabatic cooling. For instance, Hopkins (1918) estimated that springtime phenological phenomena (e.g., budburst) occur 3.3 days later per 100-m increase in elevation based on observations throughout the United States. However, as acknowledged by Hopkins (1918) and confirmed by more recent field- and LSP-based studies (e.g., Fisher et al., 2006; Hudson Dunn & de Beurs, 2011; Pellerin et al., 2012; Lapenis et al., 2017; Xia et al., 2019), phenological lapse rates can range widely among landscapes (e.g., 2 to 7 days per 100 m). Lapse rates can even vary within a single landscape (Elmore et al., 2012), though researchers typically estimate a single lapse rate per landscape. Inconsistencies in the magnitude (and even direction) of the relationship between elevation and SoS may be due to overlapping gradients in environmental variables other than temperature (e.g., precipitation, soil properties), endogenous factors (e.g., genotypically controlled sensitivity to chilling, warmth accumulation, and insolation; Borchert et al., 2005; Liang, 2016), and land use. While the rarity of LSP studies along elevation gradients in tropical montane landscapes precludes quantitative generalization (Streher et al., 2017; Xia et al., 2019), lapse rates in these landscapes are likely even more variable than in mid-latitude contexts. Greater complexity of environmental forcings and plant biogeographical legacies (mediating the spatial distribution of endogenous phenology controls) (Lauer, 1973; Sarmiento, 1986; Toledo-Garibaldi & Williams-Linera, 2014) along tropical elevation gradients are further differentiated by altitudinally dependent human activity (Vizcaíno-Bravo et al., 2020). In this study, I employed a statistical approach to mitigate these challenges and generate interpretable estimates of how SoS varies with topoclimate, while recognizing that SoS is itself an estimated (not measured) variable.

Comparison of the three additive quantile regression models underscores the need to revisit

the assumption of a linear relationship between elevation and spring phenology. The two models that assumed a linear effect of elevation yielded slope coefficient estimates that were positive (i.e., delayed SoS at higher elevations) but no more than 50% of the lapse rates reported for temperate zones (0.8 to 1 day per 100 m in this study versus >2 days per 100 m in the studies cited above). Accounting for the uncertainty of SoS and/or the effect of aspect did not dramatically change this finding (Fig. 2.9). In contrast, when the effect of elevation on SoS was represented with a nonlinear term, distinct regimes of more pronounced SoS lapse rates became apparent within specific elevation bands (Fig. 2.8 and 2.10). From 1200 to approximately 1500 m, SoS occurs earlier with increasing elevation (i.e., negative lapse rate). The median lapse rate changes sign between 1530 and 1590 m, but the evidence for a positive lapse rate only becomes convincing (i.e., 95%CI does not include zero) above 2260 m. The lapse rates between 2330 and 2730 m are remarkably higher (median rate: 4.2 days per 100 m; 95%CI: 1.1 to 7.7) than the gradient-wide lapse rates estimated with the two simpler models (0.6 to 1.2 days per 100 m). Notably, estimates of the nonlinear variation of SoS with elevation were robust to the uncertainty of SoS (Fig. 10).

Though definitive explanation of the altitudinal zonation of SoS lapse rates requires further field measurements and climatic analyses, I contend that the detected trends are likely due to interactions between climate and the biogeographical origin (i.e., temperate versus tropical) of dominant tree species. The latter, in turn, reflects processes of climatic and anthropogenic filtering. The previously described altitudinal thresholds in SoS lapse rates correspond closely to key bioclimatic transition zones along the elevation gradient. Days with frost are exceedingly rare below 1500 m (Lauer, 1973). Fog frequency is also likely reduced at lower elevations, though published observations have been restricted to a small number of points along the elevation gradient (Ponette-González et al., 2010; Alvarado-Barrientos et al., 2014) and relatively short time periods (one to two years, Vogelmann, 1973). Above 2200 m, the probability of frost increases dramatically (Lauer, 1973), as does the dominance of oak and pine species, whereas cloud forest *sensu stricto* is limited to narrow ravines. Collectively, climatic factors contribute to the coexistence of species of tropical and temperate affinities at lower elevations and greater dominance of temperate-affinity species at higher elevations (Lauer, 1973; Williams-Linera et al., 2013; Toledo-Garibaldi & Williams-Linera, 2014). The diversity of bioclimatic affinities of species at lower elevations implies greater heterogeneity of environmental sensitivities and endogenous

phenological controls, which may contribute to the negative SoS lapse rates observed from 1200 to 1500 m.

Considering that the local lapse rate of mean annual temperature is not significantly less than the global average (0.51 versus 0.55 °C per 100 m, respectively; Körner, 2007), the dampening of the SoS lapse rate from 1500 to 2200 m may be explained by the subordinate role of temperature in triggering spring phenology in species of temperate affinity growing under a tropical temperature regime. Temperate species that are fully deciduous elsewhere in their range (e.g., *Liquidambar styraciflua* L., *Carpinus caroliniana*) here exhibit leaf-exchanging behavior; that is, budbreak and leaf expansion occur shortly after abscission, with no pronounced dormant period (Borchert et al., 2005). Temperature (and hence elevation) appears to mediate this process primarily through species-specific effects on the timing of abscission (Williams-Linera, 1997, 2000). Deviations in the SoS lapse rate at lower and higher elevations may be related to the temporal overlap of leaf abscission and flushing (e.g., leaf expansion before full shedding in Quercus species; Borchert et al., 2005), as well as the dependence of abscission on seasonal moisture deficits (particularly at lower elevations), day length, and phylogeny (Williams-Linera, 2000).

I also detected a systematic effect of aspect on SoS, with maximum greenup occurring approximately five days earlier on north-facing slopes compared to south-facing slopes. This result implies that the slopes receiving the least solar radiation exhibit a phenological advance equivalent to a 500-m decrease in elevation (assuming the gradient-wide lapse rate of 1 day per 100 m). Purely physical phenomena (e.g., solar geometry dynamics) may contribute to the estimated aspect effect. For instance, reflectance on slopes with different aspects varies as a function of view angle and solar geometry throughout the year. Topographic correction reduces artifacts from differential illumination (Galvão et al., 2016), but residual errors may persist after correction. Differences in species composition on slopes with contrasting aspects (e.g., greater abundance of *Fagus grandifolia* var. *mexicana* on north-facing slopes) may also explain this finding, inviting future research on the role of aspect in differentiating bioclimatic conditions and/or species assemblages in humid landscapes.

2.4.3 Spring phenology as proxy for species composition

In the third use case, I developed spatial predictions of the diversity of tree species in broadleaf forests (cloud forest and oak-pine forest). These predictions were based on simple linear relationships between the maximum greenup rate, α_3, estimated with the Bayesian phenology model and the Shannon-Wiener index, H', and abundance-weighted proportion of deciduous species, p_{decid}, calculated for two sets of forest inventory plots (Fig. 2.5). In general, more diverse stands greened up more gradually and featured lower proportions of deciduous species. Independent of leaf habit, an inverse relationship between canopy diversity and maximum greenup rate may be expected from an LSP perspective if species undergo spring phenology asynchronously (Reich, 1995). In this case, as the number of species within the area of analysis (pixel or plot) increases, LSP dynamics are increasingly smoothed due to the mixing of a larger number of staggered greenup curves. Apart from diluting the seasonal signal of deciduous species, evergreen species abundance may directly affect α_3. For example, leaf exchange has been shown to occur asynchronously within individual broadleaf-evergreen species in the study area (Williams-Linera, 2000), so that even a monospecific evergreen stand would be expected to have a lower α_3 due to the temporal mixing described for multispecies stands. Additionally, longer leaf lifetimes in evergreen species (Williams-Linera, 2000) may maintain higher minimum greenness, in which case α_3 could be reduced due to a smaller increase in greenness per unit time. Weak positive correlations between median parameter estimates of seasonal minimum greenness and maximum greenup rate (ρ_{α_1,α_3}=0.32) and the abundance of deciduous trees ($\rho_{\alpha_1,logit(p_{decid})}$=0.42) across the forest inventory sites are inconsistent with this explanation.

I argue that the mixing of asynchronous deciduous and evergreen greenup dynamics is the most likely explanation for the negative relationship between α_3 and H'. Low-diversity sites tend to be relatively enriched in deciduous species and may therefore exhibit a pronounced increase in greenness over a brief period, leading to a higher value of α_3. Climate undoubtedly plays a role in phenology and community assembly in this landscape (Williams-Linera, 2000; Toledo-Garibaldi & Williams-Linera, 2014) and likely contributes to the relationships between elevation and the forest metrics modeled in this study. However, patch- to landscape-scale patterns in α_3 and p_{decid} and H' may also reveal spatial variation in the intensity of historical disturbance. The dominance of deciduous species is particularly pronounced where shade-intolerant species (e.g., *Liquidambar styraciflua* L., *Alnus acuminata*) have colonized full-sun habitats (e.g., clear-cuts and pastures; Muñiz-Castro et al., 2012) and where shade-tolerant species (e.g.,

Quercus spp.) have been selectively logged. α_3 estimated with 5-m resolution imagery may serve as a proxy for such conditions.

Accounting for the parameter uncertainty of α_3 had a moderating effect on slope coefficient distributions (Fig. 2.12) without undermining confidence in the predictive relationships for mapping purposes (95% credible intervals excluded zero with or without accounting for uncertainty of α_3; Table 2.1). Maps of median H' and p_{decid} predicted for each pixel on the basis of α_3 were similar but not identical (Fig. 2.13). More importantly, prediction uncertainties, representing both the uncertainty of the predictive relationships and the spread of the α_3 at each new location, behaved differently for the two response variables (Fig. 2.14): the central tendency and uncertainty of p_{decid} predictions exhibited a convex relationship, whereas they were largely decoupled for H' predictions. Hence, prediction uncertainties were lowest where the predicted abundance of deciduous species was highest; these areas were further differentiated by the uncertainty of H' predictions (i.e., low H' with low uncertainty versus low H' with high uncertainty). Simultaneously considering estimated phenological parameters, their relationship to field data, and associated uncertainty represents a promising means of moving from broadly defined land-cover types to mapping the compositional heterogeneity of forest stands along topoclimatic and disturbance gradients.

2.5 Conclusion

In this study, I modeled land surface phenology (LSP) in a landscape with frequent cloud cover and complex topography and land-cover patterns and evaluated the utility of LSP parameters in downstream analyses. The high spatial resolution (5 m) of the underlying imagery made it possible to resolve the LSP dynamics of individual land surface features that would co-occur within single pixels of the coarser satellite imagery typically used for LSP studies. This improved spatial resolution allowed me to quantitatively relate LSP parameters to land-cover type, topography, and the tree biodiversity of forest patches. Using a Bayesian hierarchical model, I quantified the uncertainty of LSP parameters and assessed how this uncertainty affected overall inferences. Evaluation of uncertainty was critical to (1) gauging the sufficiency of the input imagery time series (23 to 33 valid observations per pixel), (2) identifying where and when the observed greenness dynamics are consistent with the model representation (e.g., higher confidence for closed-canopy broadleaf forest compared to other land-cover types and for greenup

rather than senescence), and (3) prioritizing model improvements (e.g., flexible timing of minimum greenness, extension to other functional forms). The use cases demonstrate that accounting for the uncertainty of LSP parameters in subsequent analyses helps reduce bias and provides a more complete representation of the possible range of relationships (e.g., the effect of elevation on the start of the growing season). I encourage the wider adoption of uncertainty propagation techniques in LSP research, particularly as spatial resolution improves and integration with diverse types of field data (e.g., sap flow) becomes more common.

2.6 Tables

ln(H') = $\beta_0 + \beta_1\alpha_3$						
	Exact α_3			**Uncertain** α_3		
Parameter	**50%**	**2.5%**	**97.5%**	**50%**	**2.5%**	**97.5%**
β_0	0.95	0.83	1.08	0.89	0.75	1.04
β_1	-0.88	-1.32	-0.49	-0.61	-1.23	-0.13
σ^2	0.026	0.015	0.053	0.032	0.013	0.073
logit(p_{decid}) = $\beta_2 + \beta_3 ln(\alpha_3)$						
	Exact α_3			**Uncertain** α_3		
Parameter	**50%**	**2.5%**	**97.5%**	**50%**	**2.5%**	**97.5%**
β_2	1.59	0.99	2.15	1.20	0.55	1.88
β_3	0.77	0.47	1.07	0.57	0.24	0.89
σ^2	0.22	0.12	0.46	0.31	0.14	0.70

Table 2.1: Summary of posterior distributions of tree biodiversity model parameters as estimated while ignoring or accounting for the parameter uncertainty of α_3.

2.7 Figures

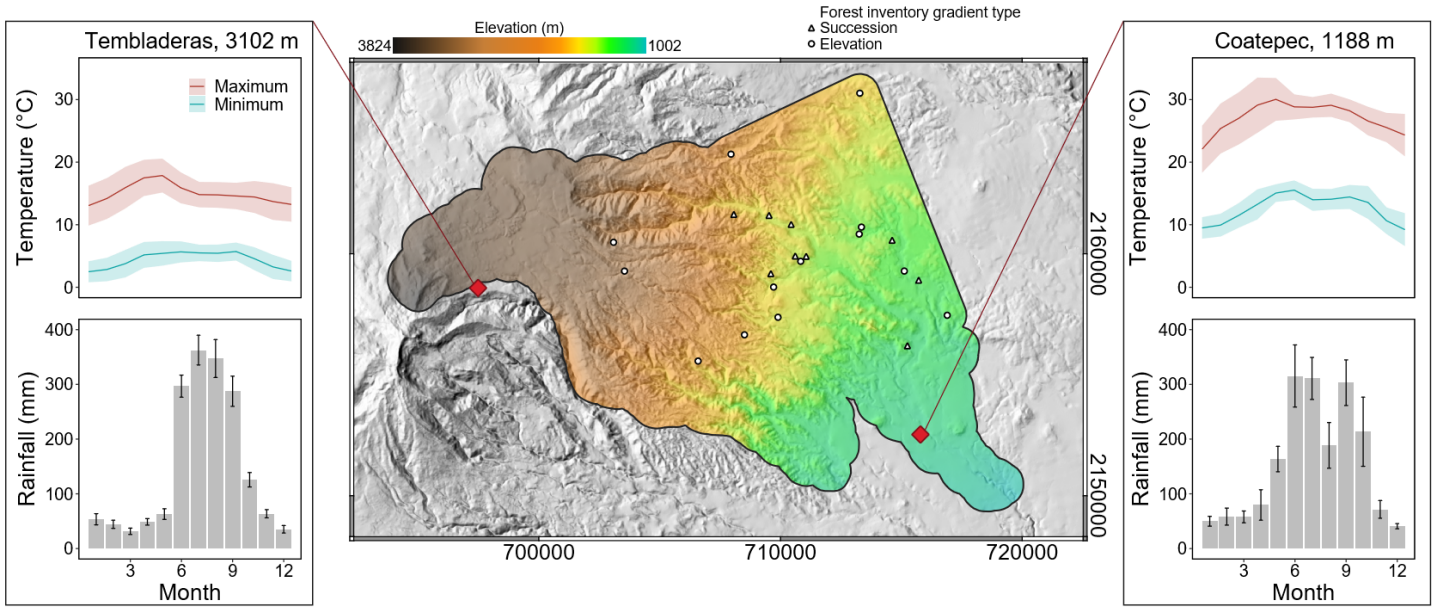

Figure 2.1: Physiography and climatology of the tropical montane study area in central Veracruz, Mexico. White points indicate locations of forest inventory plots (use case 3). Black bars on mean monthly precipitation totals indicate ±1 standard error; variability around temperature curves is presented as ±1 standard deviation to improve legibility. Digital elevation model from INEGI (2013b). Precipitation and temperature data from Servicio Meterológico Nacional (2017). Map projection: WGS 84 / UTM zone 14N.

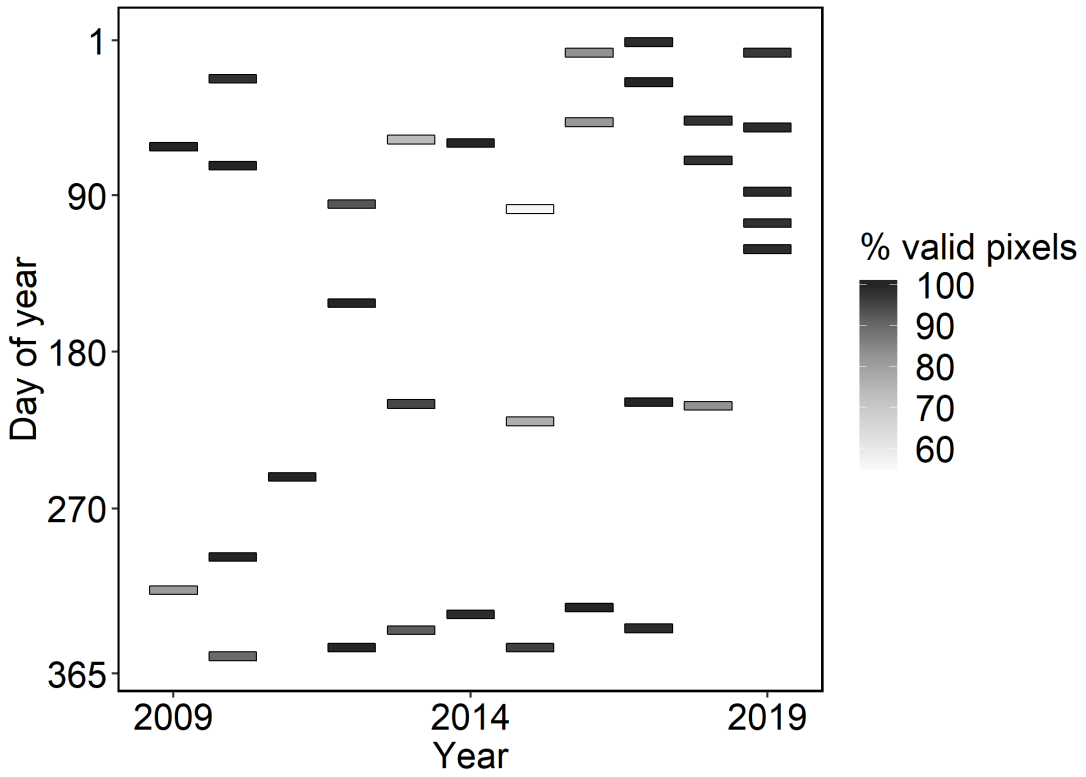

Figure 2.2: Temporal distribution and scene completeness of RapidEye images used to estimate the parameters of the phenology model.

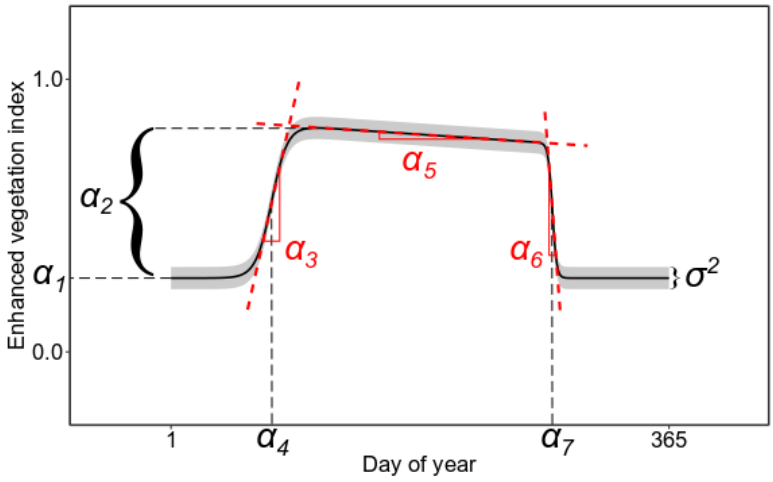

Figure 2.3: Illustration of the double-logistic phenology model. With time represented by day of year on the x-axis and greenness represented by the enhanced vegetation index (EVI) on the y-axis, the model represents the seasonal enhancement of greenness, interpreted as an increase in the photosynthetic capacity of individual leaves and/or an increase in total leaf area, plus aseasonal variance. In this study, the value of EVI on each day of year was modeled as a draw from a beta distribution with a mean determined by α_1 through α_7 and variance represented by σ^2. α_1 = minimum EVI, α_2 = difference between minimum and maximum EVI (i.e., amplitude), α_3 = maximum greenup rate, α_4 = day of maximum greenup rate (spring inflection point), α_5 = mid-growing season slope, α_6 = maximum senescence rate, α_7 = day of maximum senescence rate (autumn inflection point).

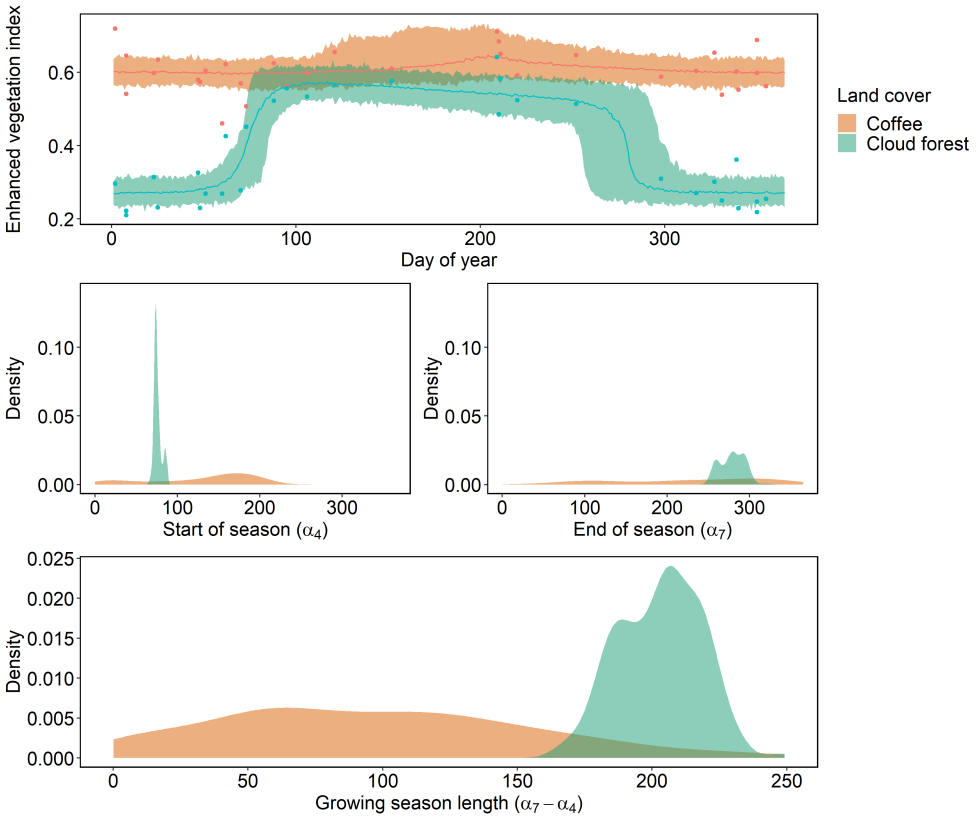

Figure 2.4: Estimation of growing season length (GSL, days) from greenness dynamics for a single pixel in a cloud forest fragment and another in a nearby coffee plantation. Top: Enhanced vegetation index (EVI) values for each RapidEye image (points) and fitted double-logistic models (solid line: median predicted values; envelopes: 95% prediction intervals). Middle left: posterior distributions of the start of season (day of year), here defined as the α_4 parameter of the double-logistic model. Middle right: posterior distributions of the end of season (day of year), here defined as the α_7 parameter of the double-logistic model. Bottom: posterior distributions of GSL generated via composition sampling (i.e., α_7 - α_4).

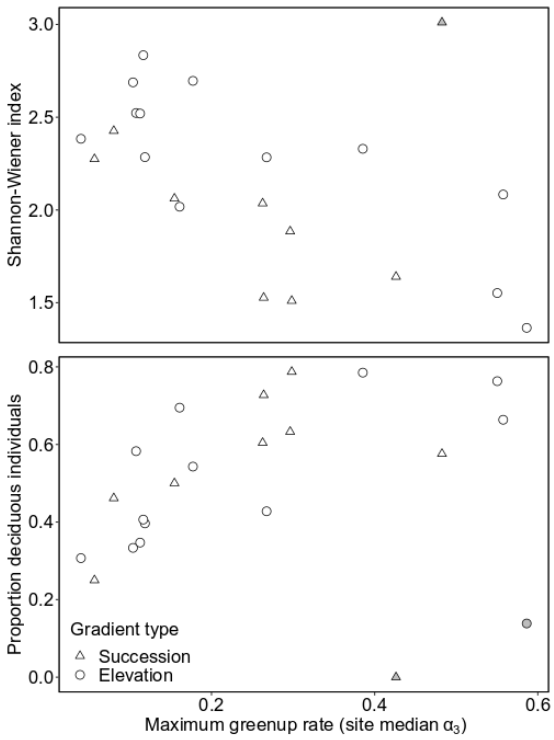

Figure 2.5: Relationships between maximum greenup rate (α_3) estimated with the Bayesian hierarchical model and tree biodiversity metrics calculated for forest inventory plots. For this illustration, medians of the pixel-level posterior distributions of α_3 were summarized as the median within a 5-m radius about each site center. These simple linear relationships form the basis of the analyses conducted in use case 3 (see equations (2.15) and (2.16) for variable transformations applied prior to model fitting). Sites excluded from model fitting are indicated in gray. Data for succession gradient sites from Vizcaíno-Bravo et al. (2020) and Berry et al. (2020). Data for elevation gradient sites from Williams-Linera et al. (2013).

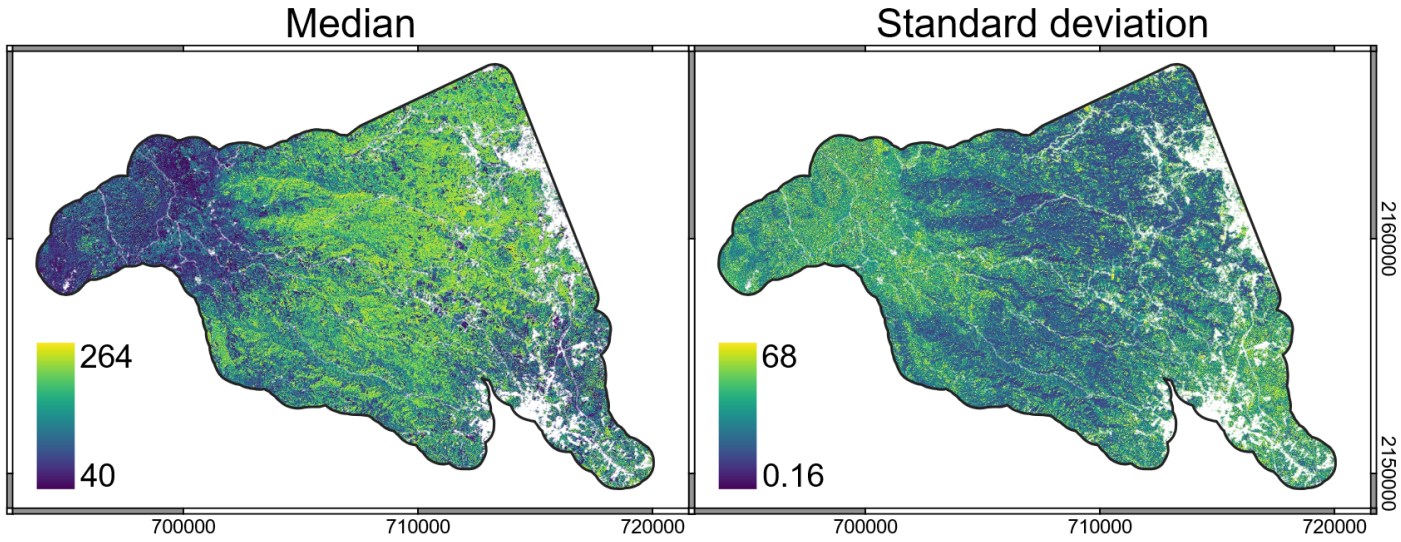

Figure 2.6: Spatial distribution of growing season length (GSL, days). Pixel-level posterior distributions of GSL are summarized in terms of median and standard deviation. Variability at each pixel is due to the uncertainty in the start of season and end of season as estimated with the Bayesian hierarchical model. The zone of higher median GSL with lower standard deviations at intermediate elevations is dominated by broadleaf forest (cloud forest and oak-alder forest). Non-vegetated surfaces (rocks, roads, and buildings) within the study area have been excluded. Palettes are adjusted to ± 2 standard deviations to enhance visual contrast.

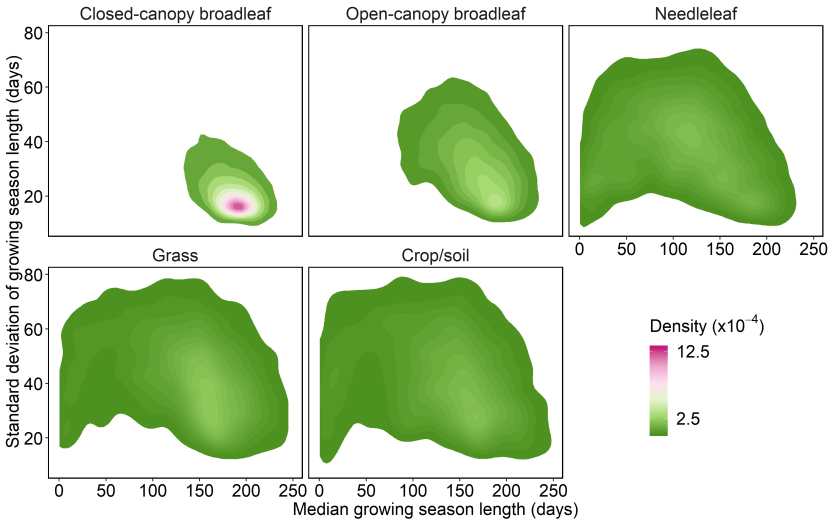

Figure 2.7: Two-dimensional kernel density distributions of the median and standard deviation of growing season length (GSL) across land-cover types. Median and standard deviation refer to pixel-level posterior distributions of GSL. Hue indicates the frequency of pixels with a particular combination of median GSL and uncertainty. GSL estimates were the least variable across the landscape (narrower range along x–axis) and best constrained at the pixel level (lower values on y–axis) for the closed–canopy broadleaf cover type compared to the other cover types. Closed–canopy broadleaf includes tropical montane cloud forest and oak-pine forest. Open–canopy broadleaf includes shade coffee as well as isolated broadleaf trees (e.g., silvopastoral systems) and broadleaf forest at early successional stages. Needleleaf includes coniferous species. Grass includes pastures and natural grasslands. Areas mapped as crops (maize, sugarcane, potato) and bare soil are grouped due to the ambiguous interpretation of growth/fallow dynamics as estimated using images pooled across multiple years. A subset of 100 000 pixels were randomly sampled for visualization.

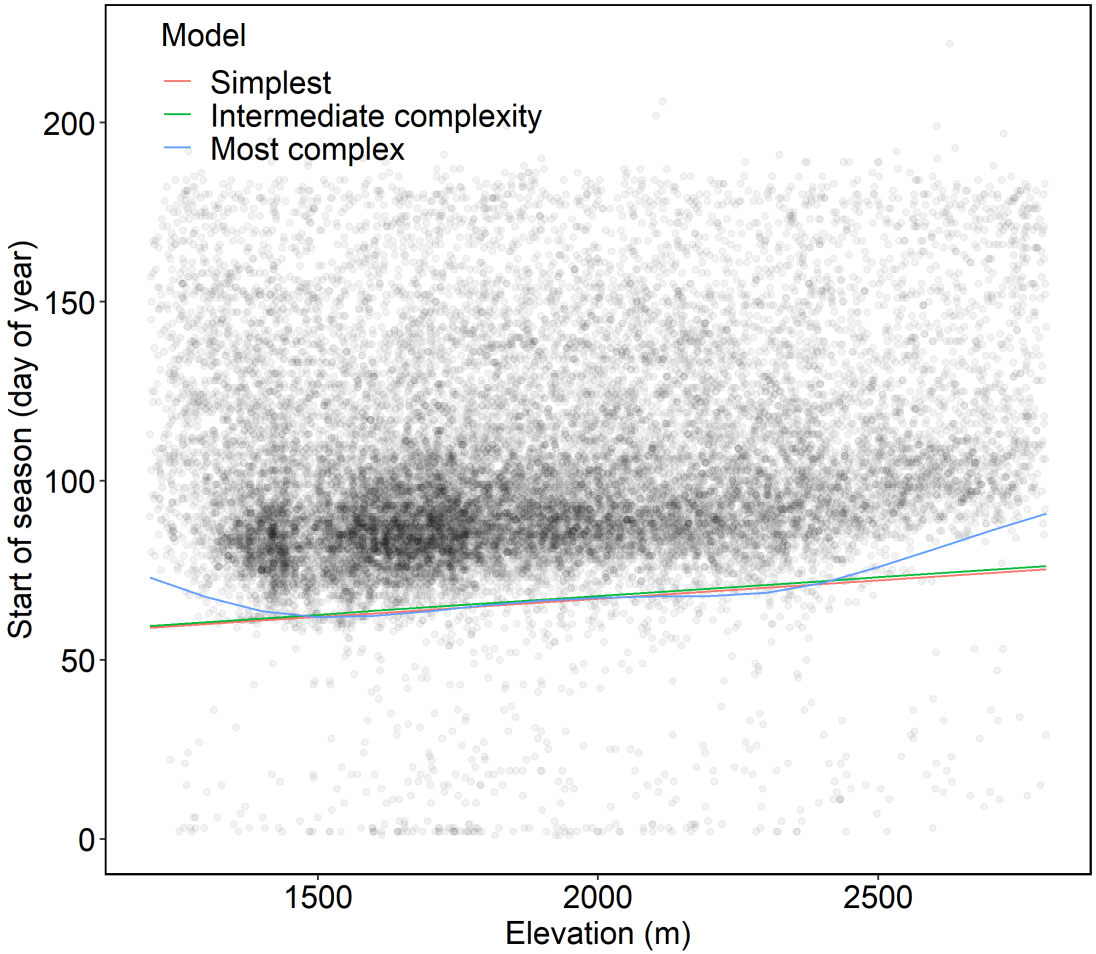

Figure 2.8: Altitudinal variation of the start of season (SoS) in the closed-canopy broadleaf cover type. The y-coordinate of each point is the median of the posterior distribution of SoS (i.e., α_4) as estimated with the Bayesian hierarchical model. Points were randomly sampled within 10-m elevation bands. Lines indicate the effect of elevation on the fifth percentile of SoS as estimated with additive quantile regression models without accounting for the pixel-level uncertainty of SoS. In the intermediate and most complex models, the effect of aspect was accounted for in model fitting. Points with SoS close to 1 are associated with isolated pixels with high parameter uncertainty.

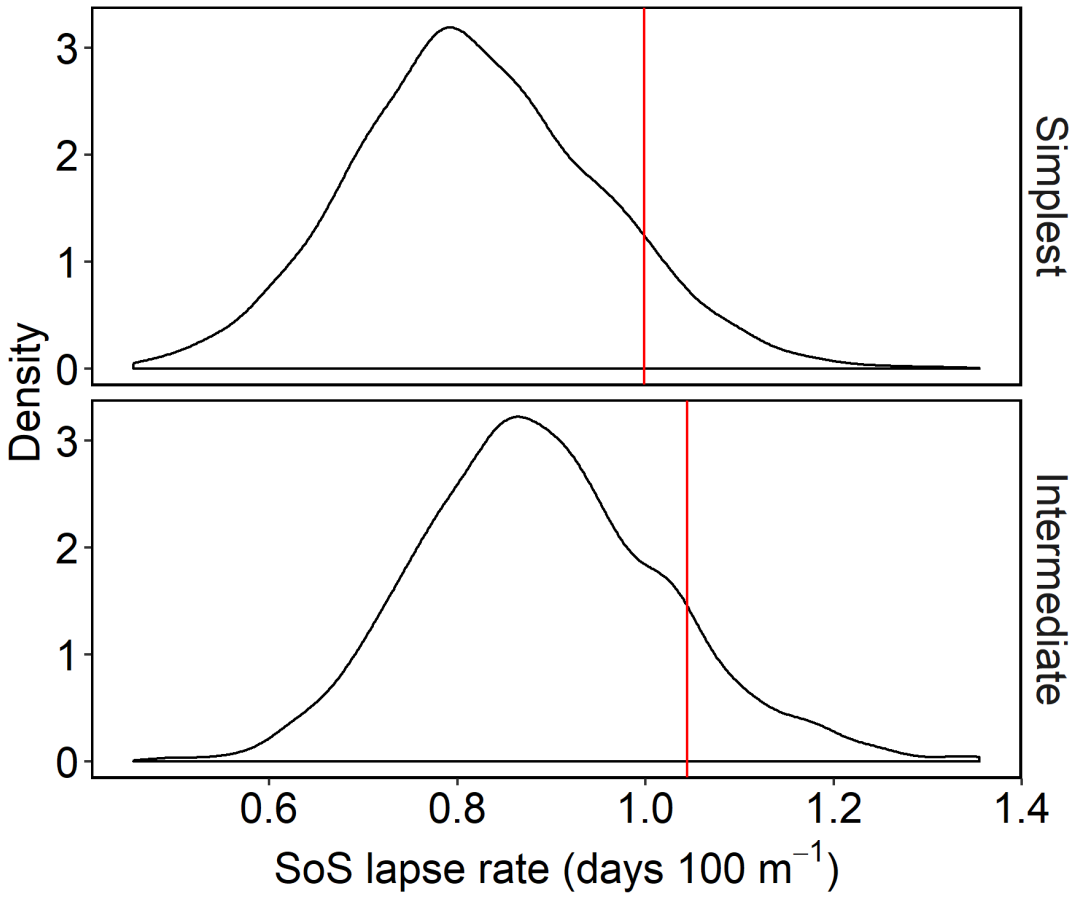

Figure 2.9: Rates of change in the fifth percentile of the start of season (SoS) with elevation in the closed-canopy broadleaf cover type as estimated with a simple linear model (top) and a model including the nonlinear effect of slope aspect (bottom). Vertical lines indicate SoS lapse rates estimated by fitting the models to pixel-level medians of SoS (i.e., α_4). Distributions are SoS lapse rates obtained by iteratively fitting the models to the thinned MCMC samples of SoS.

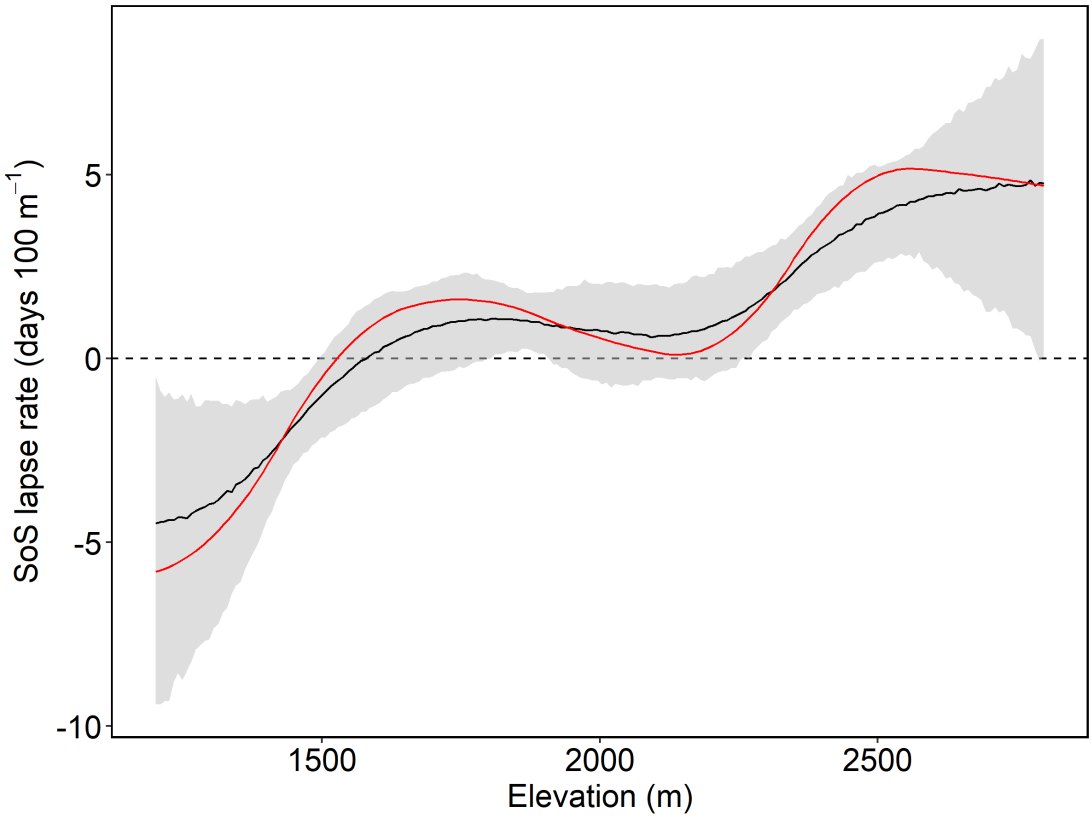

Figure 2.10: Altitudinal dependence of the start of season (SoS) lapse rate in the closed-canopy broadleaf cover type. The lapse rate function was estimated as the first derivative of a penalized B-spline predicting the fifth percentile of SoS as a function of elevation in an additive quantile regression model. The effect of slope aspect was accounted for with a cyclic cubic spline. The lighter curve (red in digital version) indicates the lapse rate function obtained from the model fit to pixel-level medians of SoS, whereas the darker (black) curve and envelop indicate the median and 95% credible intervals, respectively, of lapse rate functions obtained by iteratively fitting the model to the thinned MCMC samples of SoS.

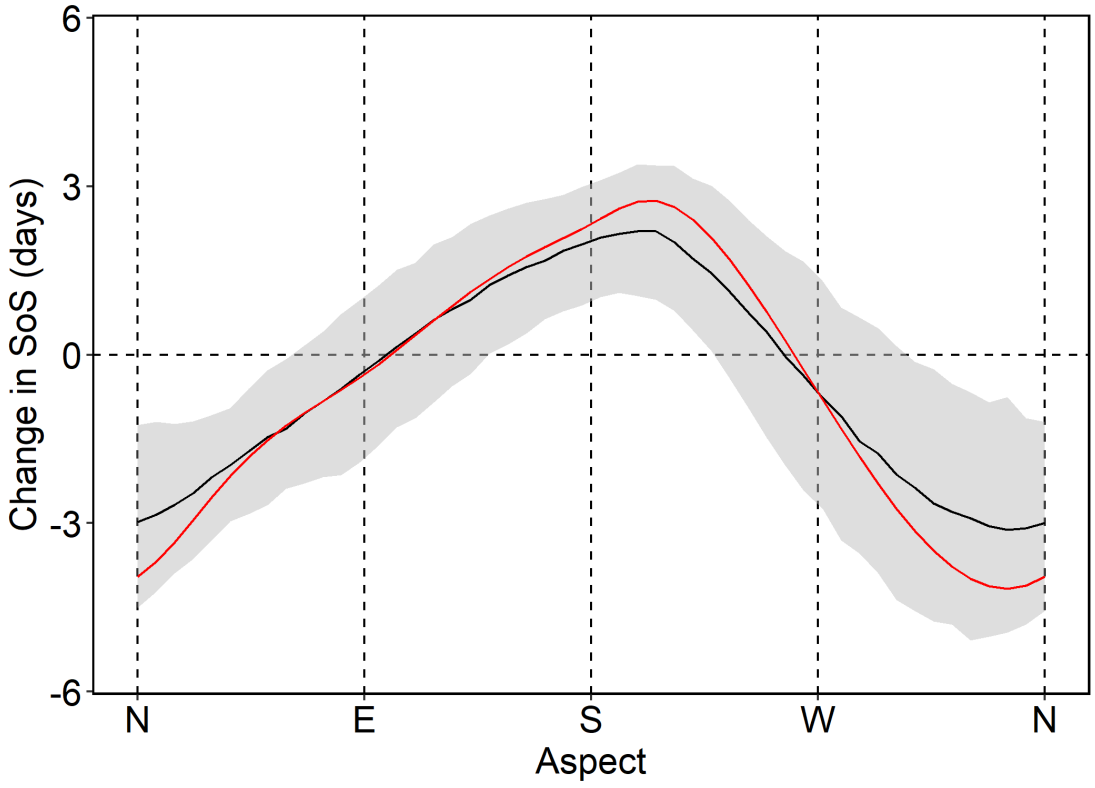

Figure 2.11: The effect of slope aspect on the start of season (SoS) in the closed-canopy broadleaf cover type. The aspect effect was estimated using a cyclic cubic spline in an additive quantile regression, after accounting for the nonlinear effect of elevation on SoS. The lighter curve (red in digital version) indicates the aspect effect obtained from the model fit to pixel-level medians of SoS, whereas the darker (black) curve and envelop indicate the median and 95% credible intervals, respectively, of the aspect effect obtained by iteratively fitting the model to the thinned MCMC samples of SoS.

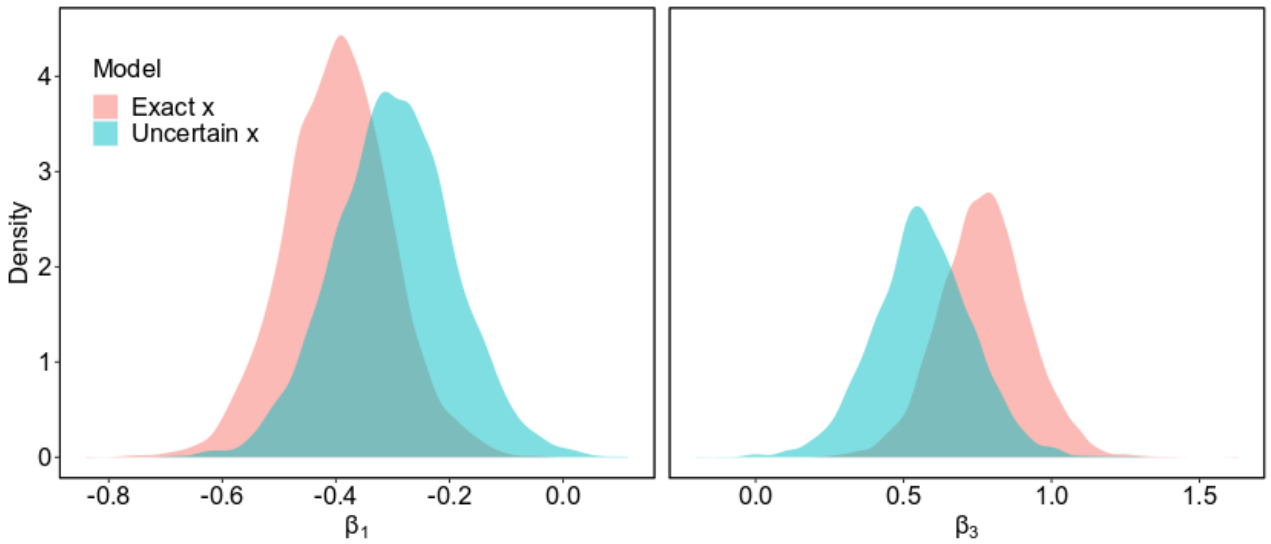

Figure 2.12: Posterior distributions of slope coefficients from simple linear models predicting tree diversity on the basis of maximum greenup rate parameter (α_3). Coefficient distributions obtained by fitting the models to site median values of α_3 (*exact x*) are displayed in red, whereas distributions obtained by fitting the model to the thinned MCMC samples of α_3 (*uncertain x*) are shown in blue. Left: coefficient distributions for the model predicting the Shannon-Wiener index (H'). Right: coefficient distributions for the model predicting the abundance-weighted proportion of deciduous species (p_{decid}).

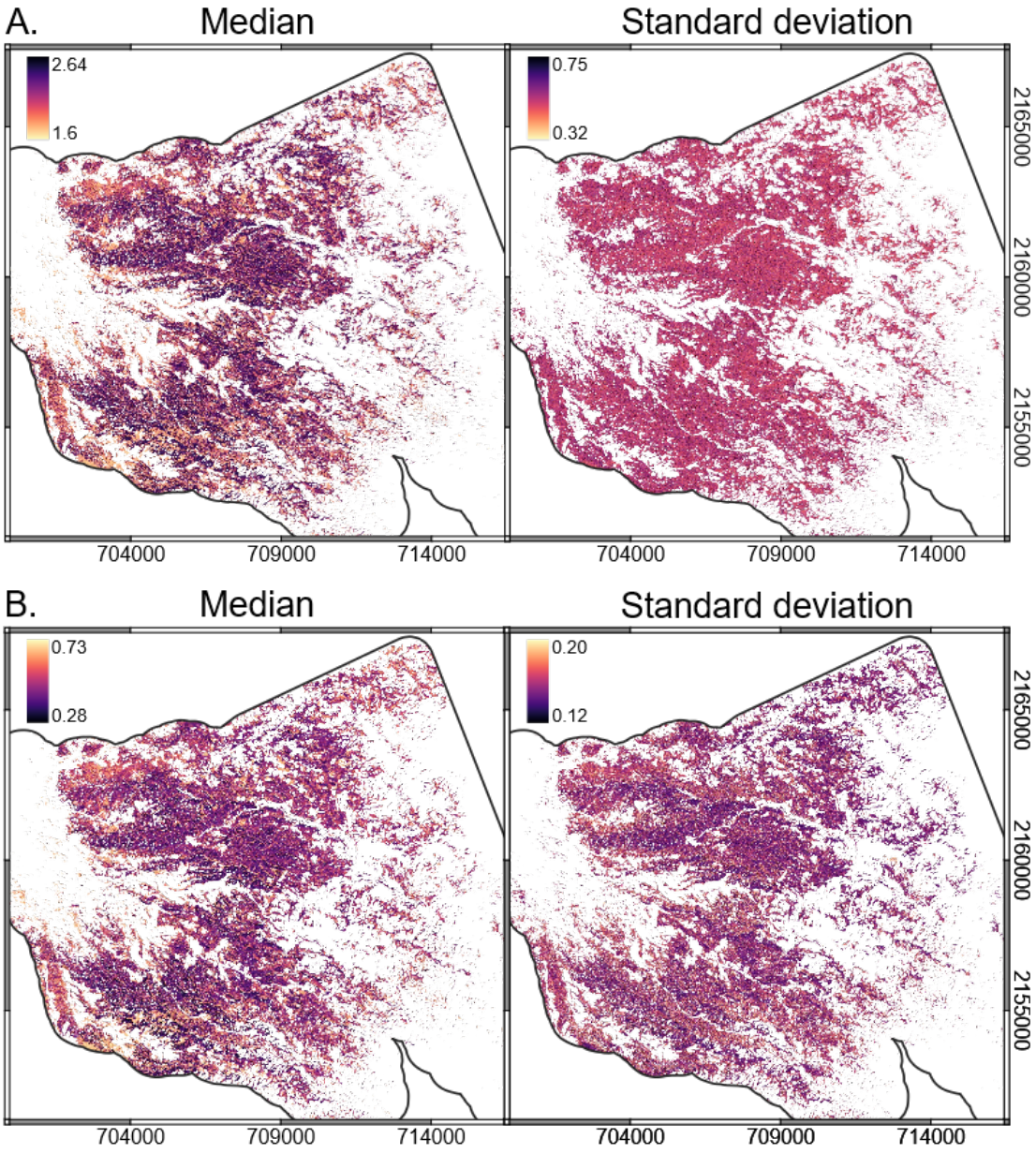

Figure 2.13: Spatial predictions of tree biodiversity metrics for closed-canopy broadleaf forest on the basis of α_3. Posterior distributions of predictions, representing the uncertainty of the underlying predictive relationship as well as the parameter uncertainty of α_3 at each pixel, are summarized in terms of pixel-level medians and standard deviations. Palettes are adjusted to ± 2 standard deviations to enhance visual contrast. A. Predicted Shannon-Wiener index (H'). B. Predicted abundance-weighted proportion of deciduous species (p_{decid}). Palette inverted to facilitate comparison with predicted H'.

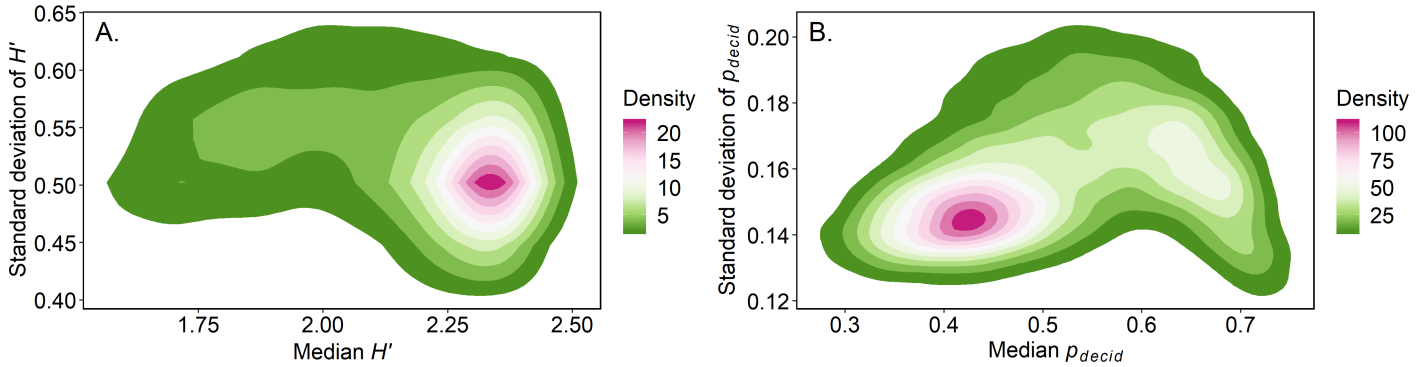

Figure 2.14: Two-dimensional kernel density distributions of tree biodiversity predictions and associated uncertainty for a subset of 10 000 closed-canopy broadleaf pixels. Hue indicates the frequency of pixels with similar medians and standard deviations. A. Pixel-level medians and standard deviations of predicted Shannon-Wiener index (H'). B. Pixel-level medians and standard deviations of predicted abundance-weighted proportion of deciduous species (p_{decid}).

Chapter 3

Bayesian calibration of regional-to-global soil products for landscape-level soil organic carbon mapping

Abstract

The role of regional-to-global soil models for understanding landscape-level variation in soil properties and soil-mediated ecosystem services (e.g., soil organic carbon [SOC] storage) is unclear. In landscapes where biophysical and anthropogenic characteristics change abruptly over short distances, the dominant patterns in soil properties may be determined by factors that cannot feasibly be represented within coarse-resolution empirical soil models (e.g., geochemistry and land-use history). In this study, I evaluated whether predictions from existing soil models can be improved for landscape-specific applications, without requiring additional covariates or significant input from end-users, by leveraging soils observations within a Bayesian hierarchical framework. Focusing on a mountainous landscape in east-central Mexico, I calculated SOC inventories for 0-30 cm and 30-100 cm depth intervals along gradients of topoclimate, geochemistry, and disturbance/succession using original and previously published data. I then used these calculated inventories to locally calibrate predictions from models developed at regional

and global levels. This approach yielded estimates of parameter and prediction uncertainties and allowed for simultaneous prediction (coregionalization) of top- and subsoil SOC inventories. Apart from correcting the overall (generally negative) bias of existing model predictions, spatially varying coefficients clarified landscape-level patterns that were underestimated by or missing from regional-to-global soil products. Persistent prediction uncertainty remaining after calibration, taken together with site-level uncertainties in SOC inventories due to the use of pedotransfer functions, underscored the continued importance of field-based observations and the need for scalable indicators of pedologic variability.

3.1 Introduction

Societal recognition of our dependence on soils and the ecosystem services they provide appears to have reached an unprecedented high (Bender et al., 2016; Griscom et al., 2017; Keesstra et al., 2018). Soils play critical roles in regulating the cycles of carbon, water, and nutrients; in filtering and/or degrading hazardous compounds; in supporting plant growth; in providing habitat and substrate for fauna and fungi and physical support for anthropogenic infrastructure; and in contributing materially and symbolically to the spiritual and aesthetic dimensions of human civilization (Dominati et al., 2010; Adhikari & Hartemink, 2016).

Soils are inherently heterogeneous in space and time, as are the environmental and human factors that mediate ecosystem service provision by soils (Hanesch & Scholger, 2002; Grunwald, 2005; García Calderón et al., 2006; Rossiter & Bouma, 2018; Marín-Castro et al., 2016; Yang et al., 2018). Understanding how soils vary spatially is particularly important for conserving hotspots of ecosystem service provision (Turner et al., 2012; Mokondoko et al., 2018) and for identifying optimal areas for the restoration of ecosystem services (Berry et al., 2005; Crossman & Bryan, 2009; Rosenstock et al., 2014).

Because soil properties reflect the interplay of numerous biophysical and anthropogenic factors (Kuriakose et al., 2009; Negrete-Yankelevich et al., 2020), a wide array of seemingly disparate variables are correlated with soil characteristics and can be used to predict their spatial variation (Levi & Rasmussen, 2014; Miller et al., 2015; Lamichhane et al., 2019; Duarte-Guardia et al., 2019). Regional-to-global models leveraging these empirical associations (e.g., SoilGrids

Hengl et al., 2014, 2017; Global Soil Organic Carbon Map [GSOCmap], FAO & ITPS, 2020) are increasingly used as sources of soil information in disciplines outside of soil science (Fois et al., 2018; Eekhout et al., 2018; Fraval et al., 2018; Carlson et al., 2019; Sánchez-González et al., 2019; Dinerstein et al., 2019; Rozendaal et al., 2019; Waldman et al., 2019).

Several studies have estimated the spatial distributions of soil-mediated ecosystem services or proxies thereof (e.g., soil organic carbon [SOC] storage Tifafi et al., 2018, SOC dynamics (Guenet et al., 2018), and soil hydraulic properties Kearney & Maino, 2018; Trinh et al., 2018; Dai et al., 2019; Turek et al., 2020) using predictions from moderate–resolution (250 m–1 km), globally extensive models, particularly SoilGrids and the Harmonized World Soil Database (FAO/IIASA/ISRIC/ISSCAS/JRC, 2012). Exactly how these studies use global model predictions varies. For example, proxies for ecosystem services may be calculated or derived directly from model predictions (Zomer et al., 2017; Chappell et al., 2019) and compared with finer resolution, study-specific models (Mulder et al., 2016; Zhou et al., 2019; Szatmári et al., 2019; Chen et al., 2020; Silatsa et al., 2020) or used as inputs for mechanistic models (Rodríguez-Veiga et al., 2020). Alternatively, predictions from global models may themselves serve as predictors in new empirical models (Ramcharan et al., 2018; Liang et al., 2019).

While global soil models represent exciting progress towards the goal of spatially continuous soil information at fine to intermediate spatial resolutions (e.g., 30 m—1 km), products derived from these models inherently carry uncertainty and may be biased with regards to specific landscapes. Several phenomena limit confidence in soil model predictions (Hengl et al., 2019). These factors including errors in covariates (e.g., biased precipitation data in mountainous terrain Beck et al., 2020), omission of covariates (e.g., land-use history; Schulp & Verburg, 2009), insufficient representation of pedogenic factors by covariates (e.g., satellite-derived vegetation indices as proxies for organic carbon inputs [Hashimoto et al., 2011; Zeilhofer et al., 2012]), and the inherent shortcomings of relying on empirical—rather than mechanistic—relationships. Additionally, sampling bias may affect the reliability of predictions in particular landscapes. Although a large number of unique soil profiles are typically used in fitting gridded soil models (e.g., 196 498 profiles in the WoSIS database used for SoilGrids250m 2.0 as of October 2020

Batjes et al., 2019), these datasets consist of observations collected through many different sampling schemes, some spanning landscape-level variability more fully than others. Further uncertainty stems from the discrepancies between the spatial scale of gridded covariates (30 m–1 km) and point soil observations (< 1 m) (Hengl et al., 2019). Although some of these issues are unavoidable, researchers have reduced the uncertainty of national to regional soil models compared to global soil models by drawing on a wider range of covariates, selecting higher resolution (or more precise) versions of covariates unavailable for the entire globe, and training models using soil datasets with higher density of observations (Hengl et al., 2021).

Relatively few studies have evaluated predictions from regional to global soil models at finer (subnational) levels (Tewes et al., 2020; Krpec et al., 2020; Araujo-Carrillo et al., 2020). Critical assessment of model predictions against independent datasets at the landscape level is crucial both for (1) improving correlative representation of pedogenic processes in coarser empirical models (Hengl et al., 2017; McNicol et al., 2019) and (2) clarifying the utility of global soil model predictions for landscape–level ecosystem service research and management. In terms of pedogenesis, for example, mounting evidence underscores the importance of mineral weathering status for determining patterns in SOC storage and stabilization across landscapes (Matus et al., 2006; Chevallier et al., 2019; Inagaki et al., 2020), continents (Rasmussen et al., 2018; Heckman et al., 2020; von Fromm et al., 2020), and the globe (Kramer & Chadwick, 2018). However, landscape–level variation in weathering status is challenging to account for in a predictive framework due to the generality of geological covariates (e.g., 16 lithological classes in the Global Lithological Map database [Hartmann & Moosdorf, 2012] used as a predictor in the global SoilGrids model), the coarse resolution of topographic covariates (>30 m), and the lack of covariates related to the temporal dimension of soil formation (e.g., age of parent material; Slessarev et al., 2019). Similarly, global models rely on datasets with broadly defined land-cover types to represent anthropogenic factors, though field studies indicate that human impacts on soil properties and ecosystem service provision are often more directly related to land-use intensity and/or history than present-day land-cover type (Negrete-Yankelevich et al., 2020). Given the lack of standardized geospatial proxies for weathering status and land-use attributes, accounting for these drivers of edaphic variation in spatially extensive mapping efforts remains a major challenge.

To illustrate the need to evaluate the utility of predictions from soil models for understanding ecosystem service provision, consider the design and implementation of soil-based carbon sequestration programs (e.g., by governmental agencies or nongovernmental organizations). Readily available products derived from global models make it straightforward to create maps of SOC storage for individual landscapes. What information about SOC do such maps reveal? Do they provide estimates of present-day stocks, where each pixel represents the spatially weighted average of finer scale biophysical and anthropogenic effects on SOC? Are they more representative of one land-cover type than another, so that they may serve as an upper or lower baseline (Duarte-Guardia et al., 2019)? Even if biased, do they at least predict *relative* changes in SOC storage along environmental gradients (Tsui et al., 2013; Mora et al., 2014) or indicate areas where SOC storage is likely to respond to changes in management (Yadav et al., 2009)? If none of these are true, costly soil sampling and landscape–specific model development may be required to obtain actionable information.

In many research and management contexts, end–users of soils information may not have the option or interest in collecting new soil samples or building an entirely new model. Here, I evaluated practical strategies for such cases. In particular, I assessed whether additional insights into landscape–level soil variability could be gleaned by calibrating predictions from regional–to–global soil models using existing soils observations. To this end, I analyzed the magnitude, spatial trends, and uncertainty of SOC storage across a tropical montane landscape in a Bayesian hierarchical modeling framework. As a secondary objective, I evaluated the predictive power of spatially continuous versus site–specific covariates (e.g., weathering status and land–use history) using sparse partial least squares models (sPLS). Results of the proposed Bayesian model calibration approach and sPLS modeling were compared with two regional and two global soil models (250–1000–m resolution) to evaluate the landscape-level utility of uncalibrated model predictions.

3.2 Materials and methods

3.2.1 Study area

This study focused on a 7666-km^2 area at the intersection of the Trans-Mexican Volcanic Belt and the Sierra Madre Oriental in the states of Veracruz (92%) and Puebla (8%) in eastern Mexico (Fig. 3.1). While the study area makes up only 0.4% of Mexico's land area, the soil types within this area collectively cover 75% of the nation (in the FAO World Reference Base taxonomic system: Andosols, Arenosols, Fluvisols, Leptosols, Luvisols, Phaeozems, Regosols, and Vertisols; WRB, 2007; INEGI, 2013a). The majority of the study area is mantled by soils formed in volcanic parent materials, ranging from basaltic and andesitic lava flows to andesitic breccias, tuffs, rhyolitic ash, and geochemically diverse lahars (Negendank et al., 1985; Rossignol et al., 1992; Díaz-Castellón et al., 2012). These materials emanated from dozens of distinct volcanoes of varying size, from as long as 17 million years ago (Ma; Cantagrel & Robin, 1979) to as recently as 900 years before present (Siebert & Carrasco-Núñez, 2002; Rodríguez et al., 2010). The largest volcano within the study area is the 4282-m Cofre de Perote (*Nauhcampatépetl* in Nahuatl), a broad *shield-like* stratovolcano active from 1.3 to 0.2 Ma (Carrasco-Núñez et al., 2010). Non-volcanic parent materials include Cretaceous limestones of the pre-volcanic basement, isolated outcrops of Miocene sandstone and Pleistocene travertine towards the southeast, and aeolian and alluvial sediments along the coastal plain of the Gulf of Mexico (INEGI, 1984; Dubroeucq et al., 1992; Concha-Dimas et al., 2005; Servicio Geológico Mexicano, 2014).

A steep orographic climatic gradient extends from the Gulf to the east to the various volcanic landforms to the west and north and the high plain (*altiplano*) west of the Cofre. Mean annual potential evapotranspiration (PET) equals or exceeds mean annual precipitation (MAP, 900-1300 mm) near the coast, where the mean annual temperature (MAT) is 25 °C (Moreno-Casasola et al., 2009). MAP increases with elevation on the eastern side of the Cofre up to a maximum of approximately 3000 mm around 2000 m (Muñoz-Villers et al., 2012, 2016), declining to 1700 mm at 3000 m (Servicio Meterológico Nacional, 2017). MAT decreases by approximately 0.51–0.54 °C per 100–m increase in elevation. Descending west of the Cofre onto the altiplano, MAP decreases to approximately 400 mm (Dubroeucq et al., 1998). Precipitation is strongly seasonal, with approximately 80% of MAP falling in the four-month rainy season (June to September; Hernández et al., 2011; Muñoz-Villers et al., 2016). At intermediate elevations

(i.e., between the lifting condensation level and inversion layer, approximately 1200 to 3000 m), frequent fog immersion and associated precipitation maintain moist conditions throughout the dry season (Barradas et al., 2010; Alvarado-Barrientos et al., 2014), whereas sites at lower elevations and on the altiplano may experience pronounced dry-season desiccation (Rossignol et al., 1992). Prior to European colonization, the fog belt was occupied by tropical montane cloud forest (TMCF), with coniferous forest and grassland at higher elevations and on the altiplano, and tropical dry forest between the TMCF and the coast. In general, soil types along this bioclimatic sequence may be understood in terms of increasing weathering stage (e.g., neoformation of clay minerals, volumetric collapse) from Leptosols, Regosols, and silandic Andosols under coniferous forest and grassland to aluandic Andosols under upper elevation TMCF to andic Cambisols, Phaeozems, Luvisols, and Acrisols under lower elevation TMCF and tropical dry forest (Rossignol et al., 1992; Geissert et al., 1994).

Though much of the present–day landscape is covered by forest, modern anthropogenic disturbance has strongly altered ecosystem composition, structure, and function within the study area. Logging and conversion of TMCF and coniferous forest to pasture and row crops was relatively limited and localized throughout the eighteenth and nineteenth centuries but accelerated in the 1920s to 1940s with the advent of federal logging concessions (Hoffmann, 1989; Paré & Gerez, 2012). Extensive conversion of tropical dry forest to sugarcane and coffee plantations occurred earlier, beginning in the sixteenth and nineteenth centuries, respectively (Ponette-González & Fry, 2014). In recent decades, deforestation has continued alongside natural forest regeneration and reforestation efforts (Muñoz-Villers & López-Blanco, 2008; Von Thaden et al., 2021), such that the contemporary landscape is a mosaic of agricultural land uses (pasture, small-scale maize, large-scale potato, coffee agroforestry, sugarcane) and built infrastructure with forest patches that span a continuum of disturbance and succession (Williams-Linera et al., 2002; Toledo-Garibaldi & Williams-Linera, 2014; Von Thaden et al., 2019).

3.2.2 Field data

3.2.2.1 Soil sampling

I report previously unpublished SOC inventories and complementary physical and chemical properties for 58 soil profiles excavated in the headwaters of the Antigua river basin (820 km^2) on the eastern flank of the Cofre (1000–3000 m elevations). The profiles sampled in the Gavilanes subcatchment (41.3 km^2) spanned a range of landforms and forest cover), whereas the profiles sampled in the Pixquiac subcatchment (107.3 km^2) represented a gradient of disturbance and TMCF succession.

In the Gavilanes subcatchment, Dr. Daniel Geissert (Instituto de Ecología, A.C., Xalapa, Veracruz) sampled 42 profiles by genetic horizon to a maximum depth of 2.2 m across representative geomorphic units (delineated at a scale of 1:20000). This sampling design grouped land-use types into forest/nonforest classes and included a series of catenas (local hillslope sequences) distributed along the broader elevation gradient (Geissert et al., 2013).

In the Pixquiac subcatchment, I excavated eight profiles within each of two altitudinal bands at the lower and upper limits of the TMCF ecosystem (1350-1550 and 2050-2220 m, respectively). These profiles represented a common sequence of disturbance and succession, from primary forest (selectively logged but never clearcut) to pasture to fallow and secondary forest. Sites were selected on the basis of grazing history as described by landowners and constrained to similar topographic settings (planar to convex backslopes with local slope gradients from 25 to 45 degrees). Profiles were sampled by genetic horizon and in depth intervals (0–2, 2–4, 4–6, 6–8, 8–10, 10–15, 15–25, 25–40, 40–60, 60–80, 80–100 cm) to a depth of 1 m, with the exception of one profile with fragmented bedrock at 60 cm.

Samples were sieved to remove materials larger than 2 mm. Bulk density (oven-dry mass of fine-earth fraction per unit *in situ* volume) was estimated using the core method (Blake & Kartge, 1986). Carbon and nitrogen concentrations were determined on the fine-earth fraction via dry combustion (Nelson & Sommers, 1996). Particle size distributions were determined via the pipette method after oxidation of organic matter with hydrogen peroxide for the Gavilanes profiles and subsoil (B horizon) samples of the Pixquiac profiles. Depth interval samples from

the Pixquiac profiles were also analyzed using a laser diffraction particle size analyzer; however, due to poor agreement between laser diffraction and pipette methods in this landscape (e.g., R^2=0.3 for laser diffraction-predicted clay content after optimized rebinning of laser diffraction particle size boundaries via a genetic algorithm, n = 98), I do not report particle size data for the Pixquiac profiles in this study. I measured soil pH in water (1:1) and potassium chloride and sodium fluoride solutions (1 N concentration each) to characterize soil chemistry and colloidal reactivity (Fieldes & Claridge, 1975; Pansu & Gautheyrou, 2006). Additionally, I quantified concentrations of aluminum, silicon, and iron extracted by acid-ammonium oxalate using atomic absorption spectroscopy to estimate the abundance of poorly crystalline mineral phases, such as allophane, imogolite, and ferrihydrite, as well as metal-humus complexes (McKeague & Day, 1966).

3.2.2.2 Published soil observations

Data for an additional 77 profiles sampled within the broader landscape were obtained through an extensive search of national and global databases, peer–reviewed literature, undergraduate and graduate theses, and project reports. Minimum criteria for inclusion were explicit geographic coordinates, values for carbon content (measured via dry combustion or estimated from organic matter content measured with loss–on–ignition or wet oxidation methods; Walkley & Black, 1934), and a sampling depth of at least 30 cm. A total of 28 profiles in the study area met these criteria in the databases of the Mexican National Institute of Statistics and Geography (INEGI; five profiles in INEGI, 2004 and nine in INEGI, 2013a) and the International Soil Carbon Network (ISCN, Zinke et al., 1986; Nave et al., 2016; Malhotra et al., 2019). Different subsets of profiles from these same databases were used in training the regional–to–global models that I evaluated in this study. Consequently, SOC inventories calculated for these 28 profiles cannot be considered as independent validation of model predictions but serve to extend spatial coverage in the model calibration process. Note that most these profiles also appeared in the World Soil Information Service (WoSIS) database (Batjes et al., 2017, 2019), but I worked with the aforementioned sources to obtain additional profiles and metadata. Data from another 49 profiles were acquired from Geissert et al. (1994) (n=16), Meza Pérez (1996) (n=9), Gamboa & Galicia, 2012 (n=15), Aguilar Orea (2013) (n=8), and Muñoz-Villers et al. (2020) (n=1).

3.2.2.3 Horizon– and profile–level calculations

I took the following steps to calculate the storage of SOC within mineral soils (excluding organic horizons) to a depth of 30 cm and from 30 to 100 cm for profiles with observations to that depth.

I calculated the stock of SOC within horizon *i* as

$$S_{C,i} = c_{C,i}\rho_{b,i}\Delta z_i 10, \tag{3.1}$$

where $c_{C,i}$ is the mass fraction of organic carbon (i.e., percent carbon/100), $\rho_{b,i}$ is oven-dry bulk density (g cm^{-3}), Δz_i is the thickness of layer *i* (cm), and the factor of 10 converts the stock to units of kg m^{-2}.

Next, I determined the cumulative inventory of SOC at the bottom of the nth horizon through summation:

$$I_C = \sum_{i=1}^{n} S_{C,i}. \tag{3.2}$$

The cumulative inventory I_C was then calculated at the base of each horizon within each profile. To compare observed inventories with inventories predicted for standardized depth intervals by regional–to–global models (e.g., 0–30 and 0–100 cm), either I_C or the variables used to calculate it (c_C and ρ_b) must be interpolated. In the case of this study, initial interpolation of c_C and ρ_b with equal–area splines (Bishop et al., 1999; Malone et al., 2009; Hengl, 2020) yielded results virtually identical to I_C values interpolated with cubic splines (Pearson correlation coefficients 0.999 and 0.998 for 0–30 and 0–100 cm intervals, respectively). Results from the former approach were used for the remainder of this study.

For all profiles, I assumed that reported total carbon values represented organic carbon, with negligible carbon present as carbonate. This assumption of lack of carbonates was supported by unpublished thermal analyses and lack of effervescence of the Pixquiac samples upon application of 10% HCl. The soils included in the published datasets were generally acidic (typical soil pH in water < 5.5), and none were underlain by limestone parent material. Given the possible occurrence of carbonates in the driest parts of the landscape (e.g., subsoil horizons in altiplano profiles; Dubroeucq et al., 1998), organic carbon in those areas may be slightly overestimated by using total carbon. Where organic matter content (OM) was reported rather than carbon concentration (58 horizons), I estimated c_C assuming that organic matter contained 58% carbon by mass (i.e., %C = 0.58 OM; but see Pribyl, 2010). Depths were adjusted for profiles including

organic horizons to assign a depth of zero to the top of the mineral soil for comparability across data sources.

Bulk density (ρ_b) values were missing for 91 of the 454 horizons. Incomplete ρ_b observations pose a pervasive challenge when working with soil data from diverse sources(Sequeira et al., 2014). Missing ρ_b values are often estimated using empirical relationships (or"pedotransfer functions" [PTFs]) to predict ρ_b on the basis of OM or c_C, sometimes in conjunction with soil texture data (Hiederer & Köchy, 2011; Minasny & Hartemink, 2011; Sequeira et al., 2014; Sanderman et al., 2017). When estimates of ρ_b are used in lieu of measurements in the calculation of SOC inventories, spatial predictions of SOC storage carry additional uncertainty (Guevara et al., 2020). To mitigate that source of uncertainty in my modeling, I primarily focused on my analyses on profiles with measured ρ_b. However, to obtain SOC inventories for the full set of profiles and maximize spatial coverage, I applied a Bayesian approach to predict ρ_b and propagate associated uncertainty through (3.1) and (3.2). Characterizing the potential bias and uncertainty incurred from the use of PTFs was also important to my larger objectives because the models I evaluated in this study were trained on the INEGI profiles, which require estimation of ρ_b (see Guevara et al., 2020 for a systematic treatment). I estimated ρ_b where missing using a physical PTF (Stewart et al., 1970; Adams, 1973):

$$\rho_b = \frac{100}{\frac{OM}{\rho_{b,o}} + \frac{100-OM}{\rho_{b,m}}}. \tag{3.3}$$

In theory, the parameters $\rho_{b,o}$ and $\rho_{b,m}$ represent the respective bulk densities of the pure organic and mineral fractions. Fixed values of both parameters (e.g., the original values estimated by Adams, 1973 or later estimates obtained with larger datasets, e.g., De Vos et al., 2005; Lettens et al., 2005) are often used, but these values may be poorly suited for soils within particular landscapes due to inherent pedologic differences (e.g., mineralogy, degree of organic matter decomposition). For example, for forest soils formed in volcanic parent materials across all of Japan (n=3513), nonlinear least squares–estimates of $\rho_{b,o}$ and $\rho_{b,m}$ were substantially lower than the widely used estimates originally obtained for non-volcanic soils (e.g., the mudstone–derived soils Adams, 1973 studied in Wales; Nanko et al., 2014). To use (3.3) to predict the 91 missing values of ρ_b in this study, I first estimated $\rho_{b,o}$, $\rho_{b,m}$, and the error variance σ^2 using OM (again assuming OM=%C/0.58) and ρ_b for the 363 complete horizon–level records. The posterior distributions of each parameter were sampled using Markov chain Monte Carlo (MCMC) as

implemented in the `rjags` package (Plummer, 2019) in the `R` statistical computing environment (R Core Team, 2018), version 3.5.2. I then compared the resulting posterior predictive distributions (PPDs) of $\rho_{b,o}$ and $\rho_{b,m}$ with estimates for all other Andosols (and soils likely formed in volcanic materials) present in WoSIS and the International Soil Radiocarbon Database (ISRaD; Lawrence et al., 2019). Finally, for each profile missing one or more values of ρ_b, I predicted ρ_b and calculated I_C for each set of MCMC samples, yielding profile–level distributions of I_C that conveyed the uncertainty imparted by estimating ρ_b.

The fraction of soil volume occupied by coarse fragments is another source of uncertainty in estimates of I_C (Poeplau et al., 2017). Nonetheless, I chose not to adjust ρ_b or SOC inventories for coarse fragments (beyond sieving to remove their mass contributions) for three reasons. First, my observations in the Gavilanes and Pixquiac catchments indicated low abundance of coarse fragment on a mass basis (median: 0.008 g coarse fragments per g soil plus coarse fragments for Pixquiac samples). Second, estimating volumetric abundance of coarse fragments from mass abundance requires assuming a constant coarse fragment density (Alexander, 1982). This assumption is unrealistic in this context, as coarse fragments spanned a wide range of weathering statuses (e.g., highly fragmented brecchias and tuffs versus solid andesites). Third, methodological descriptions and the basis for data reporting were inconsistent among the published soil datasets. Comparison of SOC inventories as calculated in this study with coarse fragment–adjusted SOC inventories reported in the original data sources (Gamboa & Galicia, 2012) suggested that this omission did not likely impart major errors, notwithstanding clear potential for overestimation in particularly rocky areas.

For profiles with data for additional soil properties, I estimated cumulative inventories of other properties measured on a mass basis (nitrogen, clay, silt, sand, and oxalate-extractable aluminum, silicon, and iron) in the same way as for I_C. pH over each depth interval was summarized in terms of depth–weighted averages. In this study, I used these properties as potential site–specific covariates (e.g., indicators of local edaphic variation) in the sPLS analysis.

3.2.3 Regional–to–global SOC products

I assessed landscape–level predictions of SOC storage from four products developed over broader extents at intermediate–to–coarse spatial resolutions (250–1000 m) relative to many landscape–specific models (e.g., <30 m). I compared two models developed by Guevara, Vargas, and

colleagues (Guevara et al., 2020; Guevara & Vargas, 2020) as part of the NASA Carbon Monitoring System (CMS), SoilGrids250m 2.0 (Hengl et al., 2014, 2017; Poggio et al., 2021) of the International Soil Reference and Information Centre (ISRIC–World Soil Information), and the Global Soil Organic Carbon Map (GSOCmap) of the Food and Agriculture Organization (FAO) of the United Nations.

The first of the two CMS products (hereafter CMS30; Guevara et al., 2020) consisted of SOC inventories predicted to a depth of 30 cm at a spatial resolution of 250 m across Mexico and the continental United States. Predictions were generated using random forest models (Breiman, 2001) with predictors (covariates) selected through a simulated annealing procedure. Models were fit separately for profiles sampled within different periods of time (1991–2000, 2001–2010, and 1991–2010; in this study, I assessed predictions from the model for the 1991–2010 period). Profiles were extracted from the ISCN (Nave et al., 2016) and INEGI databases (INEGI, 2004, 2013a). Uncertainty from the use of different pedotransfer functions was assessed, and errors in SOC predictions for independent validation data were mapped with quantile random forest regression (Meinshausen, 2006).

The second CMS product (hereafter CMS100; Guevara & Vargas, 2020) represented SOC inventories to a depth of 100 cm at a spatial resolution of 90 m. These predictions were also generated using random forest models, which in this case were trained on 2852 profiles sampled by INEGI between 1999 and 2009 (INEGI, 2013a). Prediction uncertainty was quantified through cross–validation and interpolated as a function of environmental covariates.

The SoilGrids250m 2.0 platform (hereafter SoilGrids; Hengl et al., 2014, 2017; Poggio et al., 2021) predicts several soil physical and chemical properties in multiple intervals to a maximum depth of 200 cm at 250–m spatial resolution. The version of SoilGrids assessed in this study (Poggio et al., 2021) was created using quantile random forest models trained on profiles in the WoSIS database (196 498; Batjes et al., 2019), with the uncertainty of each property expressed in terms of the predicted 5% and 95% quantiles. SOC inventories for the 0–30 cm interval (hereafter SG30) were included in this version of SoilGrids. I calculated SoilGrids–predicted SOC inventories to 100 cm (hereafter SG100) from the carbon density product (i.e., the product of c_C and ρ_b) following (3.1) and (3.2) and obtained uncertainties by repeating this process with the predicted 5% and 95% quantiles of carbon density.

The GSOCmap was produced through an international collaboration led by the FAO through the Intergovernmental Technical Panel on Soils and the Global Soil Partnership Secretariat (FAO

& ITPS, 2020). For GSOCmap v1.5.0, SOC inventories for the 0–30 cm interval were predicted at 1000–m spatial resolution with country–specific approaches, as each participating country was responsible for the acquisition, standardization, and regionalization of data within its borders. Predictions for Mexico within GSOCmap (the Soil Organic Carbon Map of Mexico, 2017) were generated through a hybrid approach using both expert–knowledge and linear regressions with 36 015 soil observations (profiles and auger samples). Multiple domestic and international academic, governmental, and nongovernmental institutions contributed to the Mexican portion of GSOCmap (FAO & ITPS, 2020).

3.2.4 Statistical analyses

I employed two types of models to evaluate strategies for improving predictions of SOC inventories at the landscape level when additional sampling and/or data–intensive modeling are not feasible. First, I used Bayesian hierarchical modeling to calibrate predictions from spatially extensive SOC products and gain insights into local spatial patterns and uncertainties. Then, with sparse partial least squares (sPLS) models, I critically compared the predictive utility of spatially extensive geospatial covariates—including SOC products as well as primary data—and covariates with limited extent/scalability (high–resolution geospatial covariates and field data).

3.2.4.1 Bayesian hierarchical modeling

In calibrating SOC predictions from existing soil models, I sought to reduce the overall landscape–level bias of predictions while also improving fidelity to observed sub–landscape spatial structure. To this end, I analyzed the relationship between observed and model–predicted SOC inventories with two spatial random effects (SRE) models. The first model yielded calibrated predictions of SOC inventories in the 0–30 cm interval while quantifying the uncertainty of parameters and predictions. The second model jointly predicted SOC inventories in the 0–30 and 30–100 cm intervals, exploiting the profile–level covariance of top- and subsoil SOC storage to improve confidence in predictions where observations were available for the upper interval but not the lower. In essence, both models can be considered extensions of the simplest possible (nonnull) relationship between observed $y(\mathbf{s})$ and model–predicted SOC inventories $x(\mathbf{s})$ over

a given depth interval for a set of locations **s** (e.g., geographic coordinates) within a landscape:

$$y(\mathbf{s}) = \beta_0 + \beta_1 x(\mathbf{s}) + \epsilon(\mathbf{s}). \tag{3.4}$$

If the model that generated $x(\mathbf{s})$ were unbiased and fully represented the spatial structure of $y(\mathbf{s})$, the intercept β_0 would be zero, the slope coefficient β_1 would be one, and differences between $x(\mathbf{s})$ and $y(\mathbf{s})$ would be encompassed by the error term $\epsilon(\mathbf{s})$ (i.e., $\epsilon(\mathbf{s}) = y(\mathbf{s}) - x(\mathbf{s})$), representing by non-spatial random variability. Bias in $x(\mathbf{s})$ with respect to a particular landscape will affect the overall values of β_0 and β_1, while spatial structure unexplained by $x(\mathbf{s})$ will be reflected by autocorrelation in $\epsilon(\mathbf{s})$. I used SRE models to address both issues, given their capacity to estimate how $y(\mathbf{s})$ varies spatially not only in relation to $x(\mathbf{s})$, but also due to spatial variation in the parameters themselves. Applying SREs in a Bayesian framework (as opposed to using kriging and its variants in a frequentist mode) offered the major advantage of characterizing the respective uncertainties of all parameters involved (spatially varying model parameters and parameters related to spatial autocovariance) as well as the uncertainty of the resulting calibrated predictions (Finley et al., 2015).

3.2.4.1.1 Calibration of predicted SOC inventories in the 0–30 cm interval

I fit an SRE model to calibrate model–predicted SOC inventories in the 0–30 cm depth interval using the observed inventories (calculated with the soil profile data and interpolated to a standard depth). Observed inventories were square–root–transformed prior to model fitting to ensure the non–negativity of calibrated predictions. Preliminary models were built to compare differences in predictive power between the two higher–resolution products (SG30 and CMS30) and several alternative parameterizations. The full model was of the form:

$$y(\mathbf{s}) = (\beta_0 + w_0(\mathbf{s})) + (\beta_1 + w_1(\mathbf{s}))x_{MOD}(\mathbf{s}) + \epsilon(\mathbf{s}), \tag{3.5}$$

where $x_{MOD}(\mathbf{s})$ denotes the SOC inventory predicted for location **s** by either CMS30 or SG30 and $w_0(\mathbf{s})$ and $w_1(\mathbf{s})$ are SREs on the intercept and slope, respectively. In all candidate models in which they appeared, $w_0(\mathbf{s})$ and $w_1(\mathbf{s})$ were modeled as univariate Gaussian processes, assuming that the covariance between two locations decayed exponentially as a function of the distance between them, regardless of their specific positions within the landscape. Note that two parameters controlling the Gaussian process must be estimated for each SRE included in

the model; hence, seven parameters must be estimated for (3.5), including the variance of the residual error).

Vague prior distributions were specified for each parameter, as in Babcock et al. (2015). I assumed that β_0 and β_1 followed normal distributions and the spatial and residual variance parameters followed inverse-Gamma distributions. The correlation decay parameter(s) of the SRE(s) were assigned uniform distributions. I used MCMC sampling (Gelman et al., 1995) to estimate the parameters of (3.5) for different subsets of profiles: the 28 profiles appearing in the INEGI and ISCN databases, the 101 profiles with complete ρ_b measurements (including 11 from ISCN but none from INEGI), and the full set of 135 profiles. For profiles for which ρ_b was estimated using (3.2), resulting in uncertainty in SOC calculations, I used the median value of the distribution of SOC inventory estimates for modeling. MCMC sampling was conducted with the `spBayes` package in (Finley et al., 2015; Finley & Banerjee, 2020). Chains were run for 15000 iterations each; I retained 5000 thinned samples per chain for inference.

3.2.4.1.2 Joint prediction of SOC inventories in the 0–30 and 30–100 cm intervals

With the second Bayesian model, I took a coregionalization approach to predict SOC inventories in two depth intervals (0–30 and 30–100 cm) simultaneously. I used a coregionalization model, rather than fit separate models for both intervals, because fewer profiles in my dataset included sufficient data to calculate SOC storage for the deeper interval (n=70 with measured ρ_b), as is often true when compiling data from heterogeneous sources. Bayesian coregionalization allowed me estimate the covariation of SOC inventories within the two different depth intervals and then use the more ubiquitous observations for the 0–30 cm interval to guide predictions of SOC inventories to 100 cm. I used the following model parameterization to predict log–transformed inventories in both intervals on the basis of the CMS– and SoilGrids–predicted SOC inventories for the upper interval (CMS30 and SG30, respectively):

$$\begin{bmatrix} y_{0-30}(\mathbf{s}) \\ y_{30-100}(\mathbf{s}) \end{bmatrix} = \begin{bmatrix} \beta_{0,y_{0-30}} + \beta_{1,y_{0-30}} x_{CMS30}(\mathbf{s}) + \beta_{2,y_{0-30}} x_{SG30}(\mathbf{s}) \\ \beta_{0,y_{30-100}} + \beta_{1,y_{30-100}} x_{CMS30}(\mathbf{s}) + \beta_{2,y_{30-100}} x_{SG30}(\mathbf{s}) \end{bmatrix} + \mathbf{A} \begin{bmatrix} u_{y_{0-30}}(\mathbf{s}) \\ u_{y_{30-100}}(\mathbf{s}) \end{bmatrix} + \begin{bmatrix} \epsilon_{y_{0-30}}(\mathbf{s}) \\ \epsilon_{y_{30-100}}(\mathbf{s}) \end{bmatrix}. \tag{3.6}$$

The first term on the right–hand side represents spatially constant relationships between model–predicted and observed SOC inventories, with depth–interval–specific coefficients. The

SREs in this model—$u_{y_{0-30}}(\mathbf{s})$ and $u_{y_{30-100}}(\mathbf{s})$—are modeled as Gaussian processes and had an effect analogous to $w_0(\mathbf{s})$) in (3.5). The matrix $\mathbf{A}$ is mathematically related to the variance–covariance matrix of the two SRE terms and functions as a link between the two depth intervals. The parameters of (3.6) were estimated similarly as for the previous model (101 profiles with values the upper interval, 70 with the lower). Samples from the posterior predictive distributions of the two log–transformed inventories were backtransformed and summed for inference and mapping of SOC inventories for the full 0–100 cm interval.

3.2.4.2 Sparse partial least squares analysis

I used sPLS to address two alternative types of information for making landscape–level inferences on SOC storage. Like principal components analysis and other ordination techniques, partial least squares modeling approximates high–dimensional data through projection to a low–dimensional subspace. In doing so, partial least squares maximizes the covariance between a matrix of covariates and one or more response variables (i.e., a vector in mode 1 or a matrix in mode 2). sPLS extends generic partial least squares by penalizing the number of covariates that load on the latent factors defining the low–dimensional subspace and readily accommodates missing data and small sample sizes. Here, I used sPLS to select a parsimonious set of covariates that maximally covary with SOC inventories in the 0–30 interval (mode 1) and in both the 0–30 and 30–100 cm intervals (mode 2) from a wider array of potential proxies. With these intentionally simplistic models, I assessed whether:

1. widely available geospatial covariates, in conjunction with landscape–specific soils data, could predict SOC inventories as well as—or better than—more sophisticated soil models, and/or

2. covariates with limited spatial extent (high–resolution geospatial covariates or field data) offered substantial improvements in landscape–level predictions.

To investigate these possibilities, I fit sPLS models that selected from covariates in the first group only (including SOC predictions from CMS30, CMS100, SG30, SG100, and GSOCmap) and from covariates in both groups. The latter group included variables with missing values for some observation. In the case that these variables were selected as covariates in the model, their effect when missing was set to zero. Leave–one–out cross–validation did not indicate major

gains in predictive power with increasing number of latent factors; hence, for greater model interpretability, I chose to retain only two latent factors and allowed one covariate to load on each. Models were fit using `mixOmics` version 6.6.2 (Rohart et al., 2017) in `R` after center and scaling all covariates.

3.3 Results

3.3.1 Soil properties and SOC storage

3.3.1.1 Field data

Soil carbon concentration (c_C) and bulk density (ρ_b), both necessary to estimate SOC inventories, varied widely across the biophysical and anthropogenic gradients represented by the 135 profiles. Values reported for horizon–level c_C (presented here as percentages for clarity) ranged from 0.11% to a maximum of 32.4%, with a median of 7.3% (mean: 8.4%). Several observations exceeded the taxonomic definition of mineral soil (>25%) but were included in my analysis based on reported morphological classifications. ρ_b reached values as high as 1.9 g cm^{-3} but was generally low, with a median of 0.52 g cm^{-3} (mean: 0.59 g cm^{-3}, minimum: 0.17 g cm^{-3}). To predict ρ_b where missing, I estimated the bulk density of the purely organic and purely mineral fractions, $\rho_{b,o}$ and $\rho_{b,m}$ (the parameters of (3.3)), and obtained median values that agreed well with published estimates for an extensive set of volcanic soils in Japan (Nanko et al., 2014; Table 3.1; Fig. 3.2). In fact, I found that the latter parameter values predicted ρ_b for my dataset nearly as well as the parameters I estimated on that same dataset (root–mean–square error [RMSE]: 0.199 versus 0.196 g cm^{-3}, respectively, compared to 0.475 g cm^{-3} using parameters from Adams, 1973). However, median relative errors indicated that using parameters from either Nanko et al. (2014) or Adams (1973) would systematically overestimate ρ_b in the study area (12 and 56%, respectively).

The median SOC inventory in the profiles that did not require estimation of ρ_b was 14.7 kg m^{-2} in the upper 30 cm of mineral soil (mean: 15.9 kg m^{-2}; minimum: 1.7 kg m^{-2}; maximum: 46.3 kg m^{-2}) and 27.3 kg m^{-2} in the upper 100 cm (mean: 30.9 kg m^{-2}; minimum: 2.7 kg m^{-2}; maximum: 78.0 kg m^{-2}; Table 3.2). For the remaining 34 profiles (denoted *PTF* in Table 3.2), the uncertainty in ρ_b due to its estimation on the basis of organic matter (or carbon) content was propagated through the calculation of SOC inventories, giving a distribution of possible SOC

inventories for each depth interval and profile. The median uncertainty of these distributions, expressed as the 95% credible interval width, was 3.4 kg m^{-2} for SOC inventories in the 0–30 cm interval and 8.5 kg m^{-2} in the 0–100 cm interval.

3.3.1.2 Regional–to–global SOC products

Across the full study area, median SOC inventories predicted by CMS, SoilGrids, and GSOCmap were 3.9, 5.5, and 4.1 kg m^{-2}, respectively, for the 0–30 cm interval. For the 0–100 cm interval, CMS predicted a median inventory of 8.4 kg m^{-2}, and the median value I derived from SoilGrids–predicted carbon density (delivered on a finer interval basis) was 12.3 kg m^{-2}. CMS, SoilGrids, and GSOCmap respectively predicted maximum inventories (not including uncertainties) of 8.1, 18.5, and 13.5 kg m^{-2} for 0–30 cm; predicted maxima for 0-100 cm were 31.2 kg m^{-2} (CMS) and 35.8 kg m^{-2} (SoilGrids). Predicted minima were 1.9 (CMS), 2.9 (SoilGrids), and 0.6 (GSOCmap) kg m^{-2} for 0–30 cm and 3.8 (CMS) and 8.6 (SoilGrids) kg m^{-2} for 0–100 cm.

For the pixels that included the study profiles, predictions from CMS and SoilGrids showed moderate agreement with trends observed across profiles, but with significant differences in magnitude. Across all profiles, inventories predicted for the 0–30 cm interval by CMS and by SoilGrids were similarly correlated with observations (Pearson correlation coefficients: 0.49 and 0.46, respectively), whereas the correlation with GSOCmap was negligible (0.06). SoilGrids predictions for the 0–100 cm interval were more strongly correlated with observations (0.46) than were those of CMS (0.34). Assessing relationships separately for profiles included in the databases used in model development (together with thousands of other profiles) versus observations from independent studies, I detected suggestive evidence that model predictive performance may differ between the two groups (Figs. 3.3 and 3.4). However, the relationship between observed and predicted SOC inventories was not significantly different between groups (p value for interaction term on slope: 0.26 for CMS, 0.16 for SG30 excluding a single outlier but 0.003 including the outlier), after accounting for the difference in respective group means.

3.3.2 Bayesian hierarchical modeling

I evaluated two alternative spatial random effect (SRE) model structures: one model (3.5) to calibrate existing predictions of SOC inventories in the 0–30 cm interval and another model (3.6)

to jointly predict inventories in the 0–30 and 30–100 cm intervals, again on the basis of existing predictions. Fitting the spatially varying coefficient model (3.5) with observations from the same databases originally used to train the model (INEGI and ISCN) recovered a linear bias but essentially no additional spatial structure (Fig. 3.5 left; compare to upper right panel in Fig. 3.3). When the model was fit with profiles from independent studies, the overall effect was a nonlinear calibration (Fig. 3.5 center); areas originally predicted to have the lowest SOC inventories were scaled down, while areas with the highest original predictions underwent a much larger increase than in the linear case. Including both sets of profiles yielded an intermediate outcome (Fig. 3.5 right). Spatial comparison of the original CMS predictions with predictions calibrated using the model fit to the full set of profiles (Fig. 3.6) revealed that, in addition to a multiplicative rescaling of predicted values, the calibration resulted in the growth of areas with extreme predictions (both high and low). For example, inventories predicted for the altiplano on the leeward side (leftmost portion of each panel in Fig. 3.6) of the Cofre de Perote volcano had greater relative spatial variability (local structure) when assessed with CMS but were predicted to be more uniformly low after calibration. A similar phenomenon was observed at low elevations on the windward side (rightmost portion of each panel in (Fig. 3.6), while an opposite change occurred at intermediate elevations. For each of the spatially varying coefficient models, broad posterior predictive distributions for parameters and for calibrated SOC inventories indicated the need for more rigid specification of priors, given the limited size of the dataset.

Despite the added complexity of predicting multiple response variables (SOC inventories in 0–30 and 30–100 cm intervals), estimating the parameters of the coregionalization model proved to be more feasible than for the spatially varying coefficient model with the limited size of the soil profile dataset. A major advantage of this model structure was its capacity to improve predictions of deeper (30–100 cm) inventories where only shallow (0–30 cm) inventories were observed. This feature of the model involved estimation of the covariation of the spatial random effects of both intervals. Figure 3.7 (left panel) illustrates the posterior predictive distribution of the correlation between the random effects on the shallow and deep inventories, which was derived from estimates of the matrix parameter **A** in (3.6)). I found that coregionalization faithfully reconstructed the observed relationship between SOC inventories in the upper and lower soil (Fig. 3.7, right).

Spatial patterns in predicted SOC storage to 100 cm (Fig. 3.8, left; estimated by summing predictions for the upper and lower intervals) followed similar trends as calibrated predictions for

the upper soil (Fig. 3.6, right), which would be expected given the correlation of upper and lower soil SOC inventories. However, prediction uncertainties were poorly constrained. In absolute terms, the greatest uncertainty in predicted SOC inventories (represented by the 95% credible interval width [CIW]) was 207 kg m^{-2} for the 0–100 cm interval (Fig. 3.8, right), well in excess of observed SOC inventories. The median 95% CIW for predictions to 100 cm across the study area was 39 kg m^{-2}. Uncertainty relative to the magnitude of predicted values (95% CIW/median predicted value) was structured spatially in relation to the distribution of the profiles used in fitting the model; for example, uncertainties were especially large at lower elevations and towards the south where data availability was lowest. Minimum prediction uncertainty increased (i.e., the most precise predictions became increasingly uncertain) as a function of distance from observations (Fig. 3.9), but uncertainty was generally high even at closer locations.

3.3.3 sPLS analysis

My simple application of sPLS modeling consisted of four models, two of which were constrained to select two spatially continuous variables from a large array of climatic, topographic, and vegetation–related covariates, and another two models which were allowed to select from additional site–specific covariates. All four models highlighted correlations between SOC inventories and broad climatic variation (Table 3.3). Of the five covariates selected, three were spatially continuous climate products (all 1–km spatial resolution): bias–corrected mean annual precipitation (MAP_{bc}), mean annual temperature (MAT), and the ratio of mean annual potential evapotranspiration to MAP_{bc} (aridity index, AI_{bc}). Either MAP_{bc} or AI_{bc} was selected as the covariate explaining the most variation in SOC inventories in each of the four models. Covariates selected for the second factor were identified as best explaining the residual variation in SOC after accounting for the first factor. Besides MAT, the only other spatially continuous product selected was the CMS product for SOC inventories in the 0–100 cm interval (referred to as CMS100 in this study; 90–m spatial resolution; Guevara & Vargas, 2020). Of the less scalable, more site–specific covariates considered (e.g., 5 m–resolution terrain attributes and land-surface phenology parameters; historical canopy cover class inferred from aerial and satellite imagery since 1966), the only covariate selected was oxalate–extractable iron (Fe_o). Fe_o data were available for 75 of the 101 profiles included in the sPLS analysis. Note that I included mass inventories of Fe_o for both depth intervals in the pool of potential covariates, but only the upper interval was selected by the models.

3.4 Discussion

3.4.1 The geography of SOC storage in the study area

The 135 profiles analyzed in this study spanned a wide range of biophysical conditions and represented varying degrees of anthropogenic disturbance. Out of the variables I evaluated as potential empirical proxies for the biophysical and anthropogenic factors that influence SOC storage, surrogates for site water balance (MAP_{bc} and AI_{bc}) emerged as the strongest predictors (Table 3.3). Simple linear regression confirmed the sPLS–based finding that AI_{bc} predicted SOC inventories in the 0–30 cm interval marginally better than MAP_{bc} (R^2: 0.37 versus 0.35; RMSE of prediction: 7.0 versus 7.1 kg m^{-2} in leave–one–out cross–validation). Though not selected by sPLS, I also found that mean cloud frequency (1–km product derived from MODIS imagery; Wilson & Jetz, 2016) was similarly effective as a predictor of upper soil SOC storage (R^2: 0.35; RMSE of prediction: 7.1 kg m^{-2}). Note that this same cloud frequency product was used in the creation of the bias correction factors (Beck et al., 2020) that I applied to the precipitation data, possibly contributing to the improved predictive performance of corrected versus uncorrected MAP (R^2: 0.29; RMSE of prediction: 7.1 versus 7.4 kg m^{-2}).

Regardless of which variable most closely approximates moisture availability, the finding of covariation between SOC inventories and MAP_{bc} or AI_{bc} is unsurprising, considering the mechanistic role that moisture plays in mediating rates of net primary productivity and mineralization (von Lützow & Kögel-Knabner, 2009). In mountainous landscapes, where elevation and relief drive sharp gradients in temperature and moisture, systematic altitudinal patterns in SOC inventories are ubiquitous (Alexander, 1982; Powers & Schlesinger, 2002; Djukic et al., 2010; Ping et al., 2013; Mora et al., 2014; Tashi et al., 2016). Simultaneous covariation of climatic, geologic, pedologic, and biotic factors along elevation gradients limit the scope of causal inferences (Körner, 2007; Nottingham et al., 2015) but may indeed be advantageous for the purpose of landscape–level soil mapping. In volcanic landscapes, the spatial signature of climate on SOC storage tends to be further reinforced by the climate–dependent chemical weathering of volcanic ejecta (Chartres & Pain, 1984; Dahlgren et al., 1997; Meijer & Buurman, 2003; Tateno et al., 2019) and associated formation of SOC–stabilizing (organo)mineral phases (Parfitt, 2009; Chevallier et al., 2010; Takahashi & Dahlgren, 2016). These weathering products have been cited to explain the lack of significant change in SOC inventories in response to land–use change (Gamboa & Galicia, 2012).

Previous profile–based analyses within the study area (Campos C. et al., 2007; Gamboa & Galicia, 2012; Romero Uribe, 2017) and at the state level (Campos C. et al., 2014) provide strong evidence that mesoscale climate and/or climatically mediated mineral weathering more directly influence the magnitude and spatial patterns of SOC inventories in this pedologic setting than other biophysical or anthropogenic factors (e.g., parent material or land use). Hence, I expected that SOC predictions from regional–to–global models informed by gridded climate products (and satellite–derived metrics representing the response of vegetation to climate) may approximate the trends observed in this landscape reasonably well. In comparing these predictions with observed SOC inventories, I found general qualitative agreement for landscape–level trends: models predicted that SOC inventories moving westward from the Gulf of Mexico up the Cofre de Perote volcano and decreased on the altiplano west of the Cofre (Fig. 3.10), as evident in the 135 profiles (Fig. 3.11, top panel). However, models differed in both the magnitude of predictions (see Section 3.3.1.2) and in the environmental context they predicted to have the greatest SOC storage. For example, SoilGrids predicted that SOC inventories reached a maximum value at intermediate elevations (approximately 60 km from the coast in Fig. 3.10), whereas CMS predicted maximum values at the highest elevations. Furthermore, SoilGrids predicted a sharper decline west of the Cofre (i.e., descending onto the altiplano) than did CMS.

In more quantitative terms, I detected significant positive relationships between observed SOC inventories in the 0–30 cm interval and predictions from SoilGrids and CMS, but not GSOCmap. However, even after adjusting for systematic underestimation (e.g., linear model slope coefficients: 2.7 ± 0.5 and 2.9 ± 0.6 for SoilGrids and CMS, respectively; slopes >3 when training profiles [INEGI and ISCN] were excluded), I found that using these 250 m–resolution products to predict SOC inventories yielded greater errors (RMSE of prediction: 7.4–8.3 kg m^{-2} in leave–one–out cross–validation) than when I used 1 km–resolution water balance–related variables (MAP_{bc} or AI_{bc}) directly. Agreement between observed and predicted SOC inventories in the 0–100 cm interval was lower still (adjusted R^2: 0.13 for CMS and 0.24 for SoilGrids; RMSE of prediction: 18.7 and 17.5 kg m^{-2}, respectively). The greater prediction errors identified for the 0–100 cm CMS product, which had the greatest spatial resolution of all products evaluated in this study (90 m versus 250 m for SoilGrids and 0–30 cm CMS predictions and 1 km for GSOCmap), highlight the need for future investigation into the scale dependencies of empirical proxies for SOC storage in complex terrain (Ließ et al., 2016).

3.4.2 Bayesian calibration of SOC predictions: Lessons and future priorities

The overarching objective of this study was to develop strategies for using existing observations of SOC storage to constrain predictions for locations where observations are unavailable. Calibrating SOC predictions with Bayesian spatial random effects (SRE) models yielded spatially distributed estimates of SOC inventories with uncertainties that directly represented the level of variability observed within the study area. In some parts of the landscape, extreme prediction uncertainties were likely driven more by the lack of nearby observations (Fig. 3.9) than by true pedologic variation. In such areas of low data density, simple linear calibrations (i.e., (3.4)) may be warranted. However, calibrated values will be unrealistically precise if the uncertainty of calibration parameters and the spatial structure of residual errors are disregarded. I found that estimating the parameters of the spatially varying coefficient model (3.5) using only the small number of local observations available in national and global databases (INEGI and ISCN; n=28) resulted in an effectively linear calibration (Fig. 3.5) and still providing an informed perspective of the plausible range of SOC inventories at any particular point on the landscape. Hence, with minor use–specific modifications (e.g., prior specifications, number of spatial random effects), this approach may be fruitful even when data from independent studies are not available. However, if existing data require estimation of bulk density, I stress that associated uncertainty should be propagated through subsequent calculations and calibrations (Guevara et al., 2020).

Ultimately, my results underscore that improving confidence in predictions of SOC inventories at new locations within landscapes—and estimates of total SOC storage at the landscape level—hinges on reducing profile–level uncertainties and ensuring that observations adequately span the full range of environmental conditions ("feature space") present at a particular spatial scale. While not a solution to either of these problems, Bayesian methods give quantitative benchmarks of our progress towards meeting them. As an illustration, Figure 3.12 depicts potential SOC inventories (0–30 cm) in four soils under different land uses at varying distances (0.2–5.7 km) from the nearest profile included in this study. Off–the–shelf (uncalibrated) model predictions for the pixels containing these sites are overlaid on predictions from the SRE model with coregionalization (green distributions) and SOC inventories calculated with measured carbon concentration data (Romero Uribe, 2017) and PTF–estimated bulk density (blue distributions). The blue distributions are the best estimates for SOC inventories at these locations given the available (site–specific) carbon concentration data, whereas the green distributions simultaneously integrate information from SoilGrids, CMS, and nearby observations. Uncalibrated

models systematically underestimated SOC inventories for pasture and forest sites, though the PTF–estimated SOC distribution for the forest was full contained within the 90% prediction interval of SoilGrids. In contrast, uncalibrated model predictions more closely approximated SOC estimates for the sugarcane and coffee soils. SRE predictions were highly uncertain in all cases, but median predictions varied more realistically across the four locations than did the uncalibrated predictions.

One promising possible way to reduce both profile–level uncertainties (narrow the blue distributions) and the uncertainties of spatial predictions (narrow the green distributions) is to extend the coregionalization approach to accommodate additional information sources. In this study, I used coregionalization to jointly predict SOC inventories in two intervals, leveraging observations for the 0–30 cm interval when available to reduce the uncertainty of predictions for the 30–100 cm interval. In a similar way, SOC inventories can be jointly predicted with other (non–SOC) variables. For instance, my finding that Fe_o (a semiquantitative indicator of poorly crystalline iron abundance) was the single strongest predictor of SOC inventories after precipitation may be exploited by developing models that jointly predict SOC and Fe_o (or a more scalable proxy for poorly crystalline phases, e.g., far–infrared spectral absorbance; Parikh et al., 2014). After training a coregionalization model with paired observations of both SOC and the chosen mineralogical proxy, prediction uncertainties for SOC at new locations can be reduced by measuring the proxy alone. Previous researchers have employed Bayesian coregionalization to predict soil elemental concentrations (Majumdar et al., 2008), and empirical evidence for the association between metastable (organo)mineral phases and SOC storage is growing steadily (Heckman et al., 2020; von Fromm et al., 2020). The integration of these two areas of research may offer significant improvements in confidence in SOC predictions in complex landscapes.

3.5 Tables

		$\rho_{b,o}$			$\rho_{b,m}$			σ^2		
Dataset	n	50%	2.5%	97.5%	50%	2.5%	97.5%	50%	2.5%	97.5%
1	435	0.226	0.196	0.264	1.052	1.003	1.105	0.116	0.101	0.133
2	472	0.221	0.193	0.254	1.032	0.989	1.082	0.116	0.103	0.132
3	629	0.208	0.189	0.232	1.046	1.005	1.085	0.094	0.085	0.105
4	306	0.187	0.174	0.200	0.978	0.941	1.019	0.039	0.034	0.046
5	421	0.130	0.119	0.140	0.909	0.857	0.966	0.101	0.088	0.116
6	129	0.147	0.134	0.162	1.131	0.996	1.303	0.058	0.046	0.075
7	275	0.100	0.091	0.110	0.938	0.884	1.001	0.094	0.080	0.112

Table 3.1: Estimates (medians) and uncertainties (2.5% and 97.5% quantiles) of the parameters of the bulk density pedotransfer function of Adams (1973) for soils in the study area and soils formed in volcanic parent materials globally. Datasets: 1. All Andosols in WoSIS (Batjes et al., 2019). 2. Dataset 1 plus all other study area soils in WoSIS. 3. Dataset 2 plus all soils formed in volcanic parent materials in ISRaD (Lawrence et al., 2019). 4. Soils formed in volcanic parent materials across climatic and weathering gradients from a global survey (García-Rodeja et al., 2004; Dümig et al., 2008; Tsai et al., 2010; Peña-Ramírez et al., 2015). 5. All original and published data compiled for the study area (including samples without reported depths). 6. Observations in Dataset 5 from depths <30 cm. 7. Observations in Dataset 5 from depths >30 cm. $\rho_{b,o}$ and $\rho_{b,m}$ are interpreted as the bulk densities of the pure organic and mineral fractions, respectively, and σ^2 is the residual variance.

Source	ρ_b	SOC inventory, 0–30 cm				SOC inventory, 0–100 cm			
		n	50%	Min	Max	n	50%	Min	Max
Gavilanes (D. Geissert)	Measured	40	17.4	8.8	44.5	32	41.7	14.8	78.0
Gavilanes (D. Geissert)	PTF	2	16.5	7.5	25.4	1	65.5		
Pixquiac	Measured	16	15.4	9.0	21.7	13	28.6	15.1	42.6
Aguilar Orea (2013)	Measured	8	24.1	14.2	46.3	1	75.2		
Gamboa & Galicia (2012)	Measured	15	12.5	1.7	19.5	9	21.2	2.7	41.6
Geissert et al. (1994)	Measured	5	8.1	3.5	11.3	3	14.0	6.1	14.4
Geissert et al. (1994)	PTF	11	10.1	1.1	39.2	9	34.7	4.3	64.7
INEGI (2004)	PTF	5	3.7	0.2	12.5	3	4.8	0.6	32.8
INEGI (2013a)	PTF	9	4.7	1.5	18.4	7	33.6	4.2	50.4
Zinke et al. (1986)	Measured	11	9.4	2.3	17.2	8	17.4	5.0	49.7
Zinke et al. (1986)	PTF	3	9.4	7.7	10.1	2	18.6	13.2	24.1
Meza Pérez (1996)	Measured	6	13.3	5.2	39.0	4	19.3	11.3	28.2
Meza Pérez (1996)	PTF	3	15.6	12.9	25.9	3	46.8	28.8	122.5
Muñoz-Villers et al. (2020)	PTF	1	3.2			1	5.1		

Table 3.2: Median and range of soil organic carbon inventories (kg m^{-2}) in 0–30 cm and 0–100 cm depth intervals, calculated with original and previously published data. Data of Zinke et al. (1986) were accessed through the ISCN database (Nave et al., 2016). Profiles for which one or more bulk density values were estimated using the pedotransfer function (PTF) of Adams (1973) are listed separately from those with measurements available for all horizons. PTF parameter estimates obtained with data from global databases (Dataset 3 in Table 3.1 were used for INEGI (2004, 2013a); Zinke et al. (1986); local (dataset 5) parameters were used in all other cases. The median of the posterior distribution of the SOC inventory for PTF profiles was taken for this summary (i.e., propagated uncertainty not shown). n = number of profiles.

Model	Variable	Factor 1	Factor 2
Spatial covariates, SOC in 0-30 cm	CMS100	0.52	0.86
	AI_{bc}	-1	0
Spatial covariates, SOC in 0-30 and 30-100 cm	$SOC_{0–30}$	0.57	0.16
	MAT	-0.14	0.99
	MAP_{bc}	-1	0
Spatial + site–specific covariates, SOC in 0-30 cm	$SOC_{0–30}$	-0.55	-0.20
	$SOC_{30–100}$	-0.57	-0.08
	$Fe_{o,\ 0–30}$	0.32	0.96
	AI_{bc}	-1	0
Spatial + site–specific covariates, SOC in 0-30 and 30-100 cm	$SOC_{0–30}$	0.57	0.41
	MAP_{bc}	-1	0
	$Fe_{o,\ 0–30}$	-0.26	-0.97
	$SOC_{0–30}$	-0.55	-0.44
	$SOC_{30–100}$	-0.57	-0.28

Table 3.3: Correlations between sparse partial least square (sPLS) factors and covariates selected via lasso penalization in model fitting. Correlations are also provided for the regression response variables, SOC inventories in the 0–30 and 30–100 cm intervals ($SOC_{0–30}$ and $SOC_{30–100}$, respectively). Only a single covariate was chosen to load on each factor; hence, a correlation of $\pm$ indicates that a latent factor and a covariate are identical (first factor of each model). The second factor can be interpreted as explaining variation in $SOC_{0–30}$ and/or $SOC_{30–100}$ that remains after accounting for the effect of the first factor. CMS100: CMS–predicted SOC inventory for 0–100 cm interval (90–m resolution); MAP_{bc}: mean annual precipitation from CHELSA v1.2 (Karger et al., 2017) corrected for observational bias (Beck et al., 2020) (1–km resolution); AI_{bc}: ratio of CHELSA mean annual potential evapotranspiration to MAP_{bc}; MAT: mean annual temperature from WorldClim v2.1 (Fick & Hijmans, 2017); $Fe_{o,\ 0–30}$: inventory of oxalate–extractable iron in the 0–30 cm interval. Only a single covariate was chosen to load on each factor; hence, a correlation of $\pm$ indicates that a latent factor and a covariate are identical.

3.6 Figures

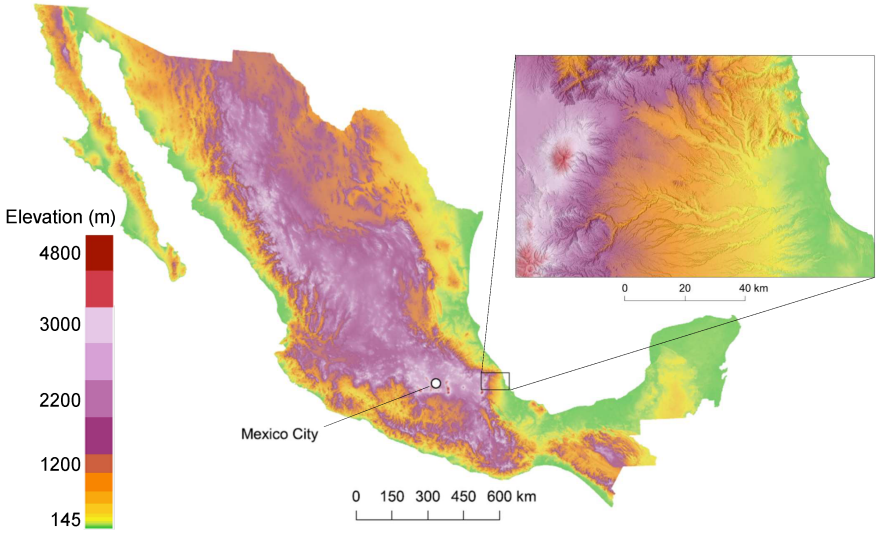

Figure 3.1: Study area in east–central Mexico. Elevation data obtained from INEGI (2013b).

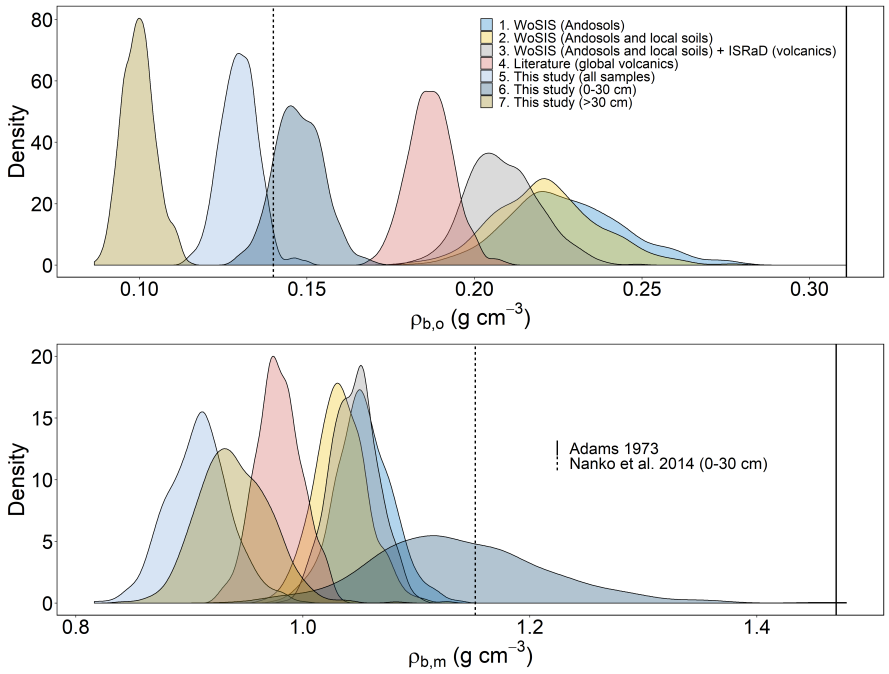

Figure 3.2: Distributions of parameter estimates for the bulk density pedotransfer function of Adams (1973) (500 thinned MCMC samples each). $\rho_{b,o}$ and $\rho_{b,m}$ are interpreted as the bulk densities of the pure organic and mineral fractions, respectively. Dashed lines indicate least-square parameter estimates from an analysis of Andosols throughout Japan (Nanko et al., 2014). Solid lines indicate values from Adams (1973), originally estimated for Podzols formed in mudstone in a temperate climate.

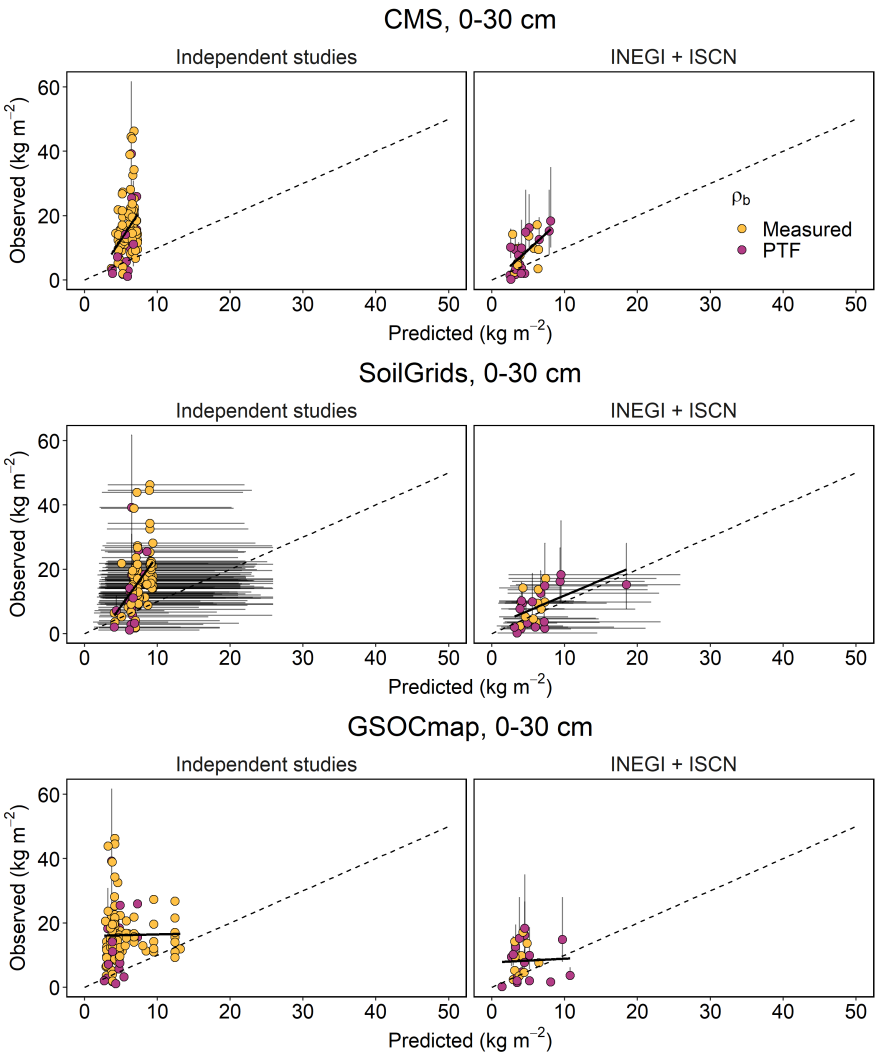

Figure 3.3: Predictions of SOC inventories in the upper 30 cm from preexisting models versus observed values. Profiles in the INEGI and ISCN databases (right panels) were involved in the development of models. Vertical error bars indicate propagated uncertainty from the estimation of bulk density where missing. Horizontal error bars in SoilGrids panels give 5% and 95% quantile predictions generated with quantile random forests. CMS uncertainties not shown as they were distributed as a single prediction interval width rather than upper and lower bounds.

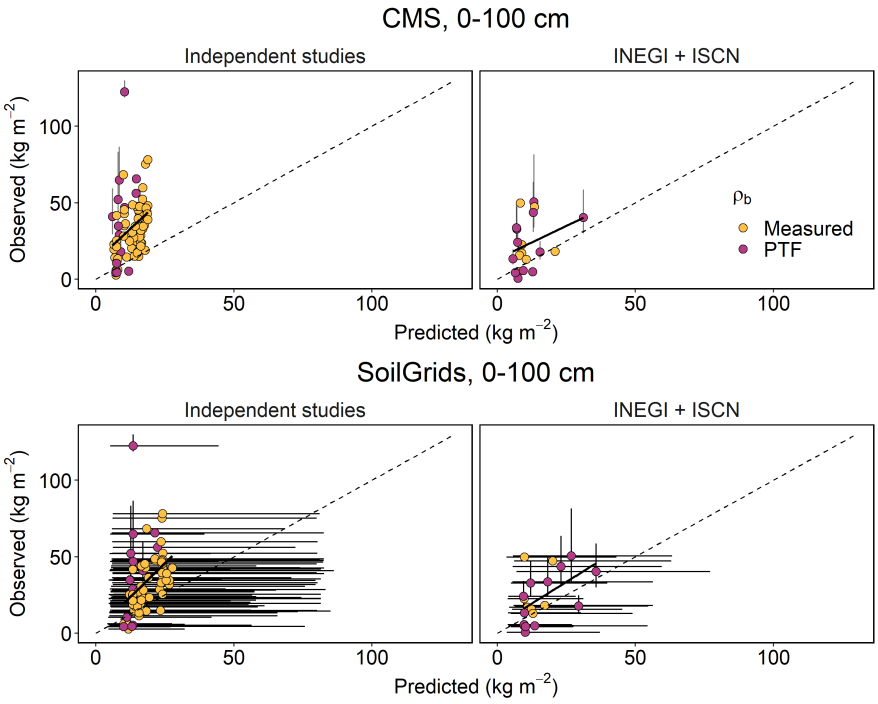

Figure 3.4: Predictions of SOC inventories in the upper 100 cm from preexisting models versus observed values. Profiles in the INEGI and ISCN databases (right panels) were involved in the development of models. Vertical error bars indicate propagated uncertainty from the estimation of bulk density where missing. Horizontal error bars in SoilGrids panels give 5% and 95% quantile predictions generated with quantile random forests. CMS uncertainties not shown as they were distributed as root–mean–square error.

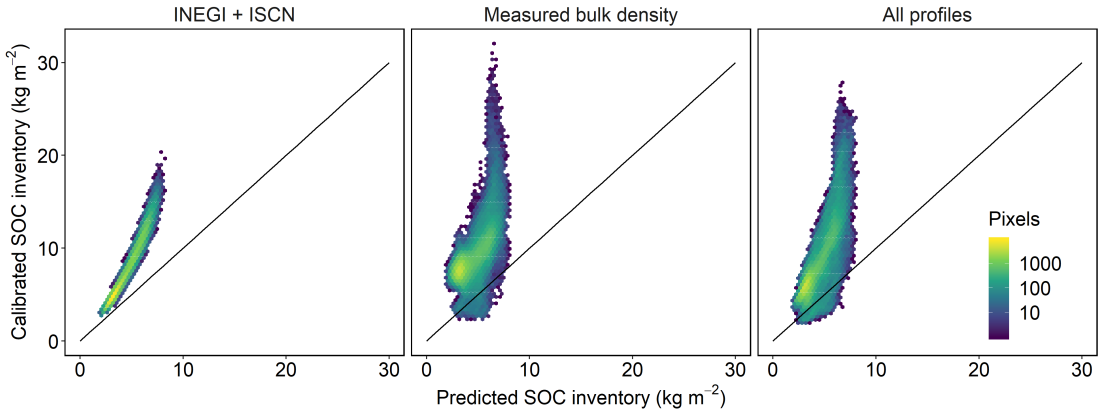

Figure 3.5: Macroscopic effects of calibrating SOC predictions with a spatially varying coefficient model. CMS predictions for the 0–30 cm interval were calibrated by fitting the spatially varying coefficient model (3.5) to different subsets of data. Left: calibration model fit with 28 profiles in the databases originally used to develop the model. Center: model fit with 101 profiles with complete sets of bulk density values (no use of PTFs). Right: model fit with all 135 profiles. In all plots, points are binned medians of pixel–level posterior predictive distributions. Pixels refer to the 250–m grid cells of the CMS product used as a covariate in the model.

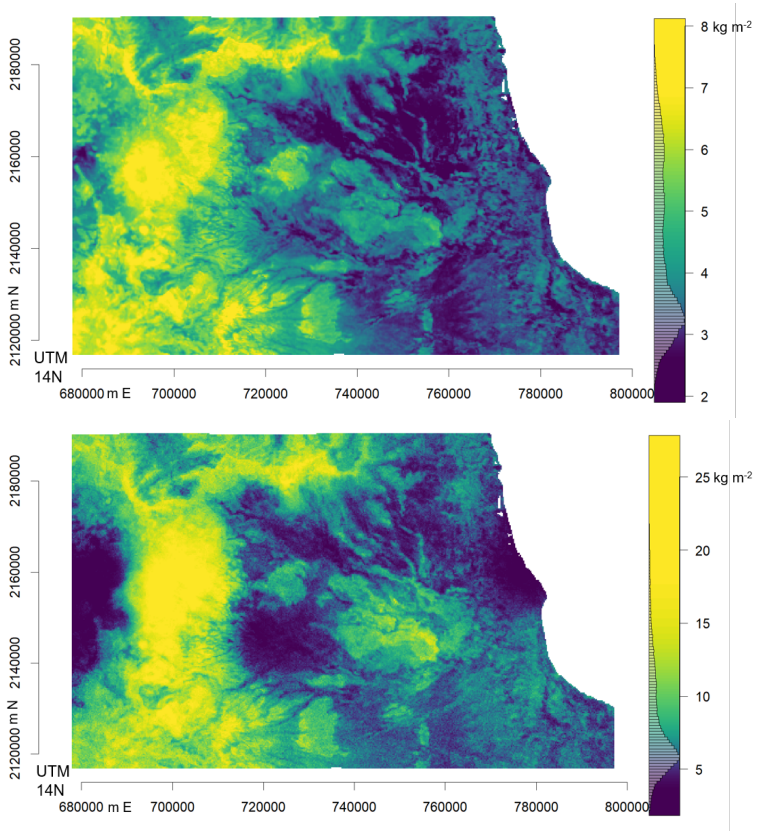

Figure 3.6: Predicted (top) and calibrated (bottom) SOC inventories (kg m^{-2}) for the 0–30 cm interval. Calibration spatially varying coefficient model fit with the full set of 135 profiles. Median calibrated predictions shown. Note differences in color scale. Map projection: WGS 84 / UTM zone 14N.

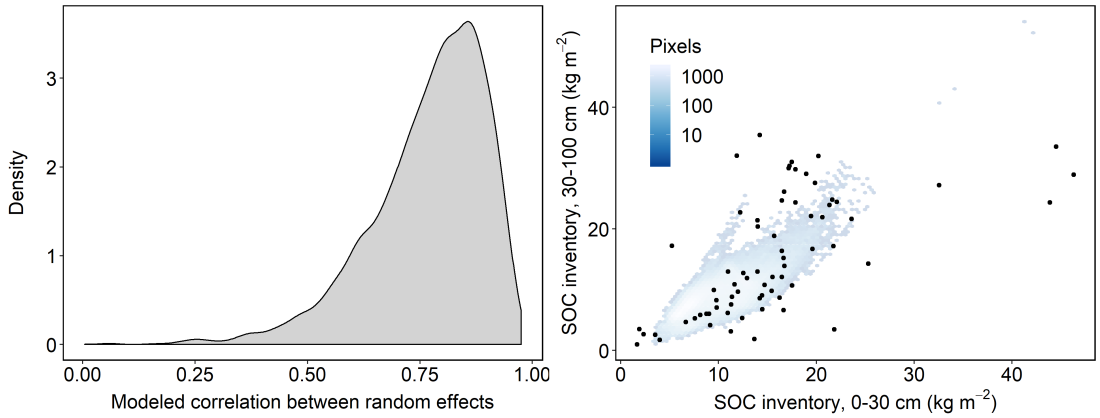

Figure 3.7: Correlation between SOC inventories in the 0–30 and 30–100 cm depth intervals. Left: the posterior predictive distribution (PPD) of the correlation between the random effects in the coregionalization model (3.6). The correlation was derived from the cross–covariance parameter, **A**, in the model fit to the profiles with complete bulk density data (101 profiles total, 70 profiles with data to 100 cm). Right: relationship between SOC inventories in the upper and lower depth intervals. Faint points are SOC inventories jointly predicted with the coregionalization model, integrating the effects of the modeled correlation (left panel) as well as all other estimated parameters. PPD medians binned for visualization. Dark points are observed inventories for the profiles used in fitting the model. Pixels refer to the 250–m grid cells of SoilGrids and CMS products used as covariates in the model.

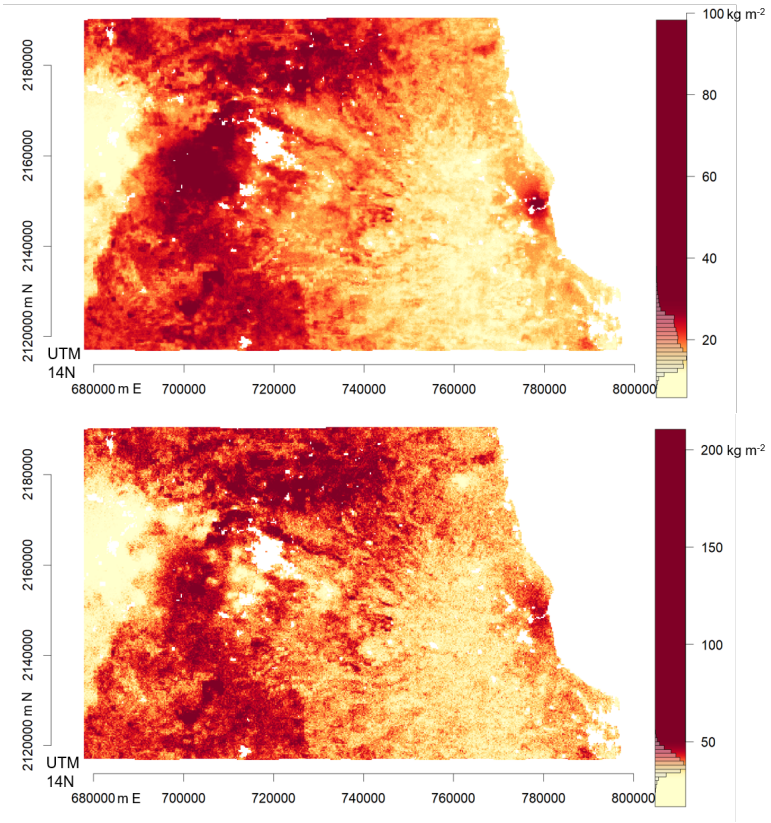

Figure 3.8: Predicted SOC inventories (kg m^{-2}) for the 0–100 cm interval (top) with uncertainties (95% credible interval widths, bottom). Predictions were obtained by summing coregionalized predictions of SOC inventories in the 0–30 and 30–100 cm intervals. Predictions for the 0–30 cm interval from SoilGrids and CMS were used as covariates in the model, in addition to an additive spatial random effect. Areas without predictions indicate features masked in SoilGrids (i.e., urban areas, rock, and water bodies). Map projection: WGS 84 / UTM zone 14N.

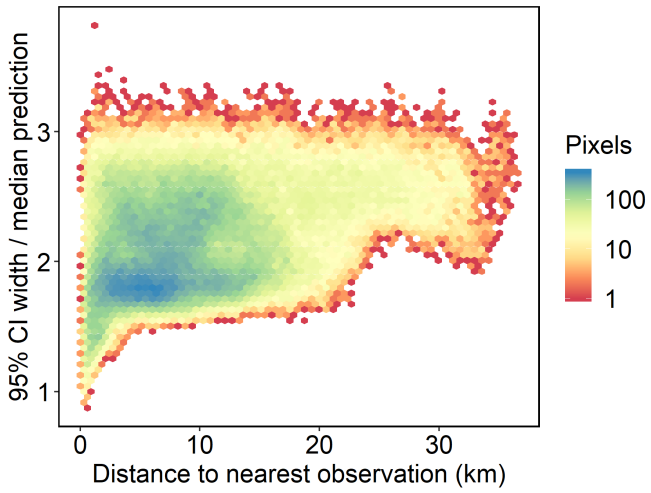

Figure 3.9: Relative uncertainty of predicted SOC inventories (sum of 0–30 and 30–100 cm depth intervals) in relation to proximity to existing observations. Pixels refer to the 250–m grid cells of SoilGrids and CMS products used as covariates in the model.

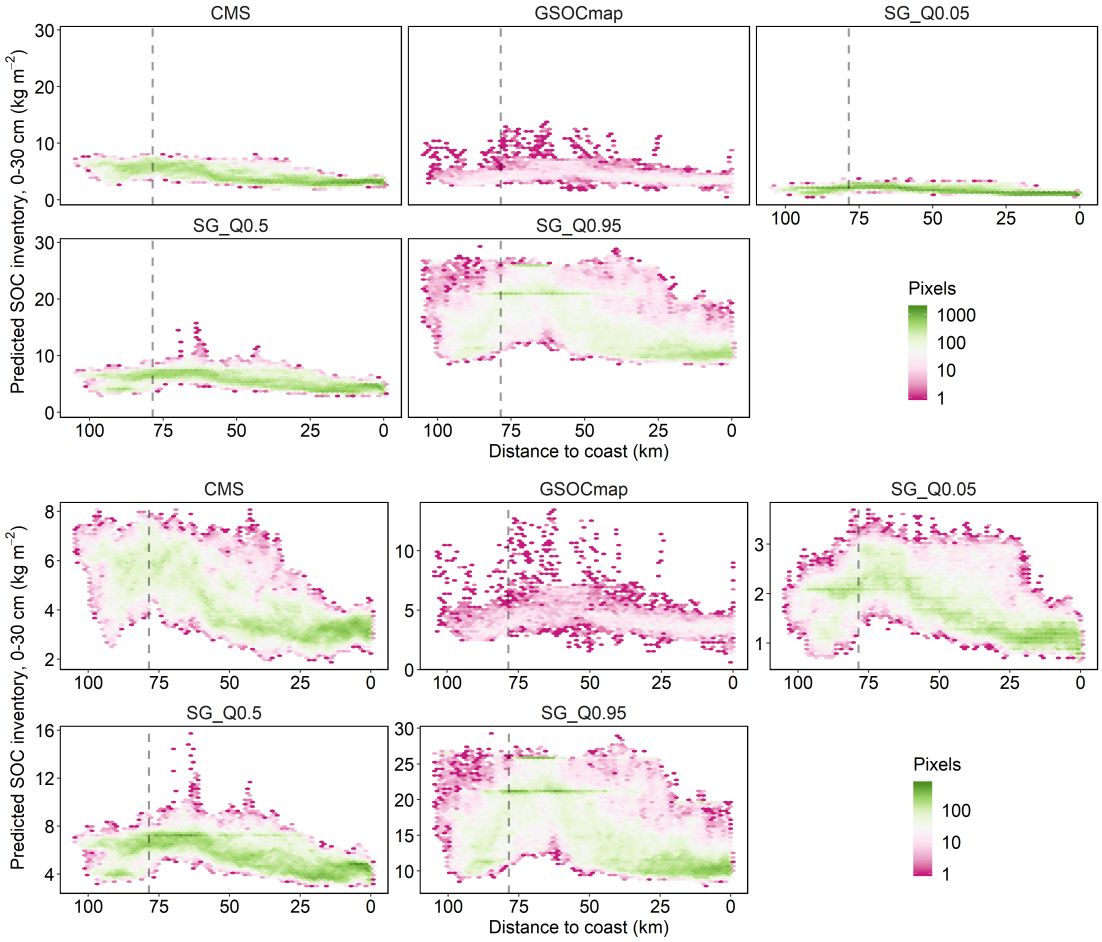

Figure 3.10: Absolute (top) and relative (bottom) trends in upper soil soil organic inventories (0–30 cm) along the longitudinal transect from the altiplano to the Gulf of Mexico, as predicted by different regional–to–global models. SG_Q0.05, SG_Q0.5, and SG_Q0.95 indicate median, 5%, and 95% prediction quantiles from SoilGrids. Dashed line shows the position of the Cofre de Perote volcano summit along the transect; areas to the left (west) of the line are in a rainshadow. Note that fewer pixels are present for GSOCmap due to its coarser resolution (1 km versus 250 m for the other products shown here).

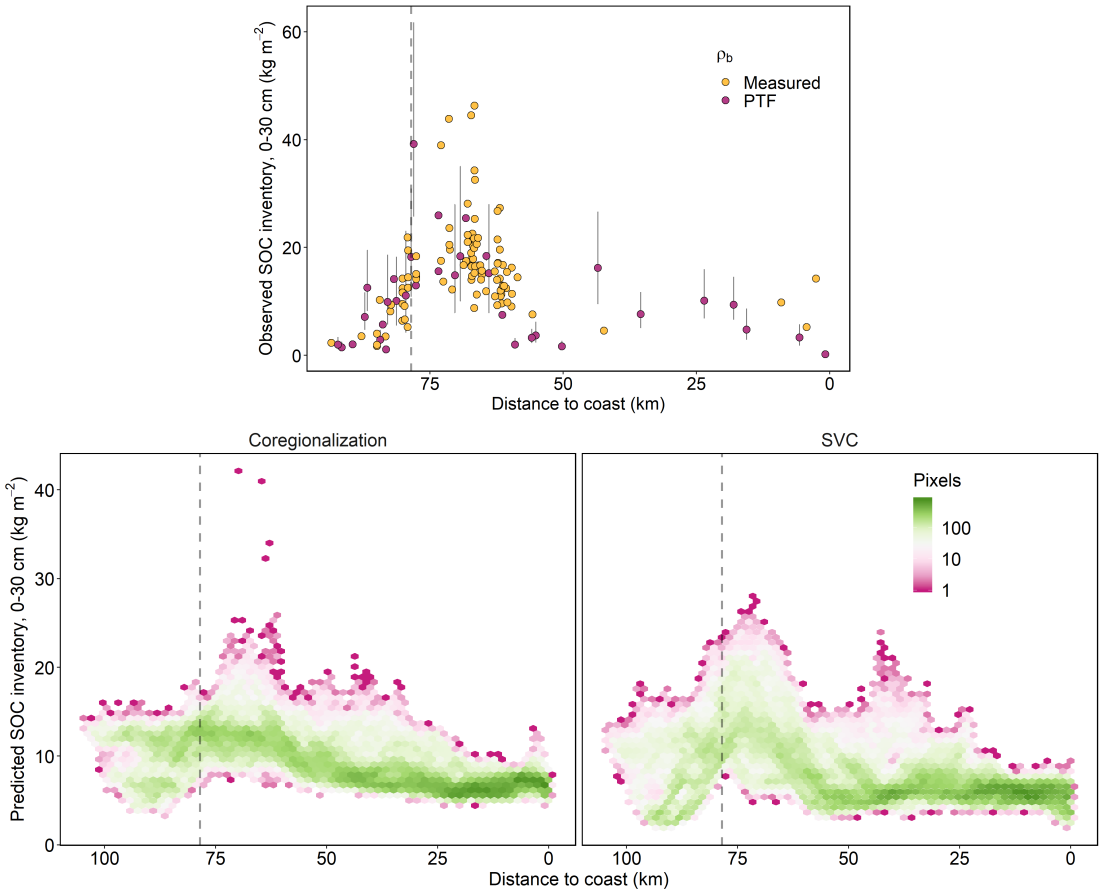

Figure 3.11: Trends in observed (top) and calibrated) SOC inventories (0–30 cm depth interval) along the longitudinal transect. Error bars in top panel indicate uncertainty (95% credible interval widths) of SOC inventories with PTF–estimated bulk density. Bottom left: predictions from a coregionalization model fit to the 101 profiles with measured bulk density, including predictions from both SoilGrids and CMS as covariates and a spatially varying intercept. Bottom right: predictions of the CMS product calibrated using a spatially varying coefficient model fit to all 135 profiles (median SOC values used where bulk density was estimated with a pedotransfer function). Medians of predictive posterior distributions were binned for visualization (i.e., prediction uncertainty not shown). Dashed line shows the position of the Cofre de Perote volcano summit along the transect; areas to the left (west) of the line are in a rainshadow.

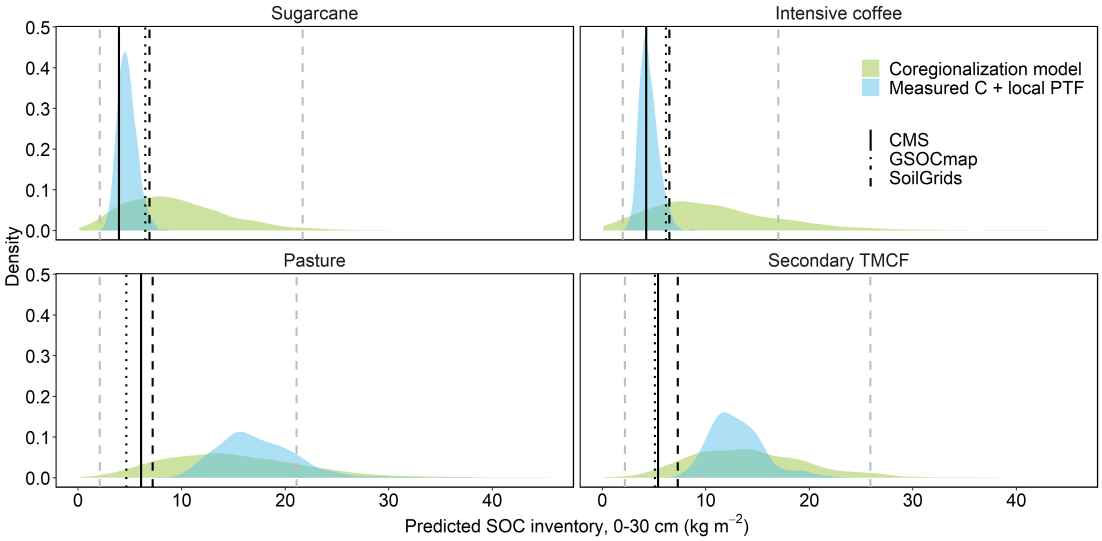

Figure 3.12: SOC inventories in the 0–30 cm depth interval predicted for independent locations in the study area. Blue distributions indicate inventories calculated with measured carbon concentration values (0–5, 5–15, and 15–30 cm intervals; Romero Uribe, 2017) and bulk density estimated using the pedotransfer function of Adams (1973) with landscape–specific parameters (Dataset 5 in Table 3.1). Vertical lines are predictions from existing SOC products; 5% and 95% quantiles of SoilGrids predictions are in gray. Green distributions are posterior predictive distributions from the coregionalization model ((3.6); jointly predicted inventories for 30–100 cm interval not shown). Clockwise from upper left, sites are 0.5, 5.7, 2.6, and 0.2 km from the nearest observation included in my analyses. Note that the sugarcane and coffee sites are at lower elevations (< 1200 m) than the pasture and tropical montane cloud forest (TMCF) sites.

Chapter 4

Land-use effects on soil organic carbon dynamics: Accounting for soil volume change in heterogeneous soilscapes

Abstract

Land-use change (LUC) modifies the size and temporal stability of soil organic carbon (SOC) reservoirs by altering the rates at which carbon enters and leaves the soil system. Changes in soil volume (i.e., strain) can occur with LUC independently of organic matter additions and losses, introducing potentially major errors into the estimation of SOC inventories. The implementation of proposed approaches to correct for strain effects on SOC storage remains limited, and the consequences of strain for proxies of SOC cycling rates (e.g., radiocarbon) are virtually unknown. Existing approaches typically assume that the soils to be compared (e.g., across experimental treatments or land uses) have undergone zero change in mineral mass. To quantify SOC dynamics in pedologic settings where that assumption is unrealistic (e.g., in intense chemical weathering environments and/or in soils dominated by metastable (organo)mineral phases), I developed an alternative method informed by the geochemical mass balance framework, assuming the immobility of a single geogenic element (e.g., zirconium or titanium). I compared conventional and immobile-element methods in order to disentangle true changes in SOC storage and turnover (inferred from radiocarbon activity) from strain effects in 16 soil profiles (0–100

cm) spanning gradients of LUC, climate, and mineral weathering in Veracruz, Mexico. Given estimated median volume reductions of 22–26% in the upper 25 cm of soil in the conversion of forest to pasture, fixed-depth calculations (ignoring strain) systematically overestimated SOC stocks under pasture and early successional stages by 21–138%, such that SOC stocks appeared to decrease during succession; this trend was reversed by adjusting for strain. Fixed–depth calculations led to negative biases in mean SOC–weighted $\Delta^{14}C$, but my finding of relatively older carbon in pastures and early successional stage did not significantly change after accounting for strain. Intercomparison of the strain–adjustment approaches strengthens the case for broader adoption of the equivalent mineral mass approach in the analysis of existing data and in future studies when geochemical data are unavailable. Realistic strain adjustments require grouping soils by development status, which itself may be guided by mass-volume relationships, as illustrated by an independent set of 42 profiles from the same landscape.

4.1 Introduction

Understanding the dynamic response of soil organic carbon (SOC) to land-use change (LUC) is critical both to improving predictions of land-atmosphere carbon exchange (Stocker et al., 2014) and to assessing the efficacy of enhancing carbon sequestration in soils (Minasny et al., 2017). How a particular land-use change (LUC)—herein defined to include discrete shifts in land-use/cover type (e.g., forest to pasture) as well as continuous changes (e.g., forest succession or land-use intensification)—affects the amount of carbon stored in soils and the duration of that storage can be highly context dependent (Don et al., 2011; Deng et al., 2016; Veldkamp et al., 2020). The complexity of the effects of LUC on SOC is of little surprise, given the multiple physical, chemical, and biological processes that mediate the relationship between LUC and SOC (Hoyos & Comerford, 2005; Marín-Spiotta et al., 2008; Paul et al., 2008).

The size of SOC stocks is determined by the balance of input rates of plant-derived carbon (i.e., in leaf litter, aboveground woody debris, roots, and root exudates) and rates of loss through heterotrophic decomposition, fire, leaching, herbivory, and erosion (Chapin et al., 2006; Stewart et al., 2007; Doetterl et al., 2016). Thus, the response of SOC stocks to LUC represents the net outcome of changes in vegetation structure, productivity, and biomass allocation, microbial activity, and the myriad processes governing the other (non-respiratory) loss pathways. The persistence of SOC (i.e., distributions of residence time, age, etc.) depends on this same set of

rates, of course, but also reflects their respective heterogeneities (e.g., distinct decomposition rates for particulate and mineral-associated organic matter) and interactions (e.g., "priming" of microbes by plant inputs) (Sierra & Müller, 2015).

Compounding the inherent challenges of measuring these phenomena, LUC can lead to major sampling errors due to soil volume change, or strain ϵ, which encompasses both collapse ($-1 \leq \epsilon < 0$) and dilation ($\epsilon > 0$). Strain can occur with changes in SOC because organic matter typically occupies volume in excess of preexisting pore space (Adams, 1973), but strain may also take place with no net mass flux via changes in soil porosity (Sollins & Gregg, 2017). In some research contexts, the direct mechanistic effects of strain on SOC dynamics may be of primary interest, as when, for example, compaction (i.e., collapse) from past LUC restricts root growth or reroutes leaching fluxes from deeper to shallower subsurface flowpaths. More often, however, researchers seek to quantify changes in the mass of SOC per unit area (i.e., stocks or inventories) over a predefined depth interval (e.g., from the ground surface to 30 cm). In these cases, sampling soils subject to LUC or to different management conditions to a fixed depth may confound strain effects with true changes in SOC mass. Ignoring strain can impart significant bias to point estimates (e.g., inventories) and lead to qualitatively different conclusions (e.g., rates of SOC change or pairwise differences between land-use types; Ellert & Bettany, 1995; Crow et al., 2016).

When soils that have experienced different degrees of strain are sampled to a fixed depth, those samples will differ both in the initial (pre-strain) depth intervals represented and (usually) in the mass of mineral material included. Previous studies have largely focused on the latter issue because variation in the sampled mass contributes directly to variation in calculated stocks, even if SOC storage remains constant (Lee et al., 2009). Several strategies have been proposed to correct for this bias at the time of sampling (Gifford & Roderick, 2003; Wendt & Hauser, 2013) or at the calculation stage (Ellert & Bettany, 1995; Rovira et al., 2015; see Sollins & Gregg, 2017 and von Haden et al., 2020 for recent overviews). While the details of these methods differ, all seek to rescale the amount of soil analyzed such that the mass and volume of soils would have been equivalent prior to strain. SOC stocks calculated on a fixed-depth basis versus using one of these strain–adjustment methods (e.g., the "equivalent soil mass"[ESM] approach of Ellert & Bettany, 1995) for the same sample can differ by a factor similar to or greater than the effects of LUC or management. Nonetheless, ignoring strain remains far more common than adjusting for it.

The problem of sampling different initial volumes has received less attention than the sampling of different masses (Davidson & Ackerman, 1993; Murty et al., 2002), but it implies that strain may bias inference on any soil property that varies systematically with depth, whether or not that property is a direct function of soil mass. In this sense, I extend the recent assertion of von Haden et al. (2020) that strain adjustments should be evaluated for a wider range of variables other than SOC (e.g., elemental and isotopic ratios).

Consider, for example, the radiocarbon activity of two samples extracted over a fixed-depth interval from a soil before and after compaction (Fig. 4.1). The post-compaction sample includes material from a greater pre-compaction depth. If mean residence times increase with depth in this hypothetical profile, as is often observed, inclusion of deeper soil in the post-compaction sample would reduce the relative abundance of more recent carbon, which could be interpreted as the loss of faster-cycling SOC, without any actual change in SOC. The radiocarbon value (e.g., fraction of post-1950 ^{14}C) obtained for the sample from the compacted soil is equivalent to the mean of the values for the pre-compaction depth interval and the deeper material, weighted by their respective SOC stocks. Hence, while radiocarbon-related quantities (e.g., fraction modern, $\Delta^{14}C$) themselves do not depend on soil mass, they are likely subject to as-yet overlooked errors from inconsistent sampling of pre-strain depths.

If strain–adjustment methods are to be adopted more widely, the practical consequences of their assumptions must be evaluated. Most of these approaches, by design, assume that soil mineral mass remains constant with time or across sampling locations in space-for-time studies (Sollins & Gregg, 2017). In practice, strain adjustments are sometimes based on total soil mass (Lyttle et al., 2014), implicitly assuming that this mass is dominated by the mineral fraction due to its greater abundance and mean particle density. The assumption of constant soil mineral mass may be reasonable in soils composed of minerals that are effectively resistant to weathering on the time scale of the processes in question (e.g., LUC), as is the case in the landscapes in which most of the development and evaluation of ESM and related methods has occurred (i.e., mixed-mineralogy glacial parent materials in temperate climates). Errors due to deviation from the assumption of constant total soil mass are lowest if the initial amount and net change in organic matter are both small (von Haden et al., 2020).

In this study, I developed a method for quantifying biogeochemical changes in soils that have undergone strain and for which the assumptions of existing methods may not hold. Drawing upon the concepts of geochemical mass balance (Brimhall & Dietrich, 1987), which have

most frequently been applied on centennial or millennial time scales (Chadwick et al., 1990), I demonstrated how strain can be estimated by assuming the conservation of the mass of a single element, rather than the full mineral fraction. In addition to presenting this immobile-element approach, I compared the effects of different strain adjustments on the magnitude of SOC stocks and bulk soil radiocarbon estimates and their respective changes in response to LUC in soils at different chemical weathering stages and under contrasting climatic conditions.

4.2 Materials and methods

4.2.1 Study area

Field data for this study were collected on the lower flanks (1000–3000 m) of the Cofre de Perote stratovolcano in the state of Veracruz in eastern Mexico, approximately 70 km west of the Gulf of Mexico. Surface geology within the study area consists of the basaltic-andesitic to andesitic ejecta of the Cofre de Perote (active 1.3 to 0.2 million years ago; Carrasco-Núñez et al., 2010), with localized contributions of basaltic scoria and lava from cinder cones (active as recently as 900 years ago; Siebert & Carrasco-Núñez, 2002; Rodríguez et al., 2010) and dacitic to rhyolitic material from more remote sources (Fitz Bravo, César and Ramírez Tello Enrique, 2007; Servicio Geológico Mexicano, 2007b), as well as isolated outcrops of the Cretaceous limestone basement (Negendank et al., 1985; Rossignol et al., 1992). Climate ranges from humid subtropical at lower elevations (mean annual temperature [MAT] = 19.3 °C and mean annual precipitation [MAP] = 1755 mm at 1188 m) to humid temperate at higher elevations (MAT: 9.5 °C; MAP: 1708 mm at 3102 m) (Servicio Meterológico Nacional, 2017), with maximum rainfall (MAP >3000 mm) at intermediate elevations (Muñoz-Villers et al., 2012, 2016). Rainfall is highly seasonal along the elevation gradient, with approximately 80% of MAP falling from June to September. The landscape features deeply incised river valleys separated by steep hillslopes and elongated ridgelines; overall topographic relief is more pronounced above 1600 m. The distribution of Soil types reflects altitudinal variation in the weathering status of volcanic materials, with intermediately weathered soils dominated by metal-humus complexes (nonallophanic Andisols) above 1400 m and more intensely weathered soils with increasingly crystalline mineralogy (Inceptisols, Alfisols, and Ultisols) at lower elevations; shallow rocky soils (Orthents) mantle the extremely steep slopes above 2300 m (Rossignol et al., 1992; INEGI, 2013a; Paré & Gerez, 2012). Ecosystem types along the elevation gradient include tropical dry

forest (<1200 m), lower montane cloud forest (1200-1700 m), and upper montane cloud forest (1700-2300 m), grading into mixed broadleaf-coniferous (2300-3000 m) and coniferous forests (>2900) (Toledo-Garibaldi & Williams-Linera, 2014). All forest types are subject to selective logging of varying intensity. Urban infrastructure, shade coffee agroforestry, and sugarcane have replaced the majority of the tropical dry forest and much of the lower montane cloud forest (Muñoz-Villers & López-Blanco, 2008). Smallholder row crop (traditionally maize and bean) and livestock (cattle, sheep, and goat) production occurs above 1300 m, with fields generally much less than one hectare (Paré & Gerez, 2012). While deforestation and forest fragmentation continue to take place (Williams-Linera et al., 2002; Von Thaden et al., 2019), multiple socioecological processes (e.g., emigration, conservation and restoration, multidecadal slash-and-burn management systems) have contributed to widespread secondary succession of cloud forest vegetation in former croplands and pastures.

4.2.2 Soil sampling and analyses

I sampled 16 soil profiles spanning a gradient of disturbance and succession near the present-day altitudinal limits of cloud forest vegetation (lower montane cloud forest at 1350-1550 m and upper montane cloud forest at 2050-2220 m) in the Pixquiac catchment (107.3 km^2). I constrained site selection to soils formed in volcanic ash (excluding lava and non-volcanic parent materials). However, soils ranged in physicochemical properties and mineralogy, likely driven by both climate and differences in duration of chemical weathering (e.g., substrate age and degree of rejuvenation by erosion/deposition). Hereafter, I refer to the four more-weathered profiles—all within the lower elevation band—as Inceptisols and the 12 less-weathered profiles—four in the lower elevation band, eight in the upper—as Andisols (see Table 4.1). To characterize soils under the most and least disturbed conditions within both elevation bands, I sampled one pasture under active cattle grazing and one mature forest, likely subject to selectively logging but with no evidence of clear-cutting or grazing for at least 80 years prior to sampling. To assess soil mass-volume relations at different successional stages, I also sampled six sites ranging in time since grazing (2–60 years) per elevation band. I further characterized land-use/cover changes for each site by interpreting satellite and aerial imagery from 1966 to the time of sampling (2018). This imagery-based assessment of duration of secondary succession agreed reasonably well with landowner-reported time since grazing (Spearman's rank correlation coefficient = 0.79).

Soil profiles were excavated at backslope positions on steep hillslopes (25–45°) as this is

where much of the bidirectional changes in forest cover occurs throughout the broader landscape; sampling eroding landforms also served to minimize possible over-correction for strain in depositional environments. At each sampling location, I characterized vegetation structure by measuring canopy cover (GRS densitometer), basal area (angle gauge), and mean and maximum tree height (laser rangefinder). I additionally measured local slope gradient (laser rangefinder) and aspect (compass). Soil profiles were excavated to a minimum depth of 1 m, with the exception of one pedon with fragmented andesite at 60 cm. The surface layer of each profile was carefully shielded with a drop cloth to avoid contamination with subsoil material during excavation. I measured soil compressive strength *in situ* using a pocket penetrometer (Steber et al., 2007); measurements were conducted vertically on the soil surface and horizontally along the profile face, using an adapter foot to increase measurement sensitive in poorly cohesive soils. I sampled soils by genetic horizon for wet–chemical analyses (pH in H_2O, NaF, and KCl; oxalate-extractable Al, Fe, and Si; pyrophosphate-extractable Al and Fe; citrate-dithionite-extractable Fe). For mineral horizons, bulk density of the fine-earth fraction (material passing through a 2-mm sieve) was estimated using triplicate samples collected with metal cylinders (5 cm height, 4.7 cm diameter; Blake & Kartge, 1986). In horizons thicker than 20 cm, bulk density samples were collected within lower and upper portions of the horizon. Where peat-like organic horizons were present, I estimated bulk density by extracting a sample with a soil knife, measuring the dimensions of the sample (verified against the dimensions of the resultant void), and calculating sample volume assuming a rectangular cuboid. Samples for all other analyses were extracted from the following depth intervals (in cm): 0–2, 2–4, 4–6, 6–8, 8–10, 10–15, 15–25, 25–40, 40–60, 60–80, 80–100. A depth of zero referred to the top of the uppermost material encountered below loose leaf litter (i.e., Oe/Oa or A horizons below Oi horizons).

Organic samples (Oi horizons and predominantly organic depth intervals) were initially homogenized by grinding in a clean food processor. Air-dried mineral samples were ground with a mortar and pestle after sieving (<2 mm). After oven-drying organic samples at 55 °C and mineral samples at 105 °C for 48 hours, carbon and nitrogen concentrations were quantified via dry combustion at 1050 °C (Nelson & Sommers, 1996). Given the probable absence of carbonates in these soils (e.g., lack of effervescence upon application of dilute HCl; typical soil pH 4–5), I assumed all carbon was in organic forms in my interpretations of carbon concentration and radiocarbon activity. Geochemical composition was quantified using a portable X-ray fluorescence (pXRF) analyzer (Olympus Innov-X DELTA Premium). Oven-dried and ground samples

were prepared for pXRF analysis by loading into 7-cm^3 plastic cups with perforated 2.5-μm membrane windows (SpectroMembrane Mylar, Chemplex Industries, Inc.). Measurements were conducted in two-beam "Mining-Plus" mode for 120 seconds in a benchtop stand. Duplicate readings per sample were conducted on separate days and averaged for subsequent calculations. I was primarily concerned with estimating zirconium (Zr) and titanium (Ti) concentrations to use these rock-derived elements as relatively immobile tracers (Brimhall & Dietrich, 1987) in the proposed strain adjustment method. Both Zr and Ti were above manufacturer-reported detection limits (1–3 and 7–15 ppm, respectively) for all but six organic-rich samples (five Oi and one surface depth interval sample) in which Ti could not be detected. For these samples, Ti concentrations were imputed by applying the log-ratio data augmentation algorithm to the full matrix of pXRF-detected elements using the zCompositions package (Palarea-Albaladejo & Martin-Fernandez, 2015) in the R statistical computing environment (R Core Team, 2018).

Particle size distributions were measured on air-dried depth-interval samples using a Malvern Mastersizer 3000 laser diffraction analyzer. Subsamples of approximately 0.5 g were shaken overnight in a solution of sodium hexametaphosphate and bleach to disperse aggregates and oxidize organic matter, respectively. Samples were then suspended in 500 mL distilled water, which was continuously stirred while suspension was drawn into the analyzer. After measuring the initial particle size distribution, I continued to disperse the suspension via 60-second sonications at maximum power output (calibration unavailable) and remeasure the particle size distribution. After preliminary tests, I chose to use the particle size distribution after four sequential sonications as an approximately stable level of dispersion. I found generally poor correlation between particle size distribution estimated with laser diffraction and with the pipette method in a separate set of soils sampled in the same landscape, even after optimizing the breaks between particle size classes using a genetic algorithm (R^2=0.3 for laser diffraction-predicted clay content, n = 98 soils). Furthermore, calorimetric tests with a more powerful sonication unit (Qsonica Q500) suggested that the Malvern sonicator likely did not yield sufficient energy to fully disperse silt-sized aggregates (data not shown). Hence, for the purposes of this study, I interpreted the laser diffraction results as the size distribution of both particles and sonication-resistant aggregates. For data analysis, I summarized each particle/aggregate size distribution by summing the volumetric fraction within particle diameter bins defined by orders of magnitude (i.e., <1, 1–10, 10–100, and 100-1000 μm) and used ratios between these bins as proxies for the relative abundance of particles and aggregates in broadly defined size ranges (e.g., ratio

of silt and silt-sized aggregates to clay and clay-sized aggregates).

Radiocarbon activity was measured on Oi horizons and the uppermost eight depth–interval samples (0–40 cm) from each profile at Lawrence Livermore National Laboratory. Following Vogel et al. (1987), I combusted ball-milled soils with CuO and Ag in evacuated quartz tubes and reduced the resulting CO_2 to graphite in the presence of H_2 gas and a powdered Fe catalyst. The abundance of radiocarbon (^{14}C) atoms in graphitized samples was analyzed via accelerator mass spectrometry. Results were corrected for mass-dependent fractionation (assuming a $\delta^{13}C$ value of -25‰ based on preliminary EA-IRMS analysis of my samples) and expressed as $\Delta^{14}C$ relative to the OX1 standard (Stuiver & Polach, 1977). Positive $\Delta^{14}C$ values in bulk soil samples reflect the relative abundance of faster-cycling ("modern") carbon, whereas negative $\Delta^{14}C$ values indicate that a greater fraction of SOC is exchanging with the atmosphere on much longer time scales.

To contextualize the mass–volume relationships analyzed in the 16 profiles within the broader landscape, I also drew upon unpublished soil physicochemical data for 42 profiles sampled in the adjacent Gavilanes catchment (41.3 km^2). The locations of these profiles were selected to represent the primary combinations of landforms (hydropedologic units) and land-cover types across the full elevation gradient (1000 to 3000 m) (see Geissert2013 for a detailed description of the sampling design). Soil bulk density, wet-chemical properties, and carbon and nitrogen concentrations were analyzed on horizon-based samples using the same methods as for the 16 profiles in this study. Additionally, soil particle density was measured using air pycnometry for this set of profiles (Flint & Flint, 2002).

4.2.3 SOC metrics and strain adjustments

In this section, I outline the steps involved in calculating the depth-dependent accumulation of mass (units of mass per area) and mass-weighted means (dimensionless or arbitrary units). I then describe how these calculations are applied to obtain conventional (fixed–depth) and strain–adjusted estimates of SOC inventories and mean $\Delta^{14}C$.

4.2.3.1 Calculations

The stock of total soil mass in layer *i* (e.g., a fixed-depth sampling interval) is calculated as

$$S_{s,i} = \rho_{b,i} \Delta z_i 10, \tag{4.1}$$

where $\rho_{b,i}$ is the oven-dry bulk density in layer *i* (g cm^{-3}), Δz_i is the thickness of layer *i* (cm), and the factor of 10 is a unit conversion, giving the stock $S_{s,i}$ (kg m^{-2}).

The stock of soil component *x* (e.g., mineral mass, SOC, Zr, Ti) is obtained simply as

$$S_{\mathrm{x,\,i}} = S_{s,i} c_{x,i}, \tag{4.2}$$

with $c_{\mathrm{x,\,i}}$ being the mass fraction of *x* in layer *i* (g g^{-1}).

The cumulative mass inventories of soil and of soil component *x* (I_s and I_x, respectively) at the bottom of the nth layer are then determined by summation:

$$I_s = \sum_{i=1}^{n} S_{s,i} \tag{4.3}$$

$$I_x = \sum_{i=1}^{n} S_{x,i}. \tag{4.4}$$

Applying (4.3) or (4.4) consecutively to each soil layer yields *n* pairs of depth and cumulative mass (I_s or I_x). Approximation of these calculated depth–mass pairs as continuous accumulation curves using monotonic cubic splines (Wendt & Hauser, 2013; von Haden et al., 2020) allows the interpolation of I_s and I_x to any intermediate depth *z*.

To summarize a mass-normalized variable g (e.g., concentration or ratio of elements or isotopes) across *n* soil layers, a common approach is the mass-weighted mean:

$$\bar{g}_s = \frac{\sum_{i=1}^{n} S_{s,i} g_i}{I_{s,n}} \tag{4.5}$$

$$\bar{g}_x = \frac{\sum_{i=1}^{n} S_{x,i} g_i}{I_{x,n}}, \tag{4.6}$$

where the subscripts *s* and *x* indicate weighting by soil mass or by the mass of a soil component (e.g., SOC), respectively. The value of the mass-weighted mean at any depth *z* can be

estimated as described for cumulative inventories, but without the monotonic constraint on interpolation. For the purposes of this study, $\bar{g}_s$ or $\bar{g}_x$ can be interpreted as an estimate of g for a single sample extracted from the soil surface to depth z (e.g., a soil core sample).

Finally, I seek to estimate the cumulative inventory I_y of non-conservative material y (e.g., SOC) and the mean $\bar{g}_y$ of variable g weighted by the mass of material y (e.g., Δ^{14}C weighted by SOC) at nominal depth z_{nom} in a profile that has undergone strain. To do so, I first select a material x (e.g., bulk soil mass, soil mineral mass, or an immobile element such as Ti or Zr) for which I assume zero net mass change over the relevant time scale. Next, I identify the depth $_{ExM}$ (i.e,. "depth of equivalent x mass") at which I_x (i.e., the cumulative inventory of x) is equal to $I_{x,z_{nom},ref}$, the value of I_x at z_{nom} in a reference profile for which strain is assumed zero. Defining strain ϵ as the change in volume in another profile (with current volume V_{str}) relative to the reference profile (volume V_{ref})—

$$\epsilon = \frac{V_{str}}{V_{ref}} - 1. \tag{4.7}$$

—and assuming a constant cross-sectional area, I can calculate strain in the non-reference profile as

$$\epsilon_z = \frac{z_{ExM}}{z_{nom}} - 1. \tag{4.8}$$

The strain–adjusted values of the variables of interest (I_y or $\bar{g}_y$) are obtained from the pairs of depth and I_y or depth and $\bar{g}_y$ by interpolating to z_{ExM}. Equivalent results can be interpolated directly from the pairs of I_x and I_y or I_x and $\bar{g}_y$ (i.e., without reference to depth; Rovira et al., 2015), as long as $I_{x,z_{nom},ref}$ has been determined. Additionally, ϵ can be estimated by comparing cumulative mass inventories at z_{nom} rather than depths as in (4.8):

$$\hat{\epsilon}_{I_x} = \frac{I_{x,z_{nom},ref}}{I_{x,z_{nom},str}} - 1, \tag{4.9}$$

where $I_{x,z_{nom},str}$ is the cumulative inventory of x at a depth of z_{nom} in the profile that is assumed to have undergone strain. More generally, material-specific bulk densities (i.e., cumulative inventories normalized by their thicknesses, or simply $\rho_b c_x$; Brimhall & Dietrich, 1987) may be used in place of inventories so that samples of different dimensions (e.g., different depth intervals) can be compared. However, I highlight that sample dimensions do, in fact, matter in cases where the bulk density of the material x assumed to be conservative (i.e., $\rho_b c_x$) varies with

depth, which may cause $\hat{\epsilon}_{I_x}$ to deviate from ϵ_z as calculated with (4.8). Approaches similar to (4.9) may be necessary if observations are only available for a single depth interval and/or if strain is assumed to have only occurred within a single interval. For instance, a multiplicative strain adjustment is sometimes applied to topsoil SOC inventories using the ratio of ρ_b for a reference profile to ρ_b of a profile that has undergone strain (Nagy et al., 2018); this ratio equals $\hat{\epsilon}_{I_s} + 1$, where the subscript *s* indicates bulk soil.

4.2.3.2 Implementation

We quantified SOC stocks and mean Δ^{14}C (weighted by SOC mass; Masiello et al., 2004) for each soil profile as follows. First, I estimated ρ_b at the midpoint of each depth interval by linearly interpolating between horizon-based ρ_b observations (note: spline interpolation introduced artifacts in ρ_b in some profiles). Next, for each depth interval, I calculated cumulative inventories of bulk soil mass, SOC, Zr, Ti, and soil mineral mass using (4.1) through (4.4), and I calculated cumulative SOC-weighted mean Δ^{14}C using (4.6)). Prior to calculations, soil mineral mass fraction c_m was approximated as 1 - c_o, where the organic matter fraction c_o was estimated as SOC mass fraction (c_C) divided by 58 (but see Pribyl, 2010 for limitations of this assumption). For clarification, note that all mass fractions express concentrations relative to the mass of fine earth (<2 mm), whereas volumes refer to the space occupied by material of all sizes. ρ_b and (4.1)) were not adjusted according to the volume occupied by coarse fragments (Poeplau et al., 2017) due to the low mass fraction of coarse fragments in the sampled profiles (median: 0.008 g coarse fragments per g soil plus coarse fragments) and uncertainty regarding the density of the variably weathered fragments.

To evaluate how strain may affect estimates of SOC inventories and mean Δ^{14}C, I focused on the upper 25 cm of soil (i.e., z_{nom}=25 cm) and employed four distinct approaches to summarize SOC metrics from the soil surface down to that depth, with and without accounting for strain. All strain-adjustment approaches were applied after grouping soils by soil type and elevation band (i.e., low-elevation Inceptisols and low- and high-elevation Andisols) and taking as a reference the profile within each group with the least evidence of collapse (negative strain) as described below.

For the fixed-depth (FD) approach, cumulative SOC inventories and SOC-weighted mean Δ^{14}C were extracted for the 15–25 cm depth interval (i.e., *n*=7 in my sampling scheme) from each profile ($I_{SOC,z_{nom}}$ and $\overline{\Delta^{14}C}_{SOC,z_{nom}}$). This approach disregarded strain but required no

interpolation.

The remaining three approaches to summarizing SOC metrics each accounted for strain. These approaches followed a consistent procedure and varied only with regards to which materials were assumed to remain constant during strain (total soil mass, soil mineral mass, or mass of a weathering-resistant, geogenic element; Table 4.3). For example, for the equivalent bulk soil mass (ESM) approach, the reference profile in each soil group was identified as the profile with the least cumulative soil mass at 25 cm, $I_{s,z_{nom},ref}$. The SOC inventory and mean Δ^{14}C for the reference profile were equivalent to those obtained with FD ($I_{SOC,z_{nom}}$ and $\overline{\Delta^{14}C}_{SOC,z_{nom}}$). For the other profiles within each group, z_{ESM} and the corresponding SOC inventories and means of Δ^{14}C at z_{ESM} ($I_{SOC,z_{ESM}}$ and $\overline{\Delta^{14}C}_{SOC,z_{ESM}}$) were interpolated as described in the previous section, and strain was estimated using (4.8). This process was repeated for the equivalent mineral mass (EMM) and immobile-element (IE) approaches, using cumulative inventories of the mineral fraction for the former and of Ti or Zr for the latter. In all cases, reference profiles (assumed to have undergone zero strain) were selected solely on the basis of cumulative mass inventories rather than site characteristics. For the two Andisols, these profiles were the mature (selectively logged) forests, but because I was unable to sample Inceptisols under mature forest, this procedure led to selection of profiles from successional sites (C2–1 or C2–2 depending on the material used). In total, these combined approaches yielded up to five distinct SOC inventories and mean Δ^{14}C values and up to four distinct estimates of strain for the upper 25 cm of each profile.

4.2.4 Statistical analyses

To assess pedologic variation within and among the three groups of soil profiles prior to applying strain adjustments, I applied sparse principal components analysis (sPCA; Shen & Huang, 2008) to measured physical and chemical properties and biogeochemically diagnostic ratios (e.g., SOC/nitrogen, Ti/Zr, oxalate–extractable Fe/dithionite–extractable Fe). sPCA integrates the goal of traditional principal components analysis —reducing the dimensionality of a dataset with latent factors that are linear combinations of the original variables—with feature selection by allowing user specification of the number of variables contributing to (or "loading on") each latent factor. Sparse multivariate methods like sPCA are particularly useful for identifying trends in datasets with a large number of variables relative to the number of observations. sPCA provided a data–driven basis for grouping soils at similar stages of development, so that

mass–volume relations can be more confidently attributed to LUC effects rather than inherent pedologic differences. I implemented sPCA using the `mixOmics` package (Rohart et al., 2017) in `R`. To prepare data for sPCA, properties measured on depth intervals rather than on horizons (soil compressive strength, laser diffraction ratios, and concentrations of SOC, nitrogen, Ti, and Zr) were interpolated to the midpoint of each horizon. I applied sPCA in three configurations. I analyzed all available data for dominant mineral horizons (n=64) naively (i.e., ignoring relatedness of horizons with the same profile) and in a multilevel mode (i.e., accounting for horizon relatedness), and I separately analyzed the uppermost mineral horizon per profile (n=16). In each case, variables were centered and scaled prior to analysis, and the first four principal components (PC) were retained, with two variables allowed to load on each PC.

After grouping soils and selecting reference profiles as previously described, I evaluated the effects of ignoring or accounting for strain on calculated SOC inventories and mass-weighted mean $\Delta^{14}C$, both at the level of each profile (0–25 cm nominal depth interval) and in terms of trends across all 16 profiles. To compare each pair of methods, I calculated absolute and relative errors in the two SOC metrics for each profile and the root-mean square error (RMSE) across all profiles. I assessed how different strategies for accounting for strain affected inferences across profiles (LUC effects on SOC inventories and $\Delta^{14}C$) using ordinary least squares (OLS) regressions, with additive terms for soil type and elevation band. The effect of time since disturbance (i.e., years without grazing in successional sites, approximate stand age for reference forests, and zero for pastures) was represented using either a linear term (after assessing potentially nonlinear effects using generalized additive models (Wood, 2003, 2011)) or a categorical variable. In the latter case, pastures and early successional stages were included in one group and intermediate-to-late successional stages and selectively logged forests (<10 versus >10 years) were included in another. This grouping was based on observed differences in vegetation structure (Table 4.2) and upper soil morphology (Oe/Oa horizon thickness; data not shown). Where relevant, I estimated succession–specific effects by omitting the two selectively logged forests from the analysis. Linear contrasts between successional groups were estimated using the emmeans package (Lenth, 2019). Unless otherwise noted, contrasts were estimated as averages across soil types and elevation bands.

General comparisons of soil properties between soil types and across elevations were also conducted using emmeans, in this case in conjunction with mixed-effects models (lme4 package;

Bates et al., 2015). I included a fixed effect for soil group (Inceptisols and low- and high-elevation Andisols) and a random effect for each profile.

4.3 Results

4.3.1 Soil physicochemical properties

Physicochemical measurements and sparse principal components analysis (sPCA) provided quantitative support for the grouping of the 16 profiles into intermediately weathered Andisols (n=12) and more intensely weathered Inceptisols (n=4). Applying sPCA to the full set of mineral horizons (n=64) indicated (Table 4.4; left panel in Fig. 4.3) that the dominant gradient (PC1) among the studied soils was related to the abundance of metastable (organo)mineral phases (i.e., short-range-order aluminosilicates and (oxy)hydroxides and metal-humus complexes), as inferred from oxalate–extractable aluminum (Al_o) and phosphorus retention (P_{ret}, the proportion of experimentally applied phosphorus adsorbed onto soil particles). Variation in carbon concentration and the relative abundance of poorly crystalline iron (oxy)hydroxides (ratio of oxalate-extractable to dithionite-extractable iron, Fe_o/Fe_d) defined a secondary gradient (PC2). This same axis emerged as a dominant gradient after removing profile–specific effects with multilevel sPCA (Table 4.5; center panel in Fig. 4.3), suggesting that this variation was primarily driven by declines in organic matter content and increases in mineral crystallinity with depth. Excluding subsoils from the analysis revealed a gradient in soil physical properties (Table 4.6; right panel in Fig. 4.3), with bulk density ρ_b increasing and the ratio of silt–sized particles/aggregates to clay–sized particles/aggregates decreasing with soil weathering status from Andisols to Inceptisols. The variables identified as loading onto the second component from this single–horizon analysis (oxalate–extractable silicon [Si_o] and pH in 1 M sodium fluoride, proxies for allophane and poorly crystalline aluminum (oxy)hydroxides, respectively) hinted at possible mineralogical variation even within the same soil type. Unexpectedly, these multivariate analyses did not indicate any systematic differences between low– and high–elevation Andisols. However, I maintained separate soil groupings by elevation band for subsequent analyses to account for possible differences in carbon accumulation driven by contrasts in temperature, moisture, and vegetation.

4.3.2 Bulk density, carbon mass fraction, and Δ^{14}C

All soils exhibited low bulk densities (ρ_b) and high carbon mass fractions (c_C, presented here as percentages for clarity). Averaging across all sampled depths, the Inceptisols featured significantly higher ρ_b (estimated marginal mean: 0.63 g cm^{-3} [95% confidence interval: 0.55–0.70 g cm^{-3}]) and lower c_C (7.5% [0.14–14.8%]) than the Andisols, particularly at higher elevations (ρ_b: 0.33 g cm^{-3} [0.28–0.39 g cm^{-3}]; c_C: 23.0% [17.8–28.2%]; $p < 0.0001$ and $p = 0.0065$ for respective linear contrasts with Inceptisols). Lower-elevation Andisols resembled their higher-elevation counterparts in mean ρ_b (0.36 g cm^{-3} [0.29–0.43], $p = 0.8062$ and $p=0.0002$ for linear contrasts with higher-elevation Andisols and Inceptisols, respectively) and featured intermediate values of c_C 14.0% [6.7–21.4]; $p=0.12$ and $p=0.38$).

Apart from differences in means, ρ_b and c_C varied similarly with depth across soil groups but distinctly across successional stages (Figs. 4.4 and 4.5). At intermediate successional stages and under mature forests, c_C decreased exponentially from the soil surface (right panels in Fig. 4.4). In more recently grazed soils, variation in c_C within the upper soil was subdued (left panels in Fig. 4.4). Patterns in ρ_b were generally more complex, broadly mirroring the distribution of c_C but also revealing subsurface heterogeneity (Fig. 4.5). Notably, in soils under pasture and at early successional stages, a zone of elevated ρ_b was distinguished within the upper 25 cm. This observation was supported by *in situ* measurements of compressive strength (Fig. 4.6).

Succession–related patterns were also evident in the depth distributions of bulk soil Δ^{14}C (Fig. 4.7). Overall, Δ^{14}C decreased with depth and reached negative values by the 25–40 cm sample interval in all cases. However, negative values were detected in the uppermost intervals of recently grazed soils (e.g., 0–2 cm in three Andisol profiles), but generally not within the upper 10 cm of soils at later successional stages.

4.3.3 Strain effects on estimated SOC inventories and mean Δ^{14}C

The four materials used to identify soil depths with equivalent masses (Fig. 4.8)—bulk soil mass, soil mineral mass, and the weathering–resistant elements Ti and Zr—yielded consistent estimates of strain ϵ (calculated using (4.8); Table 4.7). Median ϵ across all profiles (excluding reference profiles) ranged from -0.22 (i.e., 22% volume reduction relative to reference profile) when estimated using depths of equivalent soil mass to -0.26 using depths of equivalent Ti mass. Maximum estimated ϵ was -0.61 (mineral mass basis). I found that strain decreased

significantly with time since disturbance at a mean rate of 0.06 ± 0.02 (equivalent soil mass) to 0.08 ± 0.02 (equivalent Ti mass) per decade of succession (p=0.005 to p=0.009 for slope coefficients in OLS models with additive effects for soil type and elevation band and excluding reference profiles). In other words, soils regained approximately 0.6–0.8% of their pre–strain volume per year, averaging across soil types and elevations and without differentiating between increases in porosity and accumulation of mass over time.

Calculating SOC inventories over a fixed depth interval of 0–25 cm—disregarding strain—inflated estimates by 21–47% (median relative errors) relative to strain–adjusted values, with the most severe errors exceeding 100% (maximum absolute errors: 7.3–8.7 kg C m^{-2}). On average, the conventional fixed–depth approach overestimated SOC inventories by 4.0–4.7 kg C m^{-2} (RMSE). Differences in SOC inventories due to the choice of reference material for strain adjustment were much less drastic (median relative errors $\pm$7%; RMSE: 0.7–1.3 kg C m^{-2}; maximum absolute error: 1.4 kg C m^{-2}).

Estimates of SOC persistence also proved to be sensitive to strain. Calculating mean Δ^{14}C weighted by SOC mass ($\overline{\Delta^{14}C}_{SOC}$) in the upper 25 cm of soil (numerically equivalent to extracting a single sample from 0 to 25 cm) without accounting for strain led to systematically lower values. Absolute errors from using a fixed–depth approach ranged from -0.34 to -32.03‰, with average errors of 16.27–18.64‰ (RMSE). As for SOC inventories, differences in $\overline{\Delta^{14}C}_{SOC}$ obtained using different strain–adjustment methods were comparatively minor (RMSE: 2.80–4.88‰).

When analyzing differences in SOC metrics between profiles at early versus intermediate stages of succession, accounting for strain changed the sign of the estimated difference in SOC inventories and yielded more conservative estimates of the difference in $\overline{\Delta^{14}C}_{SOC}$. Statistical power for estimating linear contrasts was generally low, reflecting unconstrained sources of variation (e.g., differences in meter–scale disturbances) as well as the limited number of profiles sampled. Lack of statistical power likely contributed to 95% confidence intervals spanning zero for most contrasts. For the purposes of evaluating the effects of strain adjustments, I highlight qualitative differences in estimates. Focusing on the 14 profiles with historical or contemporary grazing (Fig. 4.9), SOC inventories were estimated to be 1.9–2.8 kg m^{-2} greater at intermediate stages of succession when strain adjustments were applied (respective 95% CIs: -0.2–4.0 and -0.2–5.7 kg m^{-2}) or insignificantly lower when strain was ignored (-0.7 kg m^{-2},

95% CI: -3.9–2.4 kg m^{-2}). Including the two selectively logged forests in the analysis, estimated differences in SOC inventories between sites with <10 versus >10 years since major disturbance were significant (i.e., did not include zero) only after accounting for strain (data not shown). For $\overline{\Delta^{14}C_{SOC}}$, less recently disturbed sites were estimated to have slightly higher values (Fig. 4.10), though this difference was only found to be significant if strain was ignored and selectively logged forests were considered (estimated contrast: 44.40‰, 95% CI: 2.6–86.24‰). Analyzing strain–adjusted $\overline{\Delta^{14}C_{SOC}}$ values reduced the estimated difference between successional groups to approximately 31—36‰ (95% CI spanning -10–79‰ across strain–adjustment approaches), with marginally more convincing evidence of a significant difference if selectively logged forests were considered.

While I focused here on the effects of strain adjustments on inferred land-use effects on SOC metrics, I found that differences in SOC inventories between soil types and elevation bands were similarly sensitive to how strain was addressed (e.g., 3.2 ± 1.4 kg m^{-2} [p=.052] greater inventory for fixed–depth approach; no significant difference after accounting for strain). No systematic differences between soil types or elevation bands were detected for $\overline{\Delta^{14}C_{SOC}}$, regardless of how strain was addressed.

4.4 Discussion

4.4.1 SOC dynamics and volume change

Choosing a depth interval over which to study and compare soils is a critical step in quantifying changes in soil properties through time and space. While exact depths vary among studies and disciplines (Marín-Spiotta & Sharma, 2013), keeping depths consistent (fixed) when analyzing and reporting data undoubtedly remains the most common practice. My findings add to existing—but widely unheeded—evidence that the fixed–depth approach leads to major errors when soils have undergone volume change (strain, ϵ), whether due to changes in mass or porosity (Jenkinson, 1971; Murty et al., 2002; von Haden et al., 2020). Assuming that the soils I studied had lost volume during deforestation and grazing, I found that using a fixed–depth approach would overestimate SOC inventories in the upper 25 cm by 4.0–4.7 kg C m^{-2} on average (21–47% median relative error), a magnitude similar to the differences in SOC inventories between sites (Table 4.8). This overestimation was more severe for soils under pasture and at early stages of forest succession (within 10 years of grazing). Consequently, these soils appeared to

store slightly more SOC per area than soils at later successional stages on a fixed–depth basis, though this difference was highly uncertain (0.7 kg m^{-2}, 95% CI: -2.4–3.9 kg m^{-2}). Using strain–adjusted estimates of SOC inventories led to the opposite conclusion (Fig. 4.9). This finding was consistent with previous observations that the estimated effects of land-use change on SOC storage differ between fixed–depth and equivalent mass approaches (Don et al., 2011; Crow et al., 2016).

Beyond reaffirming that fixed–depth SOC inventories are overestimated when soil volume has been reduced (Fig. 4.1), I demonstrated that strain may also bias fixed–depth interpretations of radiocarbon measurements. I assessed how ignoring strain could affect estimates of SOC persistence as inferred from bulk soil radiocarbon activity by calculating SOC–weighted mean $\Delta^{14}C$ in the upper 25 cm ($\overline{\Delta^{14}C}_{SOC}$). For all profiles assumed to have undergone strain, fixed–depth estimates of $\overline{\Delta^{14}C}_{SOC}$ were lower than strain–adjusted values by 16.27–18.64‰ on average, so that recent SOC inputs (i.e., "modern" C) appeared to be relatively less abundant on a fixed–depth basis. Despite significant potential bias in $\overline{\Delta^{14}C}_{SOC}$ for individual soils (Table 4.9), accounting for strain did not dramatically change the estimated difference in $\overline{\Delta^{14}C}_{SOC}$ between successional stages (Fig. 4.10). This consistency suggests that the generally lower values of $\Delta^{14}C$ detected in upper soils of pastures and at early successional stages (Fig. 4.7) in this study and previous findings of land-use effects on radiocarbon values (Henry et al., 2013; Nagy et al., 2018; Finstad et al., 2020; Jiang et al., 2020) reflect real differences in carbon cycling and not simply errors from the sampling of deeper SOC in compacted soils (Fig. 4.1). Nonetheless, my finding of systematic negative bias from fixed–depth analysis of $\Delta^{14}C$ underscores that improving the accuracy of estimated land-use effects on SOC cycling requires consideration of dynamic soil volume in sampling designs (e.g., sampling of finer depth intervals near the soil surface) and data analysis approaches.

4.4.2 Towards informed adoption of strain–adjustment approaches

While the differences in results obtained from fixed–depth and strain–adjusted approaches are clear, how to identify which approach best approximates reality is not. Methodological errors in estimated soil properties may be mitigated by assessing the physical relationships between mass fractions of soil components and soil volume implicitly assumed by each method (Table 4.3). In contexts in which organic matter is expected to vary, a fixed–depth approach will only refer to a consistent volume (and be less prone to the aforementioned errors) if added organic matter

fills in pre-existing pore space and/or the pore space remaining after organic matter loss does not collapse (Sollins & Gregg, 2017). This situation implies an inverse relationship between organic matter (or carbon mass fraction) and porosity. How far a particular set of soil observations deviates from this relationship can be evaluated graphically to guide decisions about strain adjustments (Fig. 4.11).

Most approaches to accounting for strain in observational contexts (i.e., when initial soil volume prior was not measured) assume zero change in either total soil mass or soil mineral mass (i.e., solids other than organic matter) on the time scale of the processes inducing strain and then use that mass as the basis for comparisons across soils (or in time) in lieu of depth (Jenkinson, 1971; Ellert & Bettany, 1995; Gifford & Roderick, 2003; Wendt & Hauser, 2013; Rovira et al., 2015). The assumption of constant total soil mass implies that volume change only reflects changes in porosity and that mineral and organic matter masses are conserved (Sollins & Gregg, 2017; von Haden et al., 2020), which is clearly not the case when land-use change has resulted in net gains or losses of organic matter (e.g., through increased respiration; Campos C., 2006). The assumption of constant mineral mass may be reasonable in soils with crystalline mineralogy, but in soils characterized by relatively labile (organo)mineral phases (e.g., metal–humus complexes in Andisols and Spodosols), net loss of mineral mass from the upper soil may occur on decadal time scales (Verde et al., 2005; Basile-Doelsch et al., 2009).

To apply strain adjustments in settings in which neither total soil mass nor mineral mass can be confidently assumed to remain constant, I proposed the use of the mass of an individual weathering–resistant element as a proxy for pre–strain soil volume. This approach is essentially a generalization of the method of Brimhall & Dietrich (1987) that has primarily been used to estimate strain associated with mineral weathering on centennial to millennial time scales (Egli et al., 2006; Heckman & Rasmussen, 2011). I implemented the proposed approach separately using Ti and Zr, both of which may be mobile in specific pedogenic environments over millennial scales (Kaup & Carter, 1987; Kurtz et al., 2000) but can be assumed immobile on the time scale of land-use change. For the profiles assumed to have undergone strain relative to reference profiles, the immobile–element approach agreed reasonably well with the equivalent soil mass and equivalent mineral mass approaches, whether assessed in terms of strain, SOC inventories, or $\overline{\Delta^{14}C}_{SOC}$ (Fig. 4.8, Tables 4.7–4.9). Agreement between the immobile element and equivalent mineral mass approaches was expected due to the tight correlations between the

mineral mass fraction (1 - percent carbon/58) and the selected elements (Pearson correlation coefficients: 0.90 and 0.93 for Ti and Zr, respectively). These relationships indicate that dilution by plant–derived materials was the primary driver of variations in the concentrations of these parent material–derived elements.

Taking these findings as evidence that mineral mass remained approximately constant in response to land–use change (necessarily disregarding erosion; von Haden et al., 2020), I contend that plots of the accumulation of mineral mass with depth (i.e., cumulative mineral mass inventories) may be useful tools for diagnosing the potential degree of strain for sets of profiles without measurements of immobile elements. Cumulative mineral mass inventories of the 16 profiles analyzed in this study and 42 additional profiles sampled in the same landscape illustrate this approach (Fig. 4.12). First, discrete groups of profiles can be distinguished, indicating inherent differences in bulk density and carbon concentration among profiles due to factors other than land use, in this case reflecting contrasting stages of geochemical evolution. Profiles can be grouped *a priori* or using taxonomic proxies (oxalate–extractable aluminum and iron concentrations in this example). Figure 4.12 reveals that groups may also be determined directly from this plot when additional contextual information is lacking. For a group of soils, maximum potential strain at a particular reference depth z_{nom} (e.g., 40 cm in the left panel, 100 cm in the right) is estimated as follows. For the case of collapse, the minimum cumulative mineral mass inventory observed at the reference depth (I_{mznom}) is identified, and then the shallowest depth (z_{EMM}) at which another profile within the same group reaches that same inventory (I_{mznom}) is noted and strain is calculated as $\frac{z_{EMM}}{z_{nom}} - 1$. For the case of dilation, the opposite extremes are used (i.e., I_{mznom} is the maximum cumulative mineral mass inventory at z_{nom}, and z_{EMM} is the deepest depth at which I_{mznom} is reached). This procedure may help to differentiate between biophysical versus potentially anthropogenic drivers of soil mass–volume relations and put comparisons between pairs of profiles in a broader landscape context. Probabilistic estimation of strain (e.g., generating distributions of strain that reflect the variability of potential reference profiles) is a priority for future extensions of this work.

4.5 Tables

Site	Elevation (m)	Soil order	Geologic map unit		Slope (°)	Aspect (°)
			1:250 000	1:50 000		
C5-1	1352	Inceptisol	Q(Tb)	TplQptTA-A	25	138
C1-3	1401	Andisol	Q(Tb)	QhoPc3	34	29
C1-1	1412	Andisol	Q(Tb)	QhoPc3	34	174
C1-2	1425	Andisol	Q(Tb)	QhoPc3	27	34
C2-1	1425	Inceptisol	Q(Tb)	TplQptTA-A	38	180
C2-2	1466	Inceptisol	Q(Tb)	TplQptTA-A	35	12
C3-1	1513	Andisol	Ts(Ti)	TplQptTA-A	33	149
C4-1	1554	Inceptisol	Ts(Ti)	TplQptTA-A	35	82
M1-2	2055	Andisol	Ts(Ti)	TplQptTA-A	38	67
M1-4	2062	Andisol	Ts(Ti)	TplQptTA-A	29	201
M1-3	2107	Andisol	Ts(Ti)	TplQptTA-A	38	28
M3-1	2153	Andisol	Ts(A)	TplQptTA-A	27	114
M1-1	2164	Andisol	Ts(Ti)	TplQptTA-A	35	67
M2-3	2199	Andisol	Ts(Ti)	TplQptTA-A	33	4
M2-1	2216	Andisol	Ts(Ti)	TplQptTA-A	45	286
M2-2	2219	Andisol	Ts(Ti)	TplQptTA-A	29	183

Table 4.1: Soil types were assigned to profiles based on the physicochemical analyses conducted in this study. Surface geologic units mapped at a scale of 1:250 000 (INEGI, 1984): Q(Tb): Quaternary basic tuff; Ts(Ti): Pliocene intermediate tuff; Ts(A): Pliocene andesite. Surface geologic units mapped at a scale of 1:50 000 (Servicio Geológico Mexicano, 2007b,a): TplQptTA-A: Plio-Pleistocene andesite and andesitic tuff; QhoPc3: Holocene pyroclastics. Slope and aspect were measured 5 m upslope and 5 m downslope of each profile and averaged.

Site	Years without grazing	Overstory age (years)	Representative tree species	Basal area (m^2 ha^{-1})	Canopy cover
C1-2	0	0	V. farnesiana	0	0
C5-1	2	2	Quercus sp.	2	0.15
C1-1	5	62	Quercus sp.	18	0.78
C2-1	7	7	L. styraciflua	7	0.52
C2-2	12	12	L. styraciflua	21	0.74
C4-1	28	28	L. styraciflua, C. occidentalis	37	0.96
C3-1	33	33	Mixed LMCF	41	0.87
C1-3	—	80	Mixed LMCF	39	0.88
M2-3	0	14	A. acuminata	9	0.28
M2-2	2	16	A. acuminata	2	0.18
M1-4	3	3	A. acuminata, Brunelia sp.	3	0.48
M1-2	9	9	A. acuminata	18	0.72
M3-1	23	23	A. acuminata	37	0.82
M1-3	33	33	A. acuminata	23	0.88
M1-1	62	62	Quercus sp.	25	0.93
M2-1	—	80	Quercus sp., A. acuminata	14	0.84

Table 4.2: Site vegetation characteristics. Current pastures are indicated as sites with zero years without grazing; reference forests (selectively logged but never clear-cut) are sites with no years without grazing reported. Overstory ages were estimated for trees within 10 m of the sampling point; in some sites, trees were present prior to succession. Full species names: Vachellia farnesiana, Liquidambar styracifluia, Clethra occidentalis, Alnus acuminata. Mixed LMCF: diverse assemblage of species typical of lower montane cloud forest.

Varying attribute(s)	Attribute(s) assumed constant	Approach			
		Immobile element	Equivalent mineral mass	Equivalent soil mass	Fixed depth
Porosity, organic matter mass (inverse variation)	Volume, mineral mass	✓	✓	✓	✓
Porosity	Organic matter mass, mineral mass	✓	✓	✓	
Porosity, organic matter mass (independent variation)	Mineral mass	✓	✓		
Porosity, organic matter mass, mineral mass (independent variation)	Mass of weathering-resistant element(s)	✓			

Table 4.3: Applicability of different approaches of depth integration (i.e., strain adjustments plus fixed-depth basis) to contrasting scenarios of variation in soil mass and volume.

	PC1	PC2	PC3	PC4
C	0	0.821	0	0
ρ_b	0	0	0.048	0
Al_o	0.707	0	0	0
Fe_o/Fe_d	0	0.571	0	0
C/N	0	0	0	0.445
P_{ret}	0.707	0	0	0
R_s	0	0	0.999	0
(100–1000 μm) / (10–100 μm)	0	0	0	-0.896

Table 4.4: Factor loadings for sparse principal components analysis of all mineral horizons (n = 64). C = carbon concentration, ρ_b = soil bulk density, Al_o = oxalate–extractable aluminum concentration, Fe_o/Fe_d = ratio of oxalate–extractable iron to dithionite–extractable iron, C/N = carbon-to-nitrogen ratio, P_{ret} = phosphorus retention, R_s = soil compressive strength, (100–1000 μm) / (10–100 μm) = laser particle size ratio (approximately sand:silt).

	PC1	PC2	PC3	PC4
C	0.708	0	0	0
ρ_b	0	0	0.760	0
Al_o	0	-0.755	0	0
Si_o	0	-0.655	0	0
Fe_o/Fe_d	0.706	0	0	0
C/N	0	0	0	0.086
(100–1000 μm) / (10–100 μm)	0	0	0	-0.996
Ti/Zr	0	0	-0.650	0

Table 4.5: Factor loadings for sparse principal components analysis of all mineral horizons in a multilevel mode (highlighting within–profile variation). C = carbon concentration, ρ_b = soil bulk density, Al_o = oxalate–extractable aluminum concentration, Si_o = oxalate–extractable silicon concentration, Fe_o/Fe_d = ratio of oxalate–extractable iron to dithionite–extractable iron, C/N = carbon-to-nitrogen ratio, (100–1000 μm) / (10–100 μm) = laser particle size ratio (approximately sand:silt), Ti/Zr = titanium-to-zirconium ratio.

	PC1	PC2	PC3	PC4
ρ_b	-0.708	0	0	0
pH_{KCl}	0	0	0	0.296
pH_{NaF}	0	0.568	0	0
Si_o	0	0.823	0	0
Fe_o	0	0	-0.877	0
C/N	0	0	0	0.955
(10–100 μm) / (1–10 μm)	0.707	0	0	0
Ti/Zr	0	0	-0.480	0

Table 4.6: Factor loadings for sparse principal components analysis of uppermost mineral horizons per profile (n=16). ρ_b = soil bulk density, pH_{KCl} = pH in 1 M KCl, pH_{NaF} = pH in 1 M NaF, Si_o = oxalate–extractable silicon concentration, Fe_o = oxalate–extractable iron concentration, C/N = carbon-to-nitrogen ratio, (10–100 μm) / (1–10 μm) = laser particle size ratio (approximately silt:coarse clay), Ti/Zr = titanium-to-zirconium ratio.

			ϵ			
Elevation band	Soil type	Site	Soil mass	Mineral mass	Ti	Zr
1350-1550 m	Andisol	C1-2	-0.44	-0.43	-0.48	-0.42
		C1-1	-0.2	-0.25	-0.3	-0.25
		C3-1	-0.07	-0.04	-0.06	-0.05
		C1-3	0	0	0	0
	Inceptisol	C5-1	-0.24	-0.26	-0.4	-0.42
		C2-1	-0.01	0	0	0
		C2-2	0	-0.03	-0.08	-0.06
		C4-1	-0.002	-0.02	-0.26	-0.16
2050-2220 m	Andisol	M2-3	-0.46	-0.53	-0.49	-0.46
		M2-2	-0.45	-0.51	-0.46	-0.42
		M1-4	-0.51	-0.61	-0.59	-0.55
		M1-2	-0.26	-0.38	-0.37	-0.34
		M3-1	-0.18	-0.12	-0.07	-0.1
		M1-3	-0.28	-0.34	-0.17	-0.36
		M1-1	-0.15	-0.18	-0.09	-0.12
		M2-1	0	0	0	0

Table 4.7: Estimates of strain (ϵ) in the upper 25 cm of each profile, using different materials as mass–conservative proxies. For each material, ϵ within each soil group (soil type by elevation band) was calculated relative to the profile with the smallest cumulative inventory of that material at 25 cm; hence, values of zero indicate profiles used to define equivalent masses. Depths of equivalent mass of each material (large points in Fig. 4.8) are recovered as $(\epsilon + 1)(25\text{ cm})$.

			SOC inventory (kg m^{-2})				
Elevation band	Soil type	Site	Fixed depth	Soil mass	Mineral mass	Ti	Zr
1350-1550 m	Andisol	C1-2	14.6	9.6	9.8	8.7	10
		C1-1	8.1	6.9	6.5	6.1	6.5
		C3-1	11.5	10.9	11.2	11	11.1
		C1-3	9.1	—	—	—	—
	Inceptisol	C5-1	12.2	10.1	9.8	8.3	8.0
		C2-1	13.2	13.1	—	—	—
		C2-2	10.5	—	10.4	10.2	10.3
		C4-1	11.6	11.6	11.5	9.3	10.2
2050-2220 m	Andisol	M2-3	16.6	9.2	7.9	8.6	9.3
		M2-2	17.5	10.1	8.9	9.9	10.6
		M1-4	14.2	7.5	6	6.3	6.9
		M1-2	9.6	6.8	5.4	5.5	5.9
		M3-1	15.5	13.1	13.8	14.5	14.3
		M1-3	12.7	9.6	8.7	10.2	8.6
		M1-1	13.3	11.6	11	11.9	11.8
		M2-1	12.4	—	—	—	—

Table 4.8: Soil organic carbon inventories calculated for the nominal upper 25 cm of soil on a fixed–depth basis versus using equivalent masses of different materials assumed to be immobile. Redundant values were omitted where no strain adjustment was applied (i.e., for profiles used as references).

			$\overline{\Delta^{14}C}_{SOC}$(‰)				
Elevation band	Soil type	Site	Fixed depth	Soil mass	Mineral mass	Ti	Zr
1350-1550 m	Andisol	C1-2	-43.18	-20.55	-21.01	-18.4	-21.42
		C1-1	-79.12	-61.45	-56.99	-52.28	-56.31
		C3-1	37.06	44.07	40.69	43.4	42.36
		C1-3	-5.54	—	—	—	—
	Inceptisol	C5-1	14.94	21.53	22.33	26.26	26.38
		C2-1	-38.38	-38.04	—	—	—
		C2-2	-14.97	—	-13.73	-11.2	-12.21
		C4-1	34.07	34.2	34.83	46.89	42.26
2050-2220 m	Andisol	M2-3	-70.44	-42.42	-38.41	-40.63	-42.87
		M2-2	39.99	49.74	46.45	49.06	51.33
		M1-4	-81.4	-62.35	-61.73	-61.87	-62.12
		M1-2	-36.95	-17.4	-7.97	-8.63	-10.66
		M3-1	-7.7	5.52	4.09	-1.02	0.18
		M1-3	-30.09	-10.41	-6.3	-11.9	-6.38
		M1-1	4.16	22.47	25.76	19.74	22.3
		M2-1	43.71	—	—	—	—

Table 4.9: Mass-weighted means of radiocarbon activity calculated for the nominal upper 25 cm of soil on a fixed–depth basis versus using equivalent masses of different materials assumed to be immobile. Redundant vlues were omitted where no strain adjustment was applied (i.e., for profiles used as references)

4.6 Figures

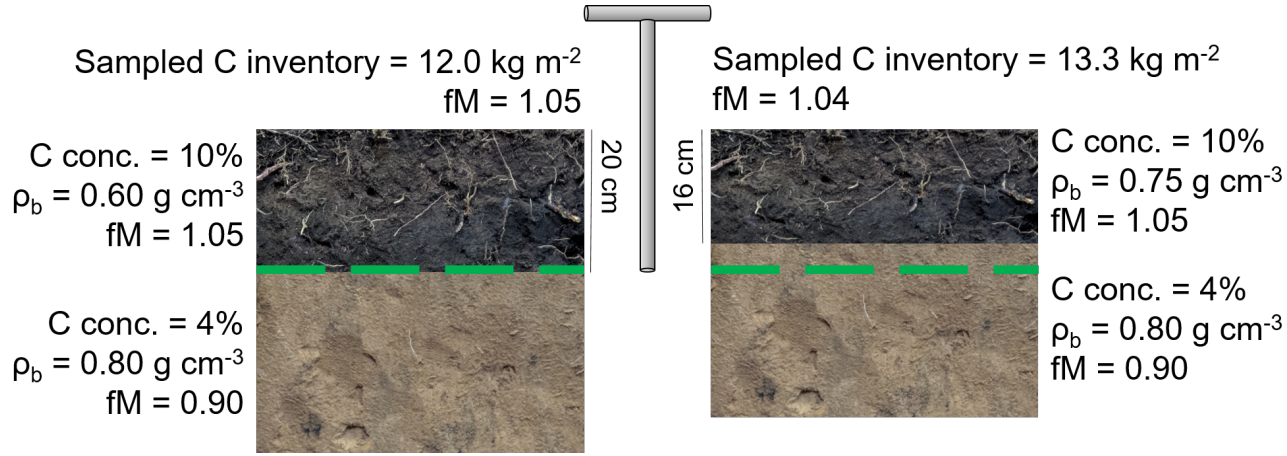

Figure 4.1: Illustration of how fixed-depth sampling can lead to errors in estimated soil organic carbon (SOC) inventories and the fraction of modern (fM) radiocarbon within a sample. In this hypothetical example, volume is reduced by 20% (i.e., strain = -0.2) due to a loss of porosity with no actual change in mass. The SOC inventory calculated at 20 cm increases with the sampling of additional mass, whereas fM decreases (that is, SOC appears to cycle more slowly on average) because the profile is effectively sampled to a greater depth.

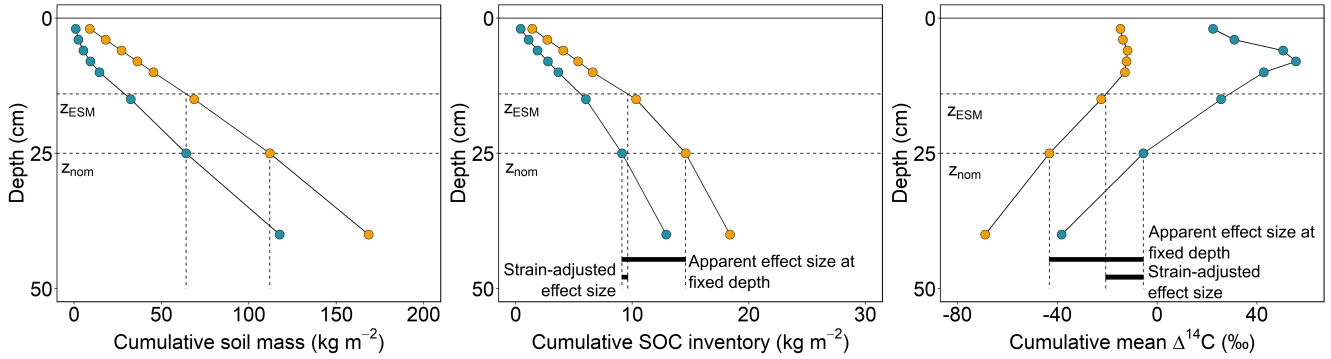

Figure 4.2: Visualization of the general strategy for strain adjustments. The strain–adjustment approaches compared in this study use different proxies to estimate the pre–strain soil volume but follow the same basic steps. Left: the soil in the denser profile (yellow points) is assumed to have undergone negative strain (collapse) relative to the reference profile (blue points). Further assuming that soil mass did not change over that time frame, strain is accounted for by identifying the depth that gives an equivalent soil mass (ESM): z_{nom} in the reference profile and z_{ESM} in the profile that has undergone strain. In this example, strain (z_{ESM}/z_{nom} - 1) is estimated to be -0.44. Center: SOC stored from 0 to 25 cm is 5.5 kg m^{-2} (60%) greater in the denser profile when strain is ignored, compared to a difference of 0.5 kg m^{-2} (5%) when profiles are compared on an ESM basis. Right: Δ^{14}C weighted by SOC mass is 37.6‰ lower in the denser profile at a fixed depth of 25 cm but only 15.0‰ lower on an ESM basis. Data in this example are from low–elevation Andisols under mature forest (blue points) and pasture (yellow points).

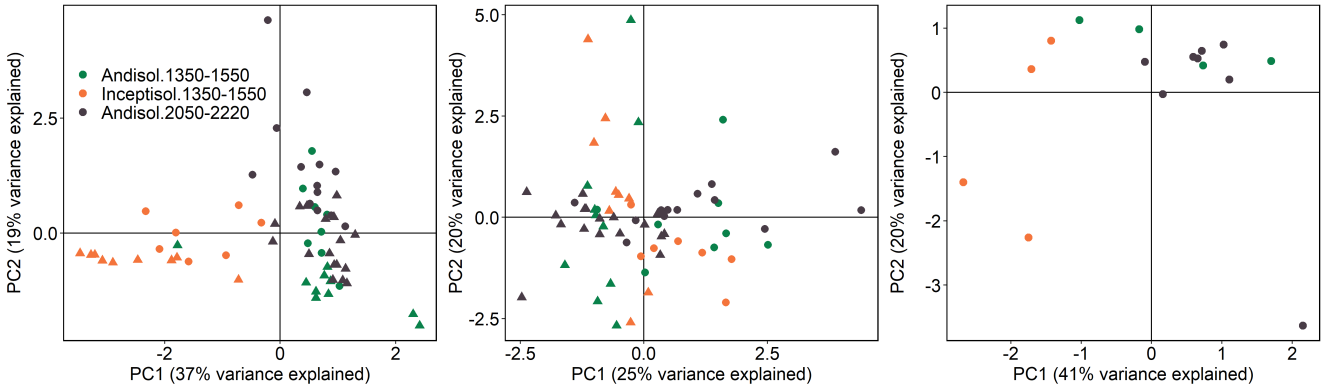

Figure 4.3: Sample scores for the first two factors from sparse principal components analysis (sPCA). Left: analysis of all mineral horizons; center: multilevel analysis of mineral horizons (removing profile effects); right: analysis of uppermost mineral horizons. Triangles indicate subsoil horizons (upper depth below 25 cm). See Tables 4.4–4.6 for factor loadings (omitted from plots for clarity).

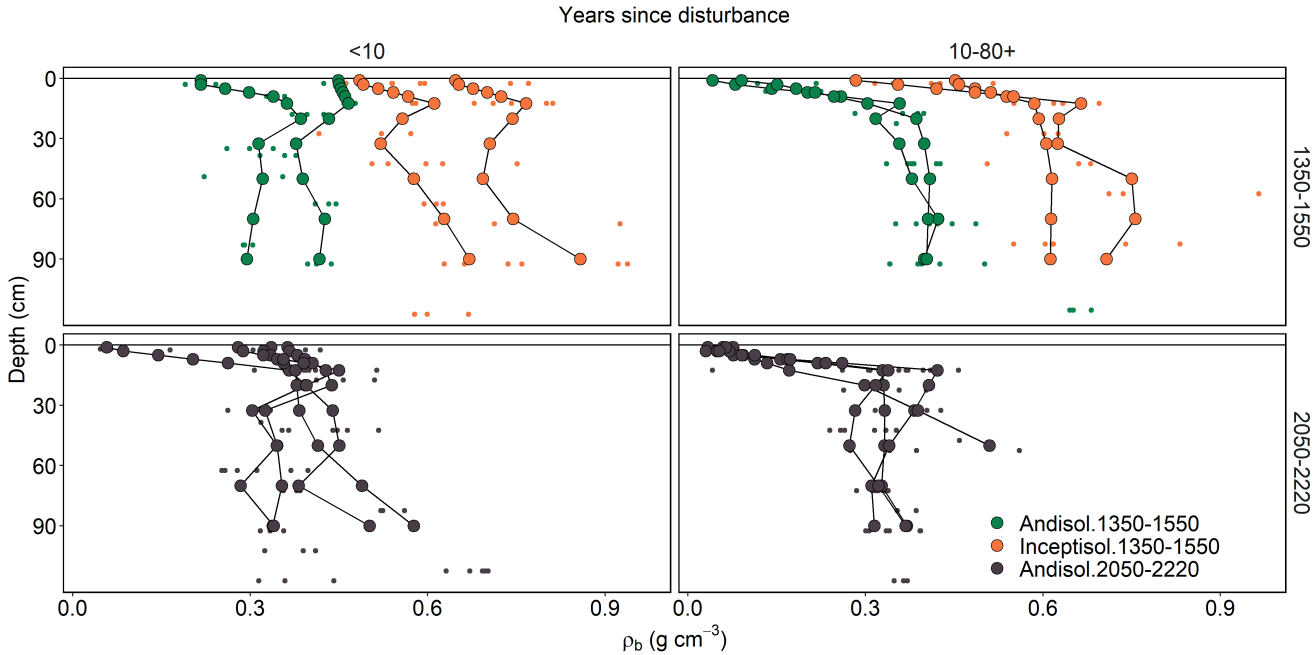

Figure 4.4: Depth distributions of soil bulk density. Smaller points indicate original horizon–based measurements; larger points are interpolated values on a consistent depth–interval basis for use in strain adjustments.

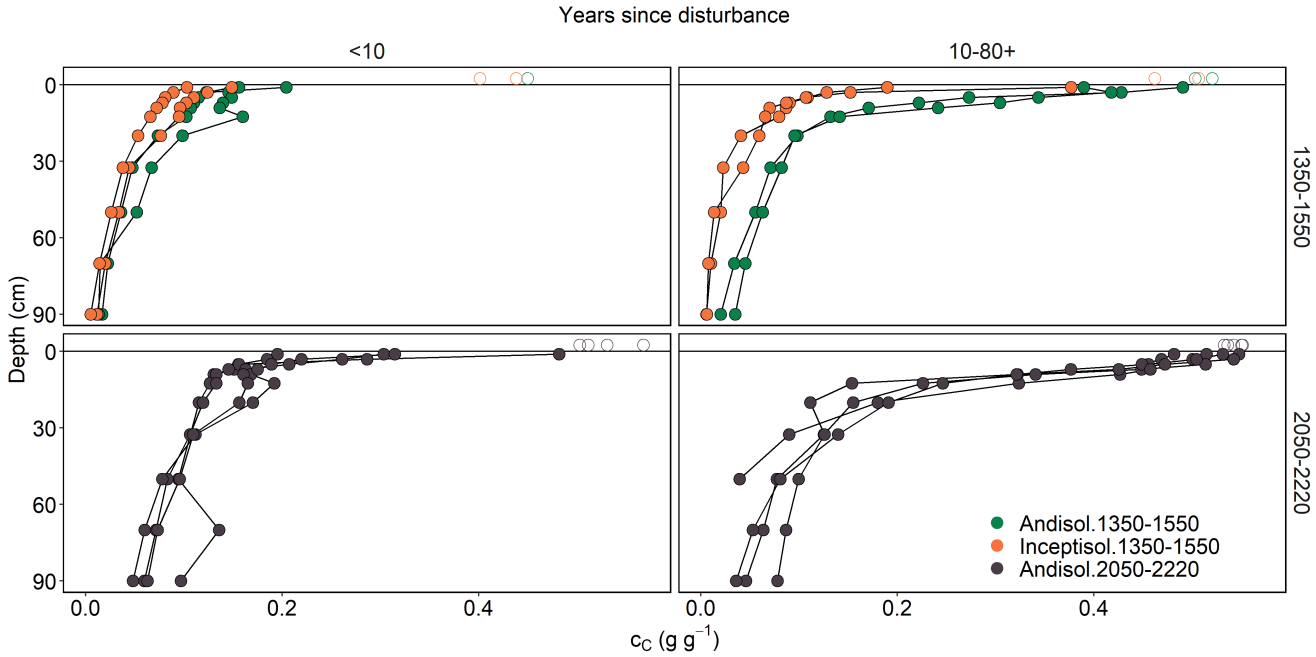

Figure 4.5: Depth distributions of soil organic carbon mass fraction. Open circles (above zero depth) indicate carbon contents of relatively undecomposed leaf litter (Oi horizons).

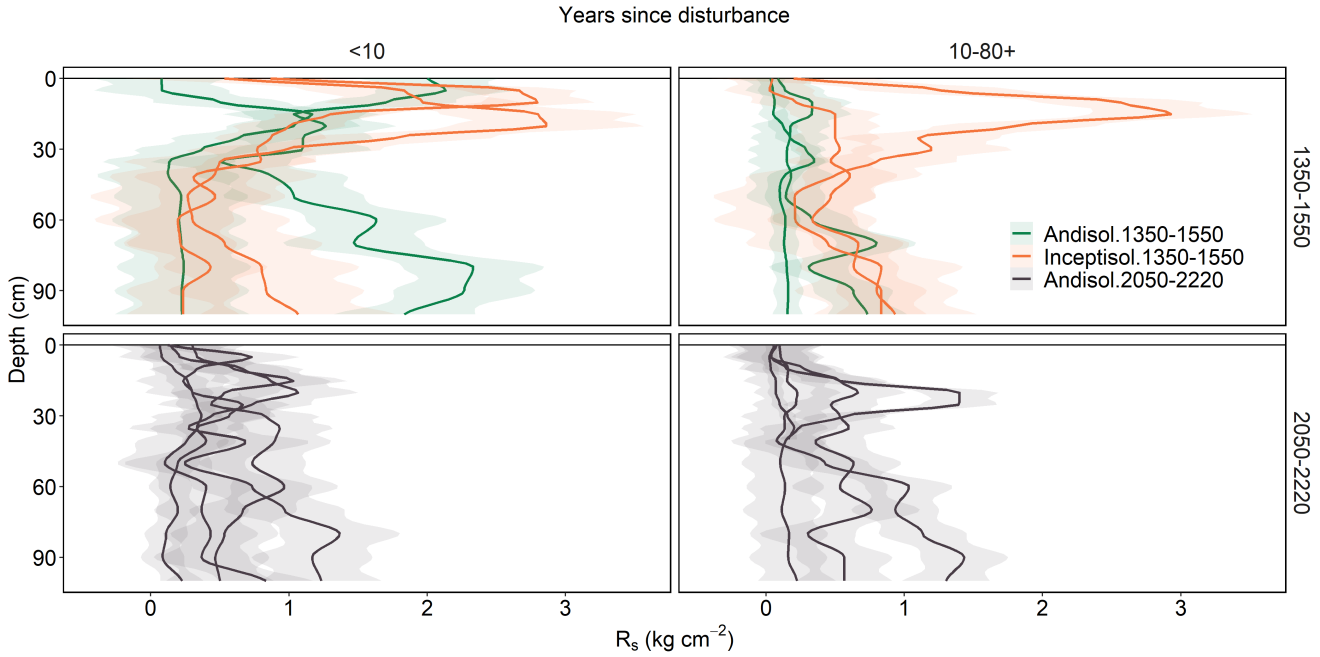

Figure 4.6: Soil compressive strength measured in situ with a pocket penetrometer. Curves are locally weighted regressions fit to observations spaced in 5–cm increments from 0–40 cm and in 10–cm increments from 40–100 cm. Shaded envelopes indicate standard errors.

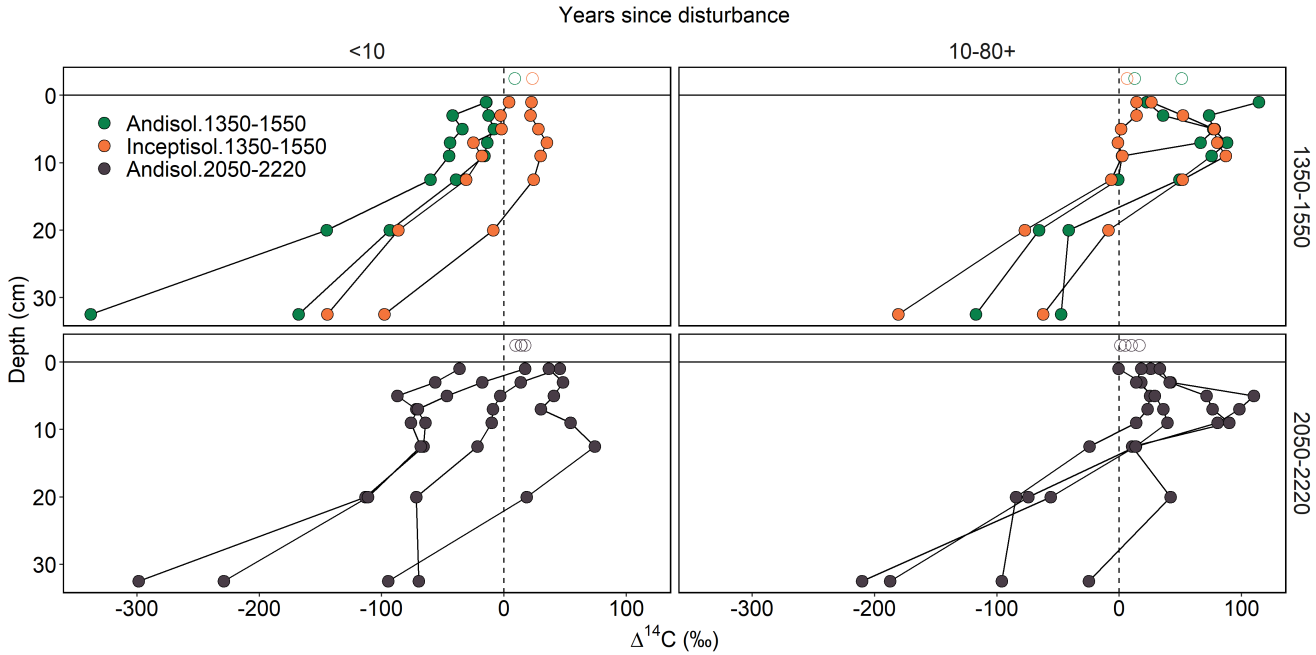

Figure 4.7: Depth distributions of bulk soil radiocarbon activity ($\Delta^{14}C$) within the upper 40 cm. Points are positioned at midpoints of sample depth intervals. Open circles (above zero depth) indicate $\Delta^{14}C$ of relatively undecomposed leaf litter (Oi horizons).

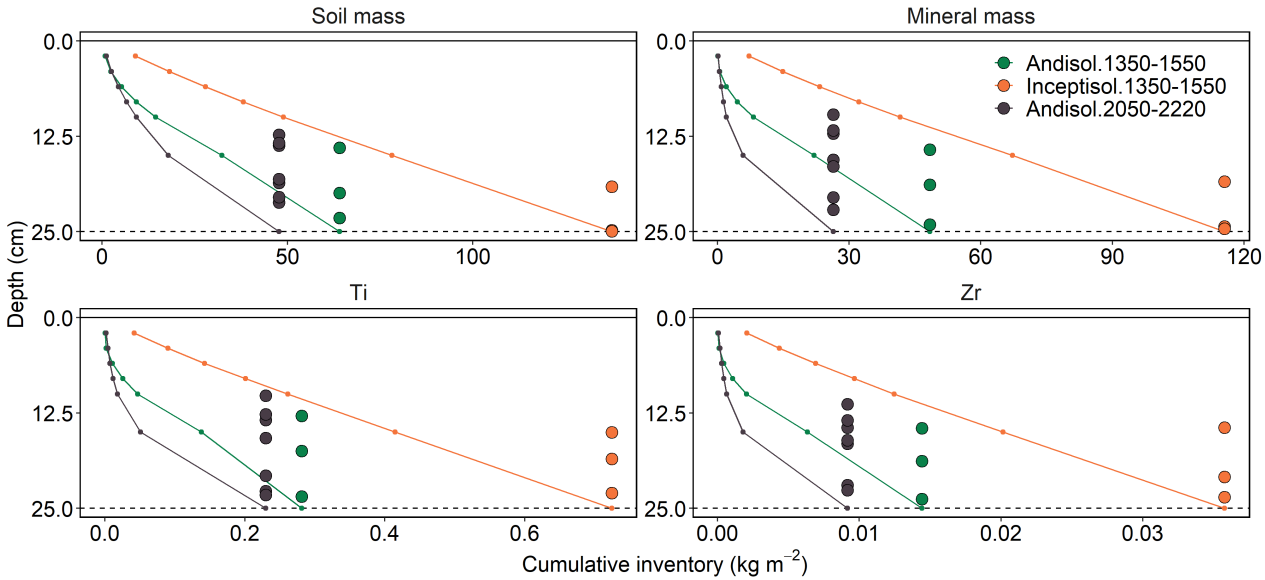

Figure 4.8: Depths used for strain adjustment. Each panel indicates the cumulative inventories of a material used as a conservative proxy for strain. Reference profiles within each soil group (smaller points connected by lines) were identified as those with the smallest inventories of a particular proxy at the nominal depth of 25 cm. Larger points indicate the depths in the other profiles within each group (assumed to have undergone strain) at which an equivalent cumulative mass inventory is obtained.

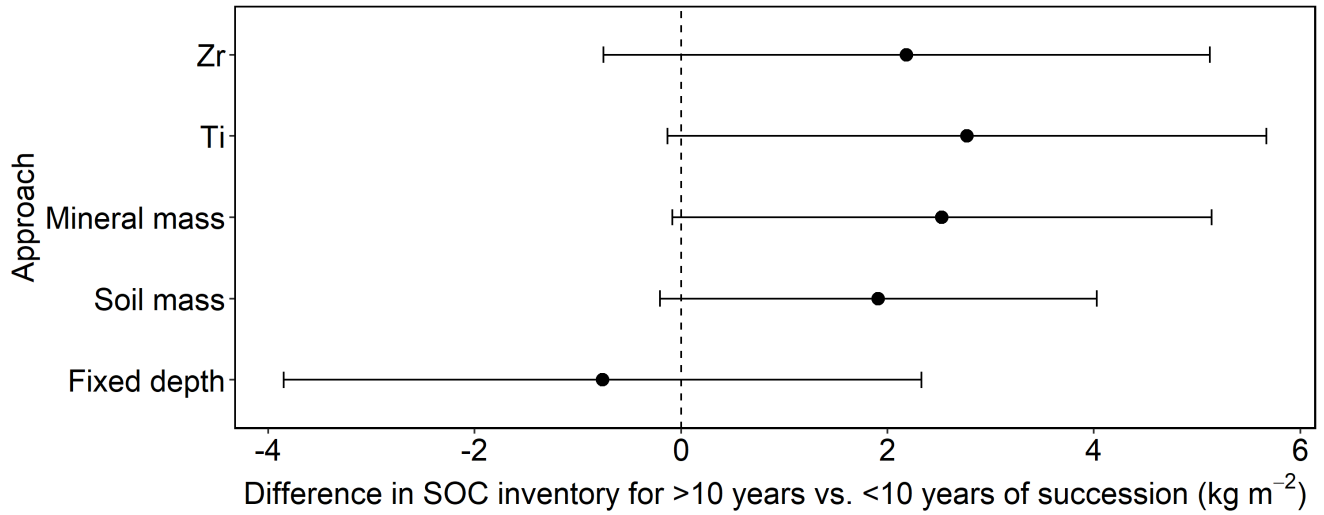

Figure 4.9: Estimated differences in mean SOC inventories between profiles grouped by successional stage. Values refer to the interval from the soil surface to a nominal depth 25 cm. Different estimates were obtained depending on the approach used to determine post–strain depth for summation. Error bars indicate 95% confidence intervals. Estimates refer to succession–specific analysis, excluding selectively logged forests.

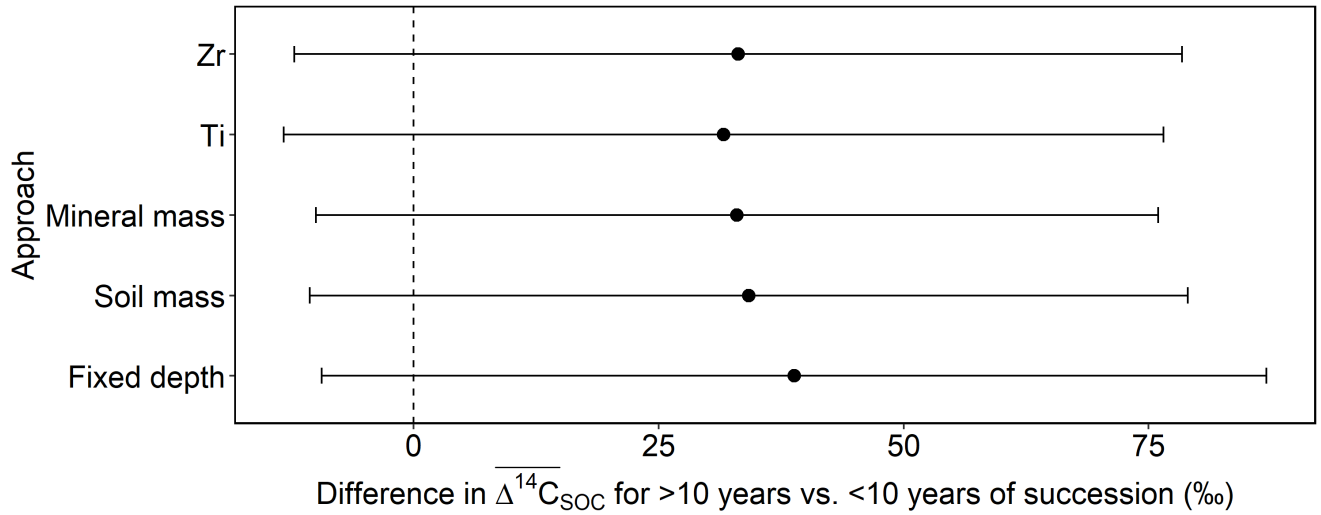

Figure 4.10: Estimated differences in SOC–weighted $\Delta^{14}C$ between profiles grouped by successional stage. Values refer to the interval from the soil surface to a nominal depth 25 cm. Different estimates were obtained depending on the approach used to determine post–strain depth for averaging. Error bars indicate 95% confidence intervals. Estimates refer to succession–specific analysis, excluding selectively logged forests.

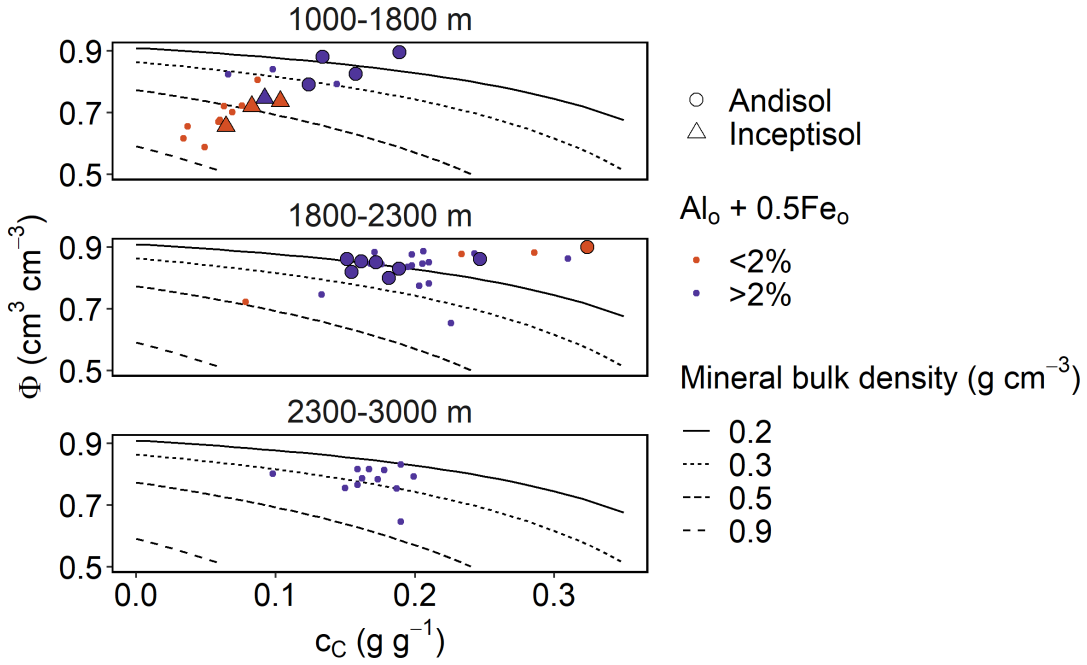

Figure 4.11: Diagnosis of deviations from isovolumetric mass change using soil organic carbon mass fraction (c_C) and porosity (Φ). Data from A horizons of 42 profiles sampled in an adjacent catchment are included for reference (smaller points); for these soils, Φ was calculated using measured mineral particle densities ($\rho_{p,m}$). For the 16 soils sampled in this study (larger points), $\rho_{p,m}$ was assumed equal to 2.2 g cm^{-3} (median value measured from the other 42 profiles). Points are color-coded to distinguish broad differences in mineral weathering status as a proxy for soil type (oxalate criterion for andic soils). Theoretical curves depicting how Φ would vary if c_C were to change without a concomitant change in soil volume were calculated as $\Phi = 1 - \frac{\rho_{b,m}}{\rho_{p,m}} - \frac{\rho_{b,o}}{\rho_{p,o}}$. Mineral bulk density ($\rho_{b,m}$) was assumed to be constant for each curve, with only organic matter contributing to changes in soil mass, represented by organic matter bulk density ($\rho_{b,o}$). The particle density ($\rho_{p,o}$) and carbon content of organic matter were assumed constant at 1.3 g cm^{-3} and 58%, respectively (Sollins & Gregg, 2017), and $\rho_{p,m}$ was again assumed to be 2.2 g cm^{-3}. For a constant volume, $\rho_{b,o}$ was calculated as $\frac{\rho_{b,m} c_o}{1 - c_o}$, with organic matter mass fraction $c_o = c_C/0.58$.

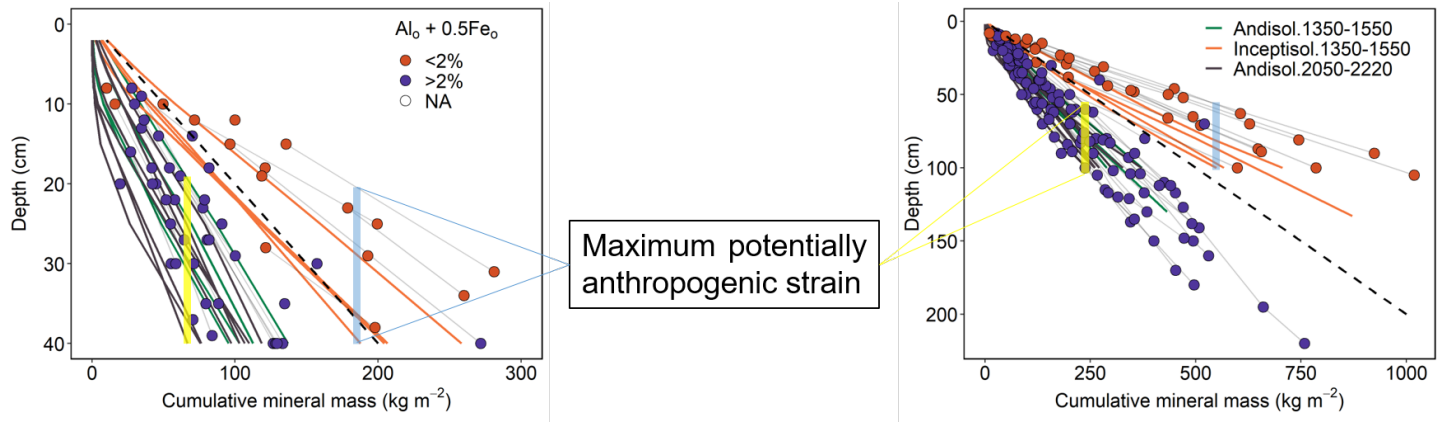

Figure 4.12: Cumulative inventories of soil mineral mass as a graphical tool for assessing land-use–related strain in heterogeneous landscapes. Left: cumulative inventories for upper 40 cm in 58 profiles. Right: cumulative inventories to the maximum depth sampled in the same 58 profiles. Points correspond to horizon–level samples from 42 profiles studied within the same landscape as the 16 profiles of this study (colored lines). Points are color-coded to distinguish broad differences in mineral weathering status as a proxy for soil type (oxalate criterion for andic soils). Dashed line is the accumulation of mass for a constant mineral bulk density of 0.5 g cm^{-3}. See text for further explanation of estimation procedure, interpretation, and assumptions.

Chapter 5

Conclusion

The three studies in this dissertation embody an effort to quantify vegetation and soil properties and associated uncertainties in a landscape with overlapping biophysical and anthropogenic gradients. The specific phenomena of interest—seasonal vegetation dynamics in Chapter 2, soil organic carbon (SOC) storage in Chapters 3 and 4, and SOC turnover in Chapter 4—play key roles in the biogeochemical and hydrologic cycles that underlie ecosystem service provision. Seasonal vegetation dynamics govern terrestrial carbon uptake through photosynthesis (Guan et al., 2015) and mediate the hydrologic cycle through transpiration and interception (González-Martínez & Holwerda, 2018; López-Ramírez et al., 2021), while also influencing the cycling of foliar nutrients (Neumann et al., 2018). SOC storage not only reduces atmospheric CO_2 concentrations, but also directly enhances soil hydraulic properties (Yang et al., 2014) and the availability of nutrients (Johnson et al., 2003; Medorio-García et al., 2020) and contributes at least indirectly to myriad other soil biogeochemical processes (Kleber et al., 2021). SOC turnover is intricately tied to the rate of carbon inputs into the soil and the "permanence" of SOC storage (Sierra et al., 2017; Dynarski et al., 2020). Hence, reducing the uncertainties of estimates of phenology and SOC dynamics can improve the quantification of biophysical processes of immense societal importance. Quantifying the magnitude of those uncertainties is a critical prerequisite towards this goal.

The analyses of land-surface phenology in Chapter 2 revealed systematic variation in the seasonality of broadleaf canopies (cloud forest and oak-pine forest) across the study area. For example, forest patches with lower biodiversity and/or a greater proportion of deciduous species tended to green up faster in the spring. Furthermore, the start of the growing season within

broadleaf cover types was delayed with increasing elevation, but the rate of delay was not constant along the elevation gradient as is often assumed (Hopkins, 1918; Streher et al., 2017). Accounting for the uncertainty of phenological parameters reduced the magnitude of each of these trends while also bolstering confidence that the trends were real (i.e., 95% credible intervals for estimated trends excluded zero after accounting for parameter uncertainty). Large parameter uncertainties in other cover types indicated the need for further model refinement (e.g., flexible timing of minimum greenness). The most immediate utility of my findings of significant phenological variation within broadleaf cover types and of land cover-specific uncertainties may be in improving mapping of land-cover type and forest condition (e.g., using phenological parameters to differentiate sub-types of broadleaf cover and using parameter uncertainties to predict cover types other than broadleaf).

In Chapter 3, I found that SOC stocks in the study area were generally underestimated by statistical models developed at regional to global scales. Landscape-specific soils observations that were readily available in global soil databases were effective for correcting the overall bias of model predictions. Using data for a more pedologically comprehensive set of soil profiles highlighted a mid-elevation hotspot of SOC storage, suggesting that the local observations included in the global databases may not have sufficiently represented the pedologic variability present across the landscape. These results indicate that increased availability of local data will likely lead to more dramatic improvements in predictions than the gains obtained from refinement of covariates and/or model parameterization. Narrowing the substantial uncertainties of calibrated predictions in future work may be aided by extending the coregionalization approach (here used to jointly predict top- and subsoil SOC stocks) to leverage measurements of auxiliary soil properties that are correlated with SOC storage but more scalable (e.g., soil spectra).

The soil profile-level analyses in Chapter 4 underscored the sensitivity of SOC storage and turnover estimates to assumptions about how soil mass and/or volume have changed along gradients of disturbance and succession. These assumptions are implicit in the choice of depth(s) at which soil profiles are compared. Existing approaches to comparing SOC storage and turnover across profiles variously ignore potential changes in porosity (fixed-depth approach), organic matter (equivalent soil mass approach), and/or reactive mineral phases (equivalent mineral mass approach). In comparing existing approaches to estimating soil volume change with a novel approach that assumes the conservation a single minimally weatherable, rock-derived element (e.g., titanium [Ti] or zirconium [Zr]), I found that fixed-depth estimates overestimated SOC

stocks and imparted a negative bias to mean radiocarbon activity values compared to approaches that accounted for reductions in soil volume associated with deforestation and grazing. This profile-level discrepancy affected estimated differences in SOC stocks from earlier to later stages of forest succession, with only the fixed-depth approach suggesting a small but statistically insignificant decline in SOC stocks during succession. Lower radiocarbon activities under pastures and early successional stages—after accounting for possible negative biases imparted by soil volume changes—were consistent with slower SOC turnover rates compared to intermediate to mature forests. The mechanisms underlying this apparent difference are the focus of ongoing complementary studies, including radiocarbon dating of soil density fractions and multimodal characterization of soil organic matter composition across the study profiles. Considering the relatively small differences detected between SOC storage and radiocarbon activities as calculated on the basis of equivalent soil mineral mass or equivalent masses of Ti or Zr, the results of Chapter 4 support more widespread use of the equivalent mineral mass approach, which requires the same data as used in the calculation of SOC stocks, when land-use changes may have resulted in soil volume changes. Extending this framework to quantify the uncertainties of SOC stocks and radiocarbon activities stemming from uncertainties related to bulk density measurements and the choice of reference profiles remains a priority for future work.

While the roles of satellite imagery and globally extensive model-based products in socioecological research and sustainable resource management will undoubtedly grow in coming years, these three sets of analyses affirm the critical importance of field-based observations for relating these information sources to the spatial variation of vegetation and soil properties within individual landscapes. Strategic integration of these information sources across scales is key to generating actionable understanding of how anthropogenic factors affect ecosystem service provision across diverse biophysical contexts.

References

Adams, W. (1973). The effect of organic matter on true and bulk densities of some uncultivated podzolic soils. *Journal of Soil Science*, 24.

Adhikari, K., & Hartemink, A.E. (2016). Linking soils to ecosystem services — a global review. *Geoderma*, 262, 101–111. doi:10.1016/j.geoderma.2015.08.009.

Aguilar Orea, G.F. (2013). Variación de la repelencia al agua de los suelos en función de la profundidad, del contenido de humedad, de la posición topográfica y de la cobertura vegetal, en la cuenca del río Los Gavilanes, Veracruz. Master's thesis. Universidad Veracruzana. Xalapa, Veracruz, Mexico.

Alexander, E.B. (1982). Volume estimates of coarse fragments in soils: a combination of visual and weighing procedures. *Journal of Soil and Water Conservation*, 37, 62–63.

Alvarado-Barrientos, M., Holwerda, F., Asbjornsen, H., Dawson, T., & Bruijnzeel, L. (2014). Suppression of transpiration due to cloud immersion in a seasonally dry Mexican weeping pine plantation. *Agricultural and Forest Meteorology*, 186, 12–25. doi:10.1016/j.agrformet.2013.11.002.

Araujo-Carrillo, G.A., Varón-Ramirez, V.M., Gómez-Latorre, D.A., Estupiñan-Casallas, J.M., Rodríguez-Roa, A.O., Deantonio-Florido, L.Y., & Martínez-Maldonado, F.E. (2020). Mapping a hydrophysical soil property through a comparative analysis of local and global scale approximations. *Scientia Agricola*, 78, 1–7. doi:10.1590/1678-992x-2019-0126.

Araya, S., Lyle, G., Lewis, M., & Ostendorf, B. (2016). Phenologic metrics derived from MODIS NDVI as indicators for plant available water-holding capacity. *Ecological Indicators*, 60, 1263–1272. doi:10.1016/j.ecolind.2015.09.012.

Ariza, C., Maselli, D., & Kohler, T. (2013). Mountains: Our Life, Our Future. Progress and Perspectives on Sustainable Mountain Development from Rio 1992 to Rio 2012 and Beyond. Swiss Agency for Development and Cooperation (SDC), Centre for Development and Environment (CDE).

Asbjornsen, H., Manson, R.H., Scullion, J.J., Holwerda, F., Muñoz-Villers, L.E., Alvarado-Barrientos, M.S., Geissert, D., Dawson, T.E., McDonnell, J.J., & Adrian Bruijnzeel, L. (2017). Interactions between payments for hydrologic services, landowner decisions, and ecohydrological consequences: Synergies and disconnection in the cloud forest zone of central Veracruz, Mexico. *Ecology and Society*, 22. doi:10.5751/ES-09144-220225.

Babcock, C., Finley, A.O., Bradford, J.B., Kolka, R., Birdsey, R., & Ryan, M.G. (2015). Lidar

based prediction of forest biomass using hierarchical models with spatially varying coefficients. *Remote Sensing of Environment*, 169, 113–127. doi:10.1016/j.rse.2015.07.028.

Babcock, C., Finley, A.O., & Looker, N. (2021). A Bayesian model to estimate land surface phenology parameters with harmonized Landsat 8 and Sentinel-2 images. *Remote Sensing of Environment*, 261, 112471. doi:10.1016/j.rse.2021.112471.

Barradas, V.L., Cervantes-Pérez, J., Ramos-Palacios, R., Puchet-Anyul, C., Vázquez-Rodríguez, P., & Granados-Ramírez, R. (2010). Meso-scale climate change in the central mountain region of Veracruz State , Mexico. Cambridge University Press. p. 549–556. doi:10.1017/CBO9780511778384.058.

Basile-Doelsch, I., Brun, T., Borschneck, D., Masion, A., Marol, C., & Balesdent, J. (2009). Effect of landuse on organic matter stabilized in organomineral complexes: A study combining density fractionation, mineralogy and δ13C. *Geoderma*, 151, 77–86. doi:10.1016/j.geoderma.2009.03.008.

Bates, D., Mächler, M., Bolker, B., & Walker, S. (2015). Fitting linear mixed-effects models using lme4. *Journal of Statistical Software*, 67, 1–48. doi:10.18637/jss.v067.i01.

Batjes, N., Ribeiro, E., & van Oostrum, A. (2019). Standardised soil profile data to support global mapping and modelling (wosis snapshot 2019). *Earth System Science Data Discussions*, , 1–46doi:10.5194/essd-2019-164.

Batjes, N.H., Ribeiro, E., Van Oostrum, A., Leenaars, J., Hengl, T., & Mendes De Jesus, J. (2017). WoSIS: Providing standardised soil profile data for the world. *Earth System Science Data*, 9, 1–14. doi:10.5194/essd-9-1-2017.

Beck, H.E., Wood, E.F., McVicar, T.R., Zambrano-Bigiarini, M., Alvarez-Garreton, C., Baez-Villanueva, O.M., Sheffield, J., & Karger, D.N. (2020). Bias correction of global high-resolution precipitation climatologies using streamflow observations from 9372 catchments. *Journal of Climate*, 33, 1299–1315. doi:10.1175/JCLI-D-19-0332.1.

Bender, S.F., Wagg, C., & van der Heijden, M.G. (2016). An underground revolution: Biodiversity and soil ecological engineering for agricultural sustainability. *Trends in Ecology and Evolution*, 31, 440–452. doi:10.1016/j.tree.2016.02.016.

Berry, J.K., Delgado, J.A., Pierce, F.J., & Khosla, R. (2005). Applying spatial analysis for precision conservation across the landscape. *Journal of Soil and Water Conservation*, 60, 363–370.

Berry, Z.C., Jones, K.W., Gomez Aguilar, L.R., Congalton, R.G., Holwerda, F., Kolka, R., Looker, N., Lopez Ramirez, S.M., Manson, R., Mayer, A., Muñoz-Villers, L., Ortiz Colin, P., Romero-Uribe, H., Saenz, L., Von Thaden, J.J., Vizcaíno Bravo, M.Q., Williams-Linera, G., & Asbjornsen, H. (2020). Evaluating ecosystem service trade-offs along a land-use intensification gradient in central Veracruz, Mexico. *Ecosystem Services*, 45, 101181. URL: https://www.sciencedirect.com/science/article/pii/S2212041620301236, doi:https://doi.org/10.1016/j.ecoser.2020.101181.

de Beurs, K.M., & Henebry, G.M. (2010). Spatio-temporal statistical methods for modelling land surface phenology. Springer Netherlands, Dordrecht. pp. 177–208. URL: https://doi.org/10.1007/978-90-481-3335-2_9, doi:10.1007/978-90-481-3335-2$_9$.

Bishop, T.F., McBratney, A.B., & Laslett, G.M. (1999). Modeling soil attribute depth functions with equal-area quadratic smoothing splines. *Geoderma*, 91, 27–45. doi:10.1016/S0016-7061(99)00003-8.

Blake, G., & Kartge, K. (1986). Bulk density, in: Klute, A. (Ed.), Methods of soil analysis.. 2nd ed. ed.. American Society of Agronomy, Madison, Wis.. Methods of Soil Analysis: Part 1. Physical and mineralogical methods, pp. 363–381.

Boisvenue, C., & Running, S.W. (2010). Simulations show decreasing carbon stocks and potential for carbon emissions in rocky mountain forests over the next century. *Ecological applications : a publication of the Ecological Society of America*, 20, 1302–19.

Borchert, R., Robertson, K., Schwartz, M.D., & Williams-Linera, G. (2005). Phenology of temperate trees in tropical climates. *International Journal of Biometeorology*, 50, 57–65. doi:10.1007/s00484-005-0261-7.

Breiman, L. (2001). Random forests. *Machine Learning*, 45, 5–32. doi:10.1201/9780429469275-8.

Brimhall, G.H., & Dietrich, W.E. (1987). Constitutive mass balance relations between chemical composition, volume, density, porosity, and strain in metasomatic hydrochemical systems: Results on weathering and pedogenesis. *Geochimica et Cosmochimica Acta*, 51, 567–587. doi:10.1016/0016-7037(87)90070-6.

Cade, B.S., & Noon, B.R. (2003). A gentle introduction to quantile regression for ecologists. *Frontiers in Ecology and the Environment*, 1, 412–420. doi:10.1890/1540-9295(2003)001[0412:AGITQR]2.0.CO;2.

Campos C., A. (2006). Response of soil surface CO_2-C flux to land use changes in a tropical cloud forest (Mexico). *Forest Ecology and Management*, 234, 305–312. doi:10.1016/j.foreco.2006.07.012.

Campos C., A., Aguilar S., G., & Landgrave, R. (2014). Soil organic carbon stocks in Veracruz state (Mexico) estimated using the 1:250,000 soil database of inegi: biophysical contributions. *Journal of Soils and Sediments*, , 1–12doi:10.1007/s11368-014-0851-2.

Campos C., A., Oleschko L., K., Etchevers B., J., & Hidalgo M., C. (2007). Exploring the effect of changes in land use on soil quality on the eastern slope of the Cofre de Perote volcano (Mexico). *Forest Ecology and Management*, 248, 174–182. doi:10.1016/j.foreco.2007.05.004.

Cantagrel, J.M., & Robin, C. (1979). K-ar dating on eastern Mexican volcanic rocks – relations between the andesitic and the alkaline provinces. *J. Volcanol. Geotherm. Res.*, 5, 99–114.

Carlson, C.J., Kracalik, I.T., Ross, N., Alexander, K.A., Hugh-Jones, M.E., Fegan, M., Elkin, B.T., Epp, T., Shury, T.K., Zhang, W., & et al. (2019). The global distribution of bacillus anthracis and associated anthrax risk to humans, livestock and wildlife. *Nature Microbiology*, 4, 1337–1343. doi:10.1038/s41564-019-0435-4.

Carrasco-Núñez, G., Siebert, L., Díaz-Castellón, R., Vázquez-Selem, L., & Capra, L. (2010). Evolution and hazards of a long-quiescent compound shield-like volcano: Cofre de Perote, eastern trans-Mexican volcanic belt. *Journal of Volcanology and Geothermal Research*, 197, 209–224. doi:10.1016/j.jvolgeores.2009.08.010.

Chadwick, O.A., Brimhall, G.H., & Hendricks, D.M. (1990). From a black to a gray box - a

mass balance interpretation of pedogenesis. *Geomorphology*, 3, 369–390. doi:10.1016/0169-555X(90)90012-F.

Chapin, F.S., Woodwell, G.M., Randerson, J.T., Rastetter, E.B., Lovett, G.M., Baldocchi, D.D., Clark, D.a., Harmon, M.E., Schimel, D.S., Valentini, R., & et al. (2006). Reconciling carbon-cycle concepts, terminology, and methods. *Ecosystems*, 9, 1041–1050. doi:10.1007/s10021-005-0105-7.

Chaplot, V., Podwojewski, P., Phachomphon, K., & Valentin, C. (2009). Soil erosion impact on soil organic carbon spatial variability on steep tropical slopes. *Soil Science Society of America Journal*, 73, 769–779. doi:10.2136/sssaj2008.0031.

Chappell, A., Webb, N.P., Leys, J.F., Waters, C.M., Orgill, S., & Eyres, M.J. (2019). Minimising soil organic carbon erosion by wind is critical for land degradation neutrality. *Environmental Science and Policy*, 93, 43–52. doi:10.1016/j.envsci.2018.12.020.

Chartres, C.J., & Pain, C.F. (1984). A climosequence of soils on late quaternary volcanic ash in highland Papua New Guinea. *Geoderma*, 32, 131–155. doi:10.1016/0016-7061(84)90068-5.

Chen, S., Mulder, V.L., Heuvelink, G.B., Poggio, L., Caubet, M., Román Dobarco, M., Walter, C., & Arrouays, D. (2020). Model averaging for mapping topsoil organic carbon in france. *Geoderma*, 366, 114237. doi:10.1016/j.geoderma.2020.114237.

Chevallier, T., Fujisaki, K., Roupsard, O., Guidat, F., Kinoshita, R., De Melo Viginio Filho, E., Lehner, P., & Albrecht, A. (2019). Short-range-order minerals as powerful factors explaining deep soil organic carbon stock distribution: The case of a coffee agroforestry plantation on Andosols in Costa Rica. *Soil*, 5, 315–332. doi:10.5194/soil-5-315-2019.

Chevallier, T., Woignier, T., Toucet, J., & Blanchart, E. (2010). Organic carbon stabilization in the fractal pore structure of Andosols. *Geoderma*, 159, 182–188. doi:10.1016/j.geoderma.2010.07.010.

Churkina, G., Schimel, D., Braswell, B.H., & Xiao, X. (2005). Spatial analysis of growing season length control over net ecosystem exchange. *Global Change Biology*, 11, 1777–1787. URL: https://onlinelibrary.wiley.com/doi/abs/10.1111/j.1365-2486.2005.001012.x, doi:10.1111/j.1365-2486.2005.001012.x, arXiv:https://onlinelibrary.wiley.com/doi/pdf/10.1111/j.1365-2486.2005.001012.x.

Clewley, D., Bunting, P., Shepherd, J., Gillingham, S., Flood, N., Dymond, J., Lucas, R., Armston, J., & Moghaddam, M. (2014). A Python-based open source system for Geographic Object-Based Image Analysis (GEOBIA) utilizing raster attribute tables. *Remote Sensing*, 6, 6111–6135. doi:10.3390/rs6076111.

Concha-Dimas, A., Cerca, M., Rodríguez, S.R., & Watters, R.J. (2005). Geomorphological evidence of the influence of pre-volcanic basement structure on emplacement and deformation of volcanic edifices at the Cofre de Perote-Pico de Orizaba chain and implications for avalanche generation. *Geomorphology*, 72, 19–39. doi:10.1016/j.geomorph.2005.05.004.

Cong, N., Wang, T., Nan, H., Ma, Y., Wang, X., Myneni, R.B., & Piao, S. (2013). Changes in satellite-derived spring vegetation green-up date and its linkage to climate in China

from 1982 to 2010: A multimethod analysis. *Global Change Biology*, 19, 881–891. doi:10.1111/gcb.12077.

Cribari-Neto, F., & Zeileis, A. (2010). Beta Regression in R. *Journal of Statistical Software, Articles*, 34, 1–24. URL: https://www.jstatsoft.org/v034/i02, doi:10.18637/jss.v034.i02.

Crossman, N.D., & Bryan, B.A. (2009). Identifying cost-effective hotspots for restoring natural capital and enhancing landscape multifunctionality. *Ecological Economics*, 68, 654–668. doi:10.1016/j.ecolecon.2008.05.003.

Crow, S.E., Reeves, M., Turn, S., Taniguchi, S., Schubert, O.S., & Koch, N. (2016). Carbon balance implications of land use change from pasture to managed eucalyptus forest in Hawaii. *Carbon Management*, 7, 171–181. doi:10.1080/17583004.2016.1213140.

Cuni-Sanchez, A., Sullivan, M., Platts, P., & et al. (2021). High above-ground carbon stock of African tropical montane forests. *Nature*, 596, 536–542. doi:10.1038/s41586-021-03728-4.

Dahlgren, R.A., Boettinger, J.L., Huntington, G.L., & Amundson, R. (1997). Soil development along an elevational transects in the western Sierra Nevada, California. *Geoderma*, 78, 207–236. doi:10.1016/S0016-7061(97)00034-7.

Dai, Y., Xin, Q., Wei, N., Zhang, Y., Shangguan, W., Yuan, H., Zhang, S., Liu, S., & Lu, X. (2019). A global high-resolution data set of soil hydraulic and thermal properties for land surface modeling. *Journal of Advances in Modeling Earth Systems*, 11, 2996–3023. doi:10.1029/2019MS001784.

Davidson, E.A., & Ackerman, I.L. (1993). Changes in soil carbon inventories following cultivation of previously untilled soils. *Biogeochemistry*, 20, 161–193. doi:10.1007/BF00000786.

De Vos, B., Van Meirvenne, M., Quataert, P., Deckers, J., & Muys, B. (2005). Predictive quality of pedotransfer functions for estimating bulk density of forest soils. *Soil Science Society of America Journal*, 69, 500–510. doi:10.2136/sssaj2005.0500.

Demattê, J.A., Safanelli, J.L., Poppiel, R.R., Rizzo, R., Silvero, N.E.Q., Mendes, W.d.S., Bonfatti, B.R., Dotto, A.C., Salazar, D.F.U., Mello, F.A.d.O., & et al. (2020). Bare earth's surface spectra as a proxy for soil resource monitoring. *Scientific Reports*, 10, 1–11. doi:10.1038/s41598-020-61408-1.

Deng, L., Zhu, G.y., Tang, Z.s., & Shangguan, Z.p. (2016). Global patterns of the effects of land-use changes on soil carbon stocks. *Global Ecology and Conservation*, 5, 127–138. doi:10.1016/j.gecco.2015.12.004.

Dinerstein, E., Vynne, C., Sala, E., Joshi, A.R., Fernando, S., Lovejoy, T.E., Mayorga, J., Olson, D., Asner, G.P., Baillie, J.E., & et al. (2019). A global deal for nature: Guiding principles, milestones, and targets. *Science Advances*, 5, 1–18. doi:10.1126/sciadv.aaw2869.

Dixon, J.L., Heimsath, A.M., & Amundson, R. (2009). The critical role of climate and saprolite weathering in landscape evolution. *Earth Surface Processes and Landforms*, 34, 1507–1521. doi:10.1002/esp.1836.

Djukic, I., Zehetner, F., Tatzber, M., & Gerzabek, M.H. (2010). Soil organic-matter stocks and characteristics along an alpine elevation gradient. *Journal of Plant Nutrition and Soil Science*, 173, 30–38. doi:10.1002/jpln.200900027.

Doetterl, S., Berhe, A.A., Nadeu, E., Wang, Z., Sommer, M., & Fiener, P. (2016). Erosion,

deposition and soil carbon: A review of process-level controls, experimental tools and models to address C cycling in dynamic landscapes. *Earth-Science Reviews*, 154, 102–122. doi:10.1016/j.earscirev.2015.12.005.

Dominati, E., Patterson, M., & Mackay, A. (2010). A framework for classifying and quantifying the natural capital and ecosystem services of soils. *Ecological Economics*, 69, 1858–1868. doi:10.1016/j.ecolecon.2010.05.002.

Don, A., Schumacher, J., & Freibauer, A. (2011). Impact of tropical land-use change on soil organic carbon stocks - a meta-analysis. *Global Change Biology*, 17, 1658–1670. doi:10.1111/j.1365-2486.2010.02336.x.

Duarte-Guardia, S., Peri, P.L., Amelung, W., Sheil, D., Laffan, S.W., Borchard, N., Bird, M.I., Dieleman, W., Pepper, D.A., Zutta, B., & et al. (2019). Better estimates of soil carbon from geographical data: a revised global approach. *Mitigation and Adaptation Strategies for Global Change*, 24, 355–372. doi:10.1007/s11027-018-9815-y.

Dubroeucq, D., Geissert, D., Moreno, P., & Millot, G. (1992). Soil evolution and plant communities in coastal dunes near Veracruz, Mexico. *Cahiers - ORSTOM, Serie Pedologie*, 27, 237–250.

Dubroeucq, D., Geissert, D., & Quantin, P. (1998). Weathering and soil forming processes under semi-arid conditions in two Mexican volcanic ash soils. *Geoderma*, 86, 99–122. doi:10.1016/S0016-7061(98)00033-0.

Dynarski, K.A., Bossio, D.A., & Scow, K.M. (2020). Dynamic stability of soil carbon: Reassessing the "permanence" of soil carbon sequestration. *Frontiers in Environmental Science*, 8, 218. URL: https://www.frontiersin.org/article/10.3389/fenvs.2020.514701, doi:10.3389/fenvs.2020.514701.

Díaz-Castellón, R., Hubbard, B.E., Carrasco-Núñez, G., & Rodríguez-Vargas, J.L. (2012). The origins of late quaternary debris avalanche and debris flow deposits from Cofre de Perote volcano, méxico. *Geosphere*, 8, 950–971. doi:10.1130/GES00709.1.

Dümig, A., Schad, P., Kohok, M., Beyerlein, P., Schwimmer, W., & Kögel-Knabner, I. (2008). A mosaic of nonallophanic Andosols, Umbrisols and Cambisols on rhyodacite in the southern Brazilian highlands. *Geoderma*, 145, 158–173. doi:10.1016/j.geoderma.2008.01.013.

Eekhout, J.P., Hunink, J.E., Terink, W., & De Vente, J. (2018). Why increased extreme precipitation under climate change negatively affects water security. *Hydrology and Earth System Sciences*, 22, 5935–5946. doi:10.5194/hess-22-5935-2018.

Egli, M., Mirabella, A., Sartori, G., & Fitze, P. (2003). Weathering rates as a function of climate: Results from a climosequence of the val genova (trentino, italian alps). *Geoderma*, 111, 99–121. doi:10.1016/S0016-7061(02)00256-2.

Egli, M., Mirabella, A., Sartori, G., Zanelli, R., & Bischof, S. (2006). Effect of north and south exposure on weathering rates and clay mineral formation in alpine soils. *Catena*, 67, 155–174. doi:10.1016/j.catena.2006.02.010.

Eilers, P.H., & Marx, B.D. (1996). Flexible smoothing with B-splines and penalties. *Statistical Science*, 11, 89–102. doi:10.1214/ss/1038425655.

Ellert, B.H., & Bettany, J.R. (1995). Calculation of organic matter and nutrients stored in soils

under contrasting management regimes. *Canadian Journal of Soil Science*, 75, 529–538. doi:10.4141/cjss95-075.

Elmore, A.J., Guinn, S.M., Minsley, B.J., & Richardson, A.D. (2012). Landscape controls on the timing of spring, autumn, and growing season length in mid-Atlantic forests. *Global Change Biology*, 18, 656–674. doi:10.1111/j.1365-2486.2011.02521.x.

FAO, & ITPS (2020). Global soil organic carbon map v1.5: Technical report, .

FAO/IIASA/ISRIC/ISSCAS/JRC (2012). Harmonized world soil database (version 1.2), .

Fasiolo, M., Goude, Y., Nedellec, R., & Wood, S.N. (2017). Fast calibrated additive quantile regression. URL: https://arxiv.org/abs/1707.03307.

Fehse, J., Hofstede, R., Aguirre, N., Paladines, C., Kooijman, A., & Sevink, J. (2002). High altitude tropical secondary forests: A competitive carbon sink? *Forest Ecology and Management*, 163, 9–25. doi:10.1016/S0378-1127(01)00535-7.

Fick, S.E., & Hijmans, R.J. (2017). Worldclim 2: new 1-km spatial resolution climate surfaces for global land areas. *International Journal of Climatology*, 37, 4302–4315. doi:10.1002/joc.5086.

Fieldes, M., & Claridge, G.G.C. (1975). Allophane. Springer Berlin Heidelberg, Berlin, Heidelberg. pp. 351–393. URL: https://doi.org/10.1007/978-3-642-65917-1_10, doi:10.1007/978-3-642-65917-$1_1$0.

Finley, A., & Babcock, C. (2020). rsBayes: Bayesian Models for Remotely Sensed Data. R package version 0.1.0.

Finley, A.O., & Banerjee, S. (2020). Bayesian spatially varying coefficient models in the spBayes R package. *Environmental Modelling Software*, 125, 104608. URL: http://www.sciencedirect.com/science/article/pii/S1364815219310412, doi:https://doi.org/10.1016/j.envsoft.2019.104608.

Finley, A.O., Banerjee, S., & Gelfand, A.E. (2015). spBayes for large univariate and multivariate point-referenced spatio-temporal data models. *Journal of Statistical Software, Articles*, 63, 1–28. URL: https://www.jstatsoft.org/v063/i13, doi:10.18637/jss.v063.i13.

Finstad, K., van Straaten, O., Veldkamp, E., & McFarlane, K. (2020). Soil carbon dynamics following land use changes and conversion to oil palm plantations in tropical lowlands inferred from radiocarbon. *Global Biogeochemical Cycles*, 34. doi:10.1029/2019GB006461.

Fisher, J.I., Mustard, J.F., & Vadeboncoeur, M.A. (2006). Green leaf phenology at Landsat resolution: Scaling from the field to the satellite. *Remote Sensing of Environment*, 100, 265–279. doi:10.1016/j.rse.2005.10.022.

Fitz Bravo, César and Ramírez Tello Enrique (2007). Informe geológico minero y geoquímico carta Xalapa E14-B27, escala 1:50,000, estado de Veracruz. Technical Report. Servicio Geológico Mexicano. Hidalgo, México.

Flint, A.L., & Flint, L.E. (2002). 2.2 Particle Density. John Wiley Sons, Ltd. pp. 229–240. URL: https://acsess.onlinelibrary.wiley.com/doi/abs/10.2136/sssabookser5.4.c10, doi:https://doi.org/10.2136/sssabookser5.4.c10, arXiv:https://acsess.onlinelibrary.wiley.com/doi/pdf/10.2136/sssabookser5.4.c10.

Fois, M., Cuena-Lombraña, A., Fenu, G., & Bacchetta, G. (2018). Using species distribution models at local scale to guide the search of poorly known species: Review, methodological issues and future directions. *Ecological Modelling*, 385, 124–132. doi:10.1016/j.ecolmodel.2018.07.018.

Fraval, S., Hammond, J., Lannerstad, M., Oosting, S.J., Sayula, G., Teufel, N., Silvestri, S., Poole, E.J., Herrero, M., & van Wijk, M.T. (2018). Livelihoods and food security in an urban linked, high potential region of tanzania: Changes over a three year period. *Agricultural Systems*, 160, 87–95. doi:10.1016/j.agsy.2017.10.013.

von Fromm, S., Hoyt, A., Acquah, G., Aynekulu, E., Berhe, A.A., Haefele, S., Lange, M., McGrath, S., Shepherd, K., Sila, A., & et al. (2020). Continental-scale controls on soil organic carbon across sub-Saharan Africa. *SOIL Discussions*, , 1–39doi:10.5194/soil-2020-69.

Galvão, L.S., Breunig, F.M., Teles, T.S., Gaida, W., & Balbinot, R. (2016). Investigation of terrain illumination effects on vegetation indices and VI-derived phenological metrics in subtropical deciduous forests. *GIScience and Remote Sensing*, 53, 360–381. URL: http://dx.doi.org/10.1080/15481603.2015.1134140, doi:10.1080/15481603.2015.1134140.

Gamboa, A.M., & Galicia, L. (2012). Land-use/cover change effects and carbon controls on volcanic soil profiles in highland temperate forests. *Geoderma*, 170, 390–402. doi:10.1016/j.geoderma.2011.11.021.

García Calderón, N.E., Ibáñez Huerta, A., Alvarez Arteaga, G., Krasilnikov, P.V., & Hernández Jiménez, A. (2006). Soil diversity and properties in mountainous subtropical areas, in sierra sur de oaxaca, Mexico. *Canadian Journal of Soil Science*, 86, 61–76. doi:10.4141/S04-070.

García-Rodeja, E., Nóvoa, J.C., Pontevedra, X., Martínez-Cortizas, A., & Buurman, P. (2004). Aluminium and iron fractionation of European volcanic soils by selective dissolution techniques. *Catena*, 56, 155–183. doi:10.1007/978-3-540-48711-$1_2$5.

GDAL/OGR contributors (2020). GDAL/OGR Geospatial Data Abstraction software Library. Open Source Geospatial Foundation. URL: https://gdal.org.

Geissert, D., Campos C., A., Meza Pérez, E., Cruz Huerta, M.L., Arteaga, C., Portilla, N., Dubroeucq, D., & Quantin, P. (1994). Cartografía, génesis y restricciones al uso de los suelos de origen volcánico de la región natural Cofre de Perote, Veracruz, México. CONACyT project no. 0796-N9110. Final report. Technical Report.

Geissert, D., Gómez-Tagle Chávez, A., Martínez Hernández, L., Meza Pérez, E., & Enríquez Fernández, E. (2013). Cartografía del suelo para la identificación de unidades hidroedáficas funcionales en una cuenca de montaña : Conceptos y propuesta metodológica, in: Memorias del Tercer Congreso Nacional de Manejo de Cuencas Hidrográficas, Universidad Nacional Autónoma de México Centro de Investigaciones en Geografía Ambiental Antigua. p. 3–11.

Gelman, A., Rubin, D., Carlin, J., & Stern, H. (1995). Bayesian Data Analysis. 1 ed., Chapman and Hall/CRC. doi:10.1201/9780429258411.

Gifford, R.M., & Roderick, M.L. (2003). Soil carbon stocks and bulk density: Spatial or cumulative mass coordinates as a basis of expression? *Global Change Biology*, 9, 1507–1514. doi:10.1046/j.1365-2486.2003.00677.x.

Goldsmith, G.R., Muñoz-Villers, L.E., Holwerda, F., Mcdonnell, J.J., Asbjornsen, H., & Dawson, T.E. (2012). Stable isotopes reveal linkages among ecohydrological processes in a seasonally dry tropical montane cloud forest. *Ecohydrology*, 5, 779–790. doi:10.1002/eco.268.

González-Martínez, T.M., & Holwerda, F. (2018). Rainfall and fog interception at the lower and upper altitudinal limits of cloud forest in Veracruz, Mexico. *Hydrological Processes*, 32, 3717–3728. doi:10.1002/hyp.13299.

GRASS Development Team (2018). Geographic Resources Analysis Support System (GRASS GIS) Software. Open Source Geospatial Foundation. USA. URL: https://grass.osgeo.org.

Green, E.G., Dietrich, W.E., & Banfield, J.F. (2006). Quantification of chemical weathering rates across an actively eroding hillslope. *Earth and Planetary Science Letters*, 242, 155–169. doi:10.1016/j.epsl.2005.11.039.

Griscom, B.W., Adams, J., Ellis, P.W., Houghton, R.A., Lomax, G., Miteva, D.A., Schlesinger, W.H., Shoch, D., Siikamäki, J.V., Smith, P., & et al. (2017). Natural climate solutions. *Proceedings of the National Academy of Sciences of the United States of America*, 114, 11645–11650. doi:10.1073/pnas.1710465114.

Grunwald, S. (2005). What do we really know about the space-time continuum of soil-landscapes?, in: Grunwald, S. (Ed.), Environmental Soil-Landscape Modeling: Geographic Information Technologies and Pedometrics, p. 3–36. doi:10.1201/9781420028188.sec1.

Guan, K., Pan, M., Li, H., Wolf, A., Wu, J., Medvigy, D., Caylor, K.K., Sheffield, J., Wood, E.F., Malhi, Y., Liang, M., Kimball, J.S., Saleska, S.R., Berry, J., Joiner, J., & Lyapustin, A.I. (2015). Photosynthetic seasonality of global tropical forests constrained by hydroclimate. *Nature Geoscience*, 8, 284–289. doi:10.1038/ngeo2382.

Guan, K., Wood, E.F., Medvigy, D., Kimball, J., Pan, M., Caylor, K.K., Sheffield, J., Xu, X., & Jones, M.O. (2014). Terrestrial hydrological controls on land surface phenology of African savannas and woodlands. *Journal of Geophysical Research G: Biogeosciences*, 119, 1652–1669. doi:10.1002/2013JG002572.

Guenet, B., Camino-Serrano, M., Ciais, P., Tifafi, M., Maignan, F., Soong, J.L., & Janssens, I.A. (2018). Impact of priming on global soil carbon stocks. *Global Change Biology*, 24, 1873–1883. doi:10.1111/gcb.14069.

Guevara, M., Arroyo, C., Brunsell, N., Cruz, C.O., Domke, G., Equihua, J., Etchevers, J., Hayes, D., Hengl, T., Ibelles, A., & et al. (2020). Soil organic carbon across Mexico and the conterminous United States (1991–2010). *Global Biogeochemical Cycles*, 34, 21. doi:10.1029/2019GB006219.

Guevara, M., & Vargas, R. (2020). Soil organic carbon estimates and uncertainty at 1-m depth across Mexico, 1999-2009.

von Haden, A.C., Yang, W.H., & DeLucia, E.H. (2020). Soils' dirty little secret: Depth-based comparisons can be inadequate for quantifying changes in soil organic carbon and other mineral soil properties. *Global Change Biology*, 26, 3759–3770. doi:10.1111/gcb.15124.

Hanesch, M., & Scholger, R. (2002). Mapping of heavy metal loadings in soils by means of magnetic susceptibility measurements. *Environmental Geology*, 42, 857–870. doi:10.1007/s00254-002-0604-1.

Hartmann, J., & Moosdorf, N. (2012). The new global lithological map database glim: A representation of rock properties at the earth surface. *Geochemistry, Geophysics, Geosystems*, 13, 1–37. doi:10.1029/2012GC004370.

Hashimoto, S., Wattenbach, M., & Smith, P. (2011). Litter carbon inputs to the mineral soil of Japanese Brown forest soils: Comparing estimates from the RothC model with estimates from MODIS. *Journal of Forest Research*, 16, 16–25. doi:10.1007/s10310-010-0209-6.

Heckman, K., & Rasmussen, C. (2011). Lithologic controls on regolith weathering and mass flux in forested ecosystems of the southwestern USA. *Geoderma*, 164, 99–111. doi:10.1016/j.geoderma.2011.05.003.

Heckman, K.A., Nave, L.E., Bowman, M., Gallo, A., Hatten, J.A., Matosziuk, L.M., Possinger, A.R., SanClements, M., Strahm, B.D., Weiglein, T.L., & et al. (2020). Divergent controls on carbon concentration and persistence between forests and grasslands of the conterminous US. *Biogeochemistry*, 0123456789. doi:10.1007/s10533-020-00725-z.

Hengl, T. (2020). GSIF: Global Soil Information Facilities. URL: https://CRAN.R-project.org/package=GSIF. r package version 0.5-5.1.

Hengl, T., De Jesus, J.M., Heuvelink, G.B., Gonzalez, M.R., Kilibarda, M., Blagotić, A., Shangguan, W., Wright, M.N., Geng, X., Bauer-Marschallinger, B., & et al. (2017). Soilgrids250m: Global gridded soil information based on machine learning. *PLoS ONE*, 12, 1–40. doi:10.1371/journal.pone.0169748.

Hengl, T., De Jesus, J.M., MacMillan, R.A., Batjes, N.H., Heuvelink, G.B., Ribeiro, E., Samuel-Rosa, A., Kempen, B., Leenaars, J.G., Walsh, M.G., & et al. (2014). Soilgrids1km - global soil information based on automated mapping. *PLoS ONE*, 9. doi:10.1371/journal.pone.0105992.

Hengl, T., Heuvelink, G., & MacMillan, R. (2019). Statistical theory for predictive soil mapping, in: Hengl, T., & MacMillan, R. (Eds.), Predictive Soil Mapping with R.

Hengl, T., Miller, M., Krizan, J., Shepherd, K., Sila, A., Kilibarda, M., Antonijevic, O., Luka Glusica, Achim Dobermann, S.H., McGrath, S., Gifty Acquah, J.C., Parente, L., Sheykhmousa, M., Saito, K., Johnson, J.M., Chamberlin, J., Silatsa, F., Yemefack, M., MacMillan, R., Wheeler, I., & Crouch, J. (2021). African Soil Properties and Nutrients Mapped at 30 – m Spatial Resolution using Two-scale Ensemble Machine Learning. *Scientific Reports*, 11. doi:10.1038/s41598-021-85639-y.

Henry, A., Mabit, L., Jaramillo, R.E., Cartagena, Y., & Lynch, J.P. (2013). Land use effects on erosion and carbon storage of the Río Chimbo watershed, Ecuador. *Plant and Soil*, 367, 477–491. doi:10.1007/s11104-012-1478-y.

Hernández, C.M., Zaragoza, C.G., Iriarte-Vivar, S., Flores-Verdugo, F.J., & Casasola, P.M. (2011). Forest structure, productivity and species phenology of mangroves in the La Mancha lagoon in the Atlantic coast of Mexico. *Wetlands Ecology and Management*, 19, 273–293. doi:10.1007/s11273-011-9216-4.

Hiederer, R., & Köchy, M. (2011). Global soil organic carbon estimates and the harmonized world soil database. doi:10.2788/13267.

Hoffmann, O. (1989). De los hacendados a los forestales: manejo del espacio, dominación y explotación del bosque en la sierra madre oriental (Cofre de Perote). *Trace*, , 31–49.

Holwerda, F., Bruijnzeel, L., Muñoz-Villers, L., Equihua, M., & Asbjornsen, H. (2010). Rainfall and cloud water interception in mature and secondary lower montane cloud forests of central Veracruz, Mexico. *Journal of Hydrology*, 384, 84–96. URL: http://linkinghub.elsevier.com/retrieve/pii/S0022169410000351, doi:10.1016/j.jhydrol.2010.01.012.

Hopkins, A. (1918). Periodical events and natural law as guides to agricultural research and practice. *Monthly Weather Review*, Supplement 9, 1–42.

Hoyos, N., & Comerford, N.B. (2005). Land use and landscape effects on aggregate stability and total carbon of Andisols from the Colombian Andes. *Geoderma*, 129, 268–278. doi:10.1016/j.geoderma.2005.01.002.

Hudson Dunn, A., & de Beurs, K.M. (2011). Land surface phenology of North American mountain environments using moderate resolution imaging spectroradiometer data. *Remote Sensing of Environment*, 115, 1220–1233. URL: http://dx.doi.org/10.1016/j.rse.2011.01.005, doi:10.1016/j.rse.2011.01.005.

Huete, A., Didan, K., Miura, T., Rodriguez, E.P., Gao, X., & Ferreira, L.G. (2002). Overview of the radiometric and biophysical performance of the MODIS vegetation indices. *Remote Sensing of Environment*, 83, 195–213. doi:10.1016/S0034-4257(02)00096-2.

Huete, A., Liu, H., Batchily, K., & [van Leeuwen], W. (1997). A comparison of vegetation indices over a global set of tm images for eos-modis. *Remote Sensing of Environment*, 59, 440 – 451. URL: http://www.sciencedirect.com/science/article/pii/S0034425796001125, doi:https://doi.org/10.1016/S0034-4257(96)00112-5.

Hwang, T., Band, L.E., Miniat, C.F., Song, C., Bolstad, P.V., Vose, J.M., & Love, J.P. (2014). Divergent phenological response to hydroclimate variability in forested mountain watersheds. *Global Change Biology*, 20, 2580–2595. doi:10.1111/gcb.12556.

Inagaki, T.M., Possinger, A.R., Grant, K.E., Schweizer, S.A., Mueller, C.W., Derry, L.A., Lehmann, J., & Kögel-Knabner, I. (2020). Subsoil organo-mineral associations under contrasting climate conditions. *Geochimica et Cosmochimica Acta*, 270, 244–263. doi:10.1016/j.gca.2019.11.030.

INEGI (1984). Conjunto de datos vectoriales geológicos serie i. Veracruz. escala 1:250,000. Available at https://www.inegi.org.mx/app/biblioteca/ficha.html?upc=702825674601/ (2018-05-18).

INEGI (2004). Conjunto de Datos Edafológicos Alfanuméricos Escala 1:250,000 Serie I, Continuo Nacional. Available at https://www.inegi.org.mx/app/biblioteca/ficha.html?upc=702825266691 (2020-08-01).

INEGI (2013a). Conjunto de datos de Perfiles de suelos. Escala 1:250 000. Serie II. Continuo Nacional. Available at https://www.inegi.org.mx/app/biblioteca/ficha.html?upc=702825266707/ (2015-09-15).

INEGI (2013b). Continuo de elevaciones Mexicano 3.0. Available at https://www.inegi.org.mx/app/geo2/elevacionesmex/ (2015-10-1).

Jenkinson, D.S. (1971). The Accumulation of Organic Matter in Soil Left Uncultivated. Lawes Agricultural Trust. p. 113–137.

Jiang, Y., Luo, C., Zhang, D., Ostle, N.J., Cheng, Z., Ding, P., Shen, C., & Zhang, G. (2020). Radiocarbon evidence of the impact of forest-to-plantation conversion on soil organic carbon dynamics on a tropical island. *Geoderma*, 375, 114484. doi:10.1016/j.geoderma.2020.114484.

Johnson, A.H., Frizano, J., & Vann, D.R. (2003). Biogeochemical implications of labile phosphorus in forest soils determined by the Hedley fractionation procedure. *Oecologia*, 135, 487–499. doi:10.1007/s00442-002-1164-5.

Karger, D.N., Conrad, O., Böhner, J., Kawohl, T., Kreft, H., Soria-Auza, R.W., Zimmermann, N.E., Linder, H.P., & Kessler, M. (2017). Climatologies at high resolution for the earth's land surface areas. *Scientific Data*, 4, 1–20. doi:10.1038/sdata.2017.122.

Kaup, B.S., & Carter, B.J. (1987). Determining Ti source and distribution within a Paleustalf by micromorphology, submicroscopy and elemental analysis. *Geoderma*, 40, 141–156. doi:10.1016/0016-7061(87)90019-X.

Kearney, M.R., & Maino, J.L. (2018). Can next-generation soil data products improve soil moisture modelling at the continental scale? An assessment using a new microclimate package for the R programming environment. *Journal of Hydrology*, 561, 662–673. doi:10.1016/j.jhydrol.2018.04.040.

Keesstra, S., Mol, G., de Leeuw, J., Okx, J., Molenaar, C., de Cleen, M., & Visser, S. (2018). Soil-related sustainable development goals: Four concepts to make land degradation neutrality and restoration work. *Land*, 7. doi:10.3390/land7040133.

Kleber, M., Bourg, I.C., Coward, E.K., Hansel, C.M., Myneni, S.C.B., & Nunan, N. (2021). Dynamic interactions at the mineral–organic matter interface. *Nature Reviews Earth Environment*, 2, 402–421. URL: http://dx.doi.org/10.1038/s43017-021-00162-y, doi:10.1038/s43017-021-00162-y.

Körner, C. (2007). The use of "altitude" in ecological research. *Trends in Ecology and Evolution*, 22, 569–574. doi:10.1016/j.tree.2007.09.006.

Kramer, M.G., & Chadwick, O.A. (2018). Climate-driven thresholds in reactive mineral retention of soil carbon at the global scale. *Nature Climate Change*, 8, 1104–1108. doi:10.1038/s41558-018-0341-4.

Krpec, P., Horáček, M., & Šarapatka, B. (2020). A comparison of the use of local legacy soil data and global datasets for hydrological modelling a small-scale watersheds: Implications for nitrate loading estimation. *Geoderma*, 377. doi:10.1016/j.geoderma.2020.114575.

Kuriakose, S.L., Devkota, S., Rossiter, D.G., & Jetten, V.G. (2009). Prediction of soil depth using environmental variables in an anthropogenic landscape, a case study in the Western Ghats of Kerala, India. *Catena*, 79, 27–38. doi:10.1016/j.catena.2009.05.005.

Kurtz, A.C., Derry, L.A., Chadwick, O.A., & Alfano, M.J. (2000). Refractory element mobility in volcanic soils. *Geology*, 28, 683–686. doi:10.1130/0091-7613(2000)028<0683:REMIVS>2.3.CO;2.

Körner, C., Jetz, W., Paulsen, J., Payne, D., Rudmann-Maurer, K., & M. Spehn, E. (2017). A global inventory of mountains for bio-geographical applications. *Alpine Botany*, 127, 1–15. doi:10.1007/s00035-016-0182-6.

Lamichhane, S., Kumar, L., & Wilson, B. (2019). Digital soil mapping algorithms and covariates for soil organic carbon mapping and their implications: A review. *Geoderma*, 352, 395–413. doi:10.1016/j.geoderma.2019.05.031.

Lapenis, A.G., Lawrence, G.B., Buyantuev, A., Jiang, S., Sullivan, T.J., McDonnell, T.C., & Bailey, S. (2017). A Newly Identified Role of the Deciduous Forest Floor in the Timing of Green-Up. *Journal of Geophysical Research: Biogeosciences*, 122, 2876–2891. doi:10.1002/2017JG004073.

Lauer, W. (1973). The Altitudinal Belts Of The Vegetation In The Central Mexican Highlands And Their Climatic Conditions. *Arctic & Alpine Research*, 5, 99–113.

Lawrence, C., Beem-Miller, J., Hoyt, A., Monroe, G., Sierra, C., Stoner, S., Heckman, K., Blankinship, J., Crow, S., McNicol, G., & et al. (2019). An open source database for the synthesis of soil radiocarbon data: ISRaD version 1.0. *Earth System Science Data Discussions*, , 1–37doi:10.5194/essd-2019-55.

Lee, J., Hopmans, J.W., Rolston, D.E., Baer, S.G., & Six, J. (2009). Determining soil carbon stock changes: Simple bulk density corrections fail. *Agriculture, Ecosystems and Environment*, 134, 251–256. doi:10.1016/j.agee.2009.07.006.

Lenth, R. (2019). emmeans: Estimated Marginal Means, aka Least-Squares Means. URL: https://CRAN.R-project.org/package=emmeans. r package version 1.3.5.1.

Lettens, S., Van Orshoven, J., Van Wesemael, B., De Vos, B., & Muys, B. (2005). Stocks and fluxes of soil organic carbon for landscape units in Belgium derived from heterogeneous data sets for 1990 and 2000. *Geoderma*, 127, 11–23. doi:10.1016/j.geoderma.2004.11.001.

Leutner, B., Horning, N., & Schwalb-Willmann, J. (2019). RStoolbox: Tools for Remote Sensing Data Analysis. URL: https://CRAN.R-project.org/package=RStoolbox. r package version 0.2.6.

Levi, M.R., & Rasmussen, C. (2014). Covariate selection with iterative principal component analysis for predicting physical soil properties. *Geoderma*, 219–220, 46–57. doi:10.1016/j.geoderma.2013.12.013.

Liang, L. (2016). Beyond the Bioclimatic Law: Geographic adaptation patterns of temperate plant phenology. *Progress in Physical Geography*, 40, 811–834. doi:10.1177/0309133316656558.

Liang, Z., Chen, S., Yang, Y., Zhou, Y., & Shi, Z. (2019). High-resolution three-dimensional mapping of soil organic carbon in china: Effects of soilgrids products on national modeling. *Science of the Total Environment*, 685, 480–489. doi:10.1016/j.scitotenv.2019.05.332.

Liaw, A., & Wiener, M. (2002). Classification and regression by randomforest. *R News*, 2, 18–22. URL: https://CRAN.R-project.org/doc/Rnews/.

Ließ, M., Schmidt, J., & Glaser, B. (2016). Improving the spatial prediction of soil organic carbon stocks in a complex tropical mountain landscape by methodological specifications in machine learning approaches. *PLoS ONE*, 11, 1–22. doi:10.1371/journal.pone.0153673.

Link, W.A., & Eaton, M.J. (2012). On thinning of chains in MCMC. *Methods in Ecology and Evolution*, 3, 112–115. URL: https://besjournals.onlinelibrary.wiley.com/doi/abs/10.1111/j.2041-210X.2011.00131.x, doi:10.1111/j.2041-210X.2011.00131.x, arXiv:https://besjournals.onlinelibrary.wiley.com/doi/pdf/10.1111/j.2041-210X.2011.00131.x.

Liu, L., Wang, Z., Wang, Y., Zhang, Y., Shen, J., Qin, D., & Li, S. (2019). Trade-off analyses of multiple mountain ecosystem services along elevation, vegetation cover and precipitation gradients: A case study in the taihang mountains. *Ecological Indicators*, 103, 94–104. doi:10.1016/j.ecolind.2019.03.034.

López-Ramírez, S.M., Mayer, A., Sáenz, L., Muñoz-Villers, L.E., Holwerda, F., Looker, N., Schürz, C., Carter Berry, Z., Manson, R., Asbjornsen, H., Kolka, R., Geissert, D., & Lezama, C. (2021). A comprehensive calibration and validation of SWAT-T using local datasets, evapotranspiration and streamflow in a tropical montane cloud forest area with permeable substrate in central Veracruz, Mexico. *Journal of Hydrology*, 603, 126781. doi:10.1016/j.jhydrol.2021.126781.

López-Ramírez, S.M., Sáenz, L., Mayer, A., Muñoz-Villers, L.E., Asbjornsen, H., Berry, Z.C., Looker, N., Manson, R., & Gómez-Aguilar, L.R. (2020). Land use change effects on catchment streamflow response in a humid tropical montane cloud forest region, central Veracruz, Mexico. *Hydrological Processes*, 34, 3555–3570. doi:10.1002/hyp.13800.

Lunn, D., Barrett, J., Sweeting, M., & Thompson, S. (2013). Fully Bayesian hierarchical modelling in two stages, with application to meta-analysis. *Journal of the Royal Statistical Society: Series C (Applied Statistics)*, 62, 551–572. URL: https://rss.onlinelibrary.wiley.com/doi/abs/10.1111/rssc.12007, doi:10.1111/rssc.12007.

Lyttle, A., Yoo, K., Hale, C., Aufdenkampe, A., Sebestyen, S.D., Resner, K., & Blum, A. (2014). Impact of exotic earthworms on organic carbon sorption on mineral surfaces and soil carbon inventories in a northern hardwood forest. *Ecosystems*, 18, 16–29. doi:10.1007/s10021-014-9809-x.

von Lützow, M., & Kögel-Knabner, I. (2009). Temperature sensitivity of soil organic matter decomposition-what do we know? *Biology and Fertility of Soils*, 46, 1–15. doi:10.1007/s00374-009-0413-8.

Majumdar, A., Kaye, J., Gries, C., Hope, D., & Grimm, N. (2008). Hierarchical spatial modeling and prediction of multiple soil nutrients and carbon concentrations. *Communications in Statistics: Simulation and Computation*, 37, 434–453. doi:10.1080/03610910701792588.

Malhotra, A., Todd-Brown, K., Nave, L.E., Batjes, N.H., Holmquist, J.R., Hoyt, A.M., Iversen, C.M., Jackson, R.B., Lajtha, K., Lawrence, C., & et al. (2019). The landscape of soil carbon data: Emerging questions, synergies and databases. *Progress in Physical Geography*, 43, 707–719. doi:10.1177/0309133319873309.

Malone, B.P., McBratney, A.B., Minasny, B., & Laslett, G.M. (2009). Mapping continuous depth functions of soil carbon storage and available water capacity. *Geoderma*, 154, 138–152. doi:10.1016/j.geoderma.2009.10.007.

Martin, J., Looker, N., Hoylman, Z., Jencso, K., & Hu, J. (2017). Hydrometeorology organizes

intra-annual patterns of tree growth across time, space and species in a montane watershed. *New Phytologist*, 215, 1387–1398. doi:10.1111/nph.14668.

Marín-Castro, B.E., Geissert, D., Negrete-Yankelevich, S., & Gómez-Tagle Chávez, A. (2016). Spatial distribution of hydraulic conductivity in soils of secondary tropical montane cloud forests and shade coffee agroecosystems. *Geoderma*, 283, 57–67. doi:10.1016/j.geoderma.2016.08.002.

Marín-Spiotta, E., & Sharma, S. (2013). Carbon storage in successional and plantation forest soils: A tropical analysis. *Global Ecology and Biogeography*, 22, 105–117. doi:10.1111/j.1466-8238.2012.00788.x.

Marín-Spiotta, E., Swanston, C.W., Torn, M.S., Silver, W.L., & Burton, S.D. (2008). Chemical and mineral control of soil carbon turnover in abandoned tropical pastures. *Geoderma*, 143, 49–62. doi:10.1016/j.geoderma.2007.10.001.

Masiello, C.A., Chadwick, O.A., Southon, J., Torn, M.S., & Harden, J.W. (2004). Weathering controls on mechanisms of carbon storage in grassland soils. *Global Biogeochemical Cycles*, 18, 1–9. doi:10.1029/2004GB002219.

Massawe, B.H., Winowiecki, L., Meliyo, J.L., Mbogoni, J.D., Msanya, B.M., Kimaro, D., Deckers, J., Gulinck, H., Lyamchai, C., Sayula, G., & et al. (2017). Assessing drivers of soil properties and classification in the west usambara mountains, tanzania. *Geoderma Regional*, 11, 141–154. doi:10.1016/j.geodrs.2017.10.002.

Matus, F., Amigo, X., & Kristiansen, S.M. (2006). Aluminium stabilization controls organic carbon levels in Chilean volcanic soils. *Geoderma*, 132, 158–168. doi:10.1016/j.geoderma.2005.05.005.

McKeague, J.A., & Day, J.H. (1966). Dithionite- and oxalate-extractable Fe and Al as aids in differentiating various classes of soils. *Canadian Journal of Soil Science*, 46, 13–22. doi:10.4141/cjss66-003.

McNab, W.H. (1989). Terrain shape index: quantifying effect of minor landforms on tree height. *Forest Science*, 35, 91–104.

McNicol, G., Bulmer, C., D'Amore, D., Sanborn, P., Saunders, S., Giesbrecht, I., Arriola, S.G., Bidlack, A., Butman, D., & Buma, B. (2019). Large, climate-sensitive soil carbon stocks mapped with pedology-informed machine learning in the north pacific coastal temperate rainforest. *Environmental Research Letters*, 14. doi:10.1088/1748-9326/aaed52.

Medorio-García, H.P., Alarcón, E., Flores-Esteves, N., Montaño, N.M., & Perroni, Y. (2020). Soil carbon, nitrogen and phosphorus dynamics in sugarcane plantations converted from tropical dry forest. *Applied Soil Ecology*, 154, 103600. URL: https://doi.org/10.1016/j.apsoil.2020.103600, doi:10.1016/j.apsoil.2020.103600.

Meijer, E.L., & Buurman, P. (2003). Chemical trends in a perhumid soil catena on the Turrialba volcano (Costa Rica). *Geoderma*, 117, 185–201. doi:10.1016/S0016-7061(03)00122-8.

Meinshausen, N. (2006). Quantile regression forests. *Journal of Machine Learning Research*, 7, 983–999. doi:10.1016/j.jmva.2014.06.005.

Melaas, E.K., Friedl, M.A., & Zhu, Z. (2013). Detecting interannual variation in deciduous

broadleaf forest phenology using Landsat TM/ETM+ data. *Remote Sensing of Environment*, 132, 176–185.

Meybeck, M., Green, P., & Vörösmarty, C. (2001). A new typology for mountains and other relief classes: An application to global continental water resources and population distribution. *Mountain Research and Development*, 21, 34–45. doi:10.1659/0276-4741(2001)021[0034:ANTFMA]2.0.CO;2.

Meza Pérez, E. (1996). Estudio comparativo de las propiedades físicas e hídricas entre los andosoles de cultivo y bosque del Cofre de Perote, Estado de Veracruz, México. Master's thesis. Universidad Nacional Autónoma de México. Mexico City, Mexico.

Miller, B.A., Koszinski, S., Wehrhan, M., & Sommer, M. (2015). Impact of multi-scale predictor selection for modeling soil properties. *Geoderma*, 239, 97–106. doi:10.1016/j.geoderma.2014.09.018.

Miller, D.L., Roberts, D.A., Clarke, K.C., Lin, Y., Menzer, O., Peters, E.B., & McFadden, J.P. (2018). Gross primary productivity of a large metropolitan region in midsummer using high spatial resolution satellite imagery. *Urban Ecosystems*, 21, 831–850. doi:10.1007/s11252-018-0769-3.

Minasny, B., & Hartemink, A.E. (2011). Predicting soil properties in the tropics. *Earth-Science Reviews*, 106, 52–62. doi:10.1016/j.earscirev.2011.01.005.

Minasny, B., Malone, B.P., McBratney, A.B., Angers, D.A., Arrouays, D., Chambers, A., Chaplot, V., Chen, Z.S., Cheng, K., Das, B.S., & et al. (2017). Soil carbon 4 per mille. *Geoderma*, 292, 59–86. doi:10.1016/j.geoderma.2017.01.002.

Minda, T.T., van der Molen, M.K., Struik, P.C., Combe, M., Jiménez, P.A., Khan, M.S., & de Arellano, J.V.G. (2018). The combined effect of elevation and meteorology on potato crop dynamics: A 10-year study in the gamo highlands, ethiopia. *Agricultural and Forest Meteorology*, 262, 166–177. doi:10.1016/j.agrformet.2018.07.009.

Minor, J., Pearl, J.K., Barnes, M.L., Colella, T.R., Murphy, P.C., Mann, S., & Barron-Gafford, G.A. (2019). Critical zone science in the anthropocene: Opportunities for biogeographic and ecological theory and praxis to drive earth science integration. *Progress in Physical Geography: Earth and Environment*, , 030913331986426doi:10.1177/0309133319864268.

Mokondoko, P., Manson, R.H., Ricketts, T.H., & Geissert, D. (2018). Spatial analysis of ecosystem service relationships to improve targeting of payments for hydrological services. *PLoS ONE*, 13, 1–27. doi:10.1371/journal.pone.0192560.

Möller, M., Gerstmann, H., Gao, F., Dahms, T.C., & Förster, M. (2017). Coupling of phenological information and simulated vegetation index time series: Limitations and potentials for the assessment and monitoring of soil erosion risk. *Catena*, 150, 192–205. URL: http://dx.doi.org/10.1016/j.catena.2016.11.016, doi:10.1016/j.catena.2016.11.016.

Mora, J., Guerra, J., Armas-Herrera, C., Arbelo, C., & Rodríguez-Rodríguez, A. (2014). Storage and depth distribution of organic carbon in volcanic soils as affected by environmental and pedological factors. *Catena*, 123, 163–175. doi:10.1016/j.catena.2014.08.004.

Moreno-Casasola, P., López Rosas, H., Infante Mata, D., Peralta, L.A., Travieso-Bello, A.C., & Warner, B.G. (2009). Environmental and anthropogenic factors associated with coastal

wetland differentiation in la mancha, Veracruz, Mexico. *Plant Ecology*, 200, 37–52. doi:10.1007/s11258-008-9400-7.

Mulder, V.L., Lacoste, M., Richer-de Forges, A.C., Martin, M.P., & Arrouays, D. (2016). National versus global modelling the 3d distribution of soil organic carbon in mainland france. *Geoderma*, 263, 16–34. doi:10.1016/j.geoderma.2015.08.035.

Muñiz-Castro, M.A., Williams-Linera, G., & Martínez-Ramos, M. (2012). Dispersal mode, shade tolerance, and phytogeographical affinity of tree species during secondary succession in tropical montane cloud forest. *Plant Ecology*, 213, 339–353. doi:10.1007/s11258-011-9980-5.

Murty, D., Kirschbaum, M.U., Mcmurtrie, R.E., & Mcgilvray, H. (2002). Does conversion of forest to agricultural land change soil carbon and nitrogen? a review of the literature. *Global Change Biology*, 8, 105–123. doi:10.1046/j.1354-1013.2001.00459.x.

Muñoz-Villers, L., Geris, J., Alvarado-Barrientos, S., Holwerda, F., & Dawson, T. (2020). Coffee and shade trees show complementary use of soil water in a traditional agroforestry ecosystem. *Hydrology and Earth System Sciences*, 24, 1649–1668. doi:10.5194/hess-2019-329.

Muñoz-Villers, L., Holwerda, F., Gómez-Cárdenas, M., Equihua, M., Asbjornsen, H., Bruijnzeel, L., Marín-Castro, B., & Tobón, C. (2012). Water balances of old-growth and regenerating montane cloud forests in central Veracruz, Mexico. *Journal of Hydrology*, 462-463, 53–66. URL: http://linkinghub.elsevier.com/retrieve/pii/S002216941100117X, doi:10.1016/j.jhydrol.2011.01.062.

Muñoz-Villers, L.E., Geissert, D.R., Holwerda, F., & McDonnell, J.J. (2016). Factors influencing stream baseflow transit times in tropical montane watersheds. *Hydrology and Earth System Sciences*, 20, 1621–1635. doi:10.5194/hess-20-1621-2016.

Muñoz-Villers, L.E., & López-Blanco, J. (2008). Land use/cover changes using Landsat TM/ETM images in a tropical and biodiverse mountainous area of central-eastern Mexico. *International Journal of Remote Sensing*, 29, 71–93. doi:10.1080/01431160701280967.

Nagy, R.C., Porder, S., Brando, P., Davidson, E.A., Figueira, A.M.e., Neill, C., Riskin, S., & Trumbore, S. (2018). Soil carbon dynamics in soybean cropland and forests in Mato Grosso, Brazil. *Journal of Geophysical Research: Biogeosciences*, 123, 18–31. doi:10.1002/2017JG004269.

Nanko, K., Ugawa, S., Hashimoto, S., Imaya, A., Kobayashi, M., Sakai, H., Ishizuka, S., Miura, S., Tanaka, N., Takahashi, M., & et al. (2014). A pedotransfer function for estimating bulk density of forest soil in Japan affected by volcanic ash. *Geoderma*, 213, 36–45. doi:10.1016/j.geoderma.2013.07.025.

NASA JPL (2017). Nasa shuttle radar topography mission global 1 arc second [data set]. Available at https://doi.org/10.5067/MEaSUREs/SRTM/SRTMGL1.003 (2018-08-02).

Nave, L., Johnson, K., van Ingen, C., Agarwal, D., Humphrey, M., & Beekwilder, N. (2016). International Soil Carbon Network (ISCN) Database v3-1, URL: https://www.osti.gov/biblio/1305039, doi:10.17040/ISCN/1305039.

Negendank, J., Emmermann, R., Krawczyk, R., Mooser, F., Tobschall, H., & Werle, D. (1985).

Geological and geochemical investigations on the eastern trans-Mexican volcanic belt. *Geofísica Internacional*, 24, 477'575.

Negrete-Yankelevich, S., Cultid-Medina, C.A., Fuentes-Pangtay, T., Álvarez Sánchez, J., Cram, S., García-Pérez, J.A., Fragoso, C., Martinez-Romero, E., Rojas, P., Varela-Fregoso, L., & et al. (2020). Disentangling the effects of legacies from those of current land use on soil properties in los tuxtlas biosphere reserve, Mexico. *Applied Soil Ecology*, 153, 103578. doi:10.1016/j.apsoil.2020.103578.

Nelson, D., & Sommers, L. (1996). Total carbon, organic carbon, and organic matter, in: Methods of Soil Analysis. John Wiley Sons, Ltd. chapter 34, pp. 961–1010.

Neumann, M., Ukonmaanaho, L., Johnson, J., Benham, S., Vesterdal, L., Novotný, R., Verstraeten, A., Lundin, L., Thimonier, A., Michopoulos, P., & Hasenauer, H. (2018). Quantifying Carbon and Nutrient Input From Litterfall in European Forests Using Field Observations and Modeling. *Global Biogeochemical Cycles*, 32, 784–798. doi:10.1029/2017GB005825.

Nguyen, L.H., & Henebry, G.M. (2019). Characterizing land use/land cover using multisensor time series from the perspective of land surface phenology. *Remote Sensing*, 11. doi:10.3390/rs11141677.

Nolè, A., Rita, A., Ferrara, A.M.S., & Borghetti, M. (2018). Effects of a large-scale late spring frost on a beech (fagus sylvatica l.) dominated mediterranean mountain forest derived from the spatio-temporal variations of ndvi. *Annals of Forest Science*, 75, 1–11. doi:10.1007/s13595-018-0763-1.

Nottingham, A.T., Bååth, E., Reischke, S., Salinas, N., & Meir, P. (2019). Adaptation of soil microbial growth to temperature: Using a tropical elevation gradient to predict future changes. *Global Change Biology*, 25, 827–838. doi:10.1111/gcb.14502.

Nottingham, A.T., Whitaker, J., Turner, B.L., Salinas, N., Zimmermann, M., Malhi, Y., & Meir, P. (2015). Climate warming and soil carbon in tropical forests: Insights from an elevation gradient in the Peruvian Andes. *BioScience*, 65, 906–921. doi:10.1093/biosci/biv109.

Oliveras, I., Girardin, C., Doughty, C.E., Cahuana, N., Arenas, C.E., Oliver, V., Huaraca Huasco, W., & Malhi, Y. (2014). Andean grasslands are as productive as tropical cloud forests. *Environmental Research Letters*, 9. doi:10.1088/1748-9326/9/11/115011.

Palarea-Albaladejo, J., & Martin-Fernandez, J. (2015). zCompositions – R package for multivariate imputation of left-censored data under a compositional approach. *Chemometrics and Intelligent Laboratory Systems*, 143, 85–96. URL: http://dx.doi.org/10.1016/j.chemolab.2015.02.019.

Pansu, M., & Gautheyrou, J. (2006). pH Measurement. Springer Berlin Heidelberg, Berlin, Heidelberg. pp. 551–579. doi:10.1007/978-3-540-31211-6_15.

Parfitt, R.L. (2009). Allophane and imogolite: role in soil biogeochemical processes. *Clay Minerals*, 44, 135–155. doi:10.1180/claymin.2009.044.1.135.

Parikh, S.J., Goyne, K.W., Margenot, A.J., Mukome, F.N., & Calderón, F.J. (2014). Soil chemical insights provided through vibrational spectroscopy. volume 126.

Paré, L., & Gerez, P. (2012). Al filo del agua: cogestión de la subcuenca del río Pixquiac, Veracruz. doi:10.2307/40087391.

Paul, S., Veldkamp, E., & Flessa, H. (2008). Differential response of mineral-associated organic matter in tropical soils formed in volcanic ashes and marine Tertiary sediment to treatment with HCl, NaOCl, and Na4P2O7. *Soil Biology and Biochemistry*, 40, 1846–1855. doi:10.1016/j.soilbio.2008.03.008.

Pellerin, M., Delestrade, A., Mathieu, G., Rigault, O., & Yoccoz, N.G. (2012). Spring tree phenology in the Alps: Effects of air temperature, altitude and local topography. *European Journal of Forest Research*, 131, 1957–1965. doi:10.1007/s10342-012-0646-1.

Pelletier, J.D., Barron-Gafford, G.A., Breshears, D.D., Brooks, P.D., Chorover, J., Durcik, M., Harman, C.J., Huxman, T.E., Lohse, K.A., Lybrand, R., & et al. (2013). Coevolution of nonlinear trends in vegetation, soils, and topography with elevation and slope aspect: A case study in the sky islands of southern arizona. *Journal of Geophysical Research: Earth Surface*, 118, 741–758. doi:10.1002/jgrf.20046.

Peña-Ramírez, V., Vázquez-Selem, L., & Siebe, C. (2015). Rates of pedogenic processes in volcanic landscapes of late Pleistocene to Holocene age in Central Mexico. *Quaternary International*, 376, 19–33. doi:10.1016/j.quaint.2014.11.032.

Pinagé, E.R., Matricardi, E.A.T., Leal, F.A., & Pedlowski, M.A. (2016). Estimates of selective logging impacts in tropical forest canopy cover using RapidEye imagery and field data. *iForest*, 9, 461–468. doi:10.3832/ifor1534-008.

Ping, C.l., Michaelson, G.J., Stiles, C.A., & González, G. (2013). Soil characteristics , carbon stores , and nutrient distribution in eight forest types along an elevation gradient , eastern Puerto Rico. *Ecological Bulletins 54:*, 54:, 67–86.

Planet Team (2017). Planet application program interface: In space for life on earth. Available at https://api.planet.com (2019-07-01).

Plummer, M. (2019). rjags: Bayesian Graphical Models using MCMC. URL: https://CRAN.R-project.org/package=rjags. r package version 4-9.

Poeplau, C., Vos, C., & Don, A. (2017). Soil organic carbon stocks are systematically overestimated by misuse of the parameters bulk density and rock fragment content. *SOIL*, 3, 61–66. doi:10.5194/soil-2016-78.

Poggio, L., De Sousa, L.M., Batjes, N.H., Heuvelink, G.B., Kempen, B., Ribeiro, E., & Rossiter, D. (2021). Soilgrids 2.0: Producing soil information for the globe with quantified spatial uncertainty. *Soil*, 7, 217–240. doi:10.5194/soil-7-217-2021.

Ponette-González, A.G., Weathers, K.C., & Curran, L.M. (2010). Water inputs across a tropical montane landscape in Veracruz, Mexico: synergistic effects of land cover, rain and fog seasonality, and interannual precipitation variability. *Global Change Biology*, 16, 946–963. URL: http://doi.wiley.com/10.1111/j.1365-2486.2009.01985.x, doi:10.1111/j.1365-2486.2009.01985.x.

Ponette-González, A.G., & Fry, M. (2014). Enduring footprint of historical land tenure on modern land cover in eastern Mexico: Implications for environmental services programmes. *Area*, 46, 398–409. doi:10.1111/area.12125.

Powers, J.S., & Schlesinger, W.H. (2002). Relationships among soil carbon distributions and

biophysical factors at nested spatial scales in rain forests of northeastern Costa Rica. *Geoderma*, 109, 165–190. doi:10.1016/S0016-7061(02)00147-7.

Pribyl, D.W. (2010). A critical review of the conventional SOC to SOM conversion factor. *Geoderma*, 156, 75–83. URL: http://dx.doi.org/10.1016/j.geoderma.2010.02.003, doi:10.1016/j.geoderma.2010.02.003.

QGIS Development Team (2018). QGIS Geographic Information System. Open Source Geospatial Foundation. URL: http://qgis.osgeo.org.

R Core Team (2018). R: A Language and Environment for Statistical Computing. R Foundation for Statistical Computing. Vienna, Austria. URL: https://www.R-project.org/.

Rahbek, C., Borregaard, M.K., Colwell, R.K., Dalsgaard, B., Holt, B.G., Morueta-Holme, N., Nogues-Bravo, D., Whittaker, R.J., & Fjeldså, J. (2019). Humboldt's enigma: What causes global patterns of mountain biodiversity? *Science*, 365, 1108–1113. doi:10.1126/science.aax0149.

Ramcharan, A., Hengl, T., Nauman, T., Brungard, C., Waltman, S., Wills, S., & Thompson, J. (2018). Soil property and class maps of the conterminous United States at 100-meter spatial resolution. *Soil Science Society of America Journal*, 82, 186–201. doi:10.2136/sssaj2017.04.0122.

Rasmussen, C., Heckman, K., Wieder, W.R., Keiluweit, M., Lawrence, C.R., Berhe, A.A., Blankinship, J.C., Crow, S.E., Druhan, J.L., Hicks Pries, C.E., & et al. (2018). Beyond clay: towards an improved set of variables for predicting soil organic matter content. *Biogeochemistry*, 137, 297–306. doi:10.1007/s10533-018-0424-3.

Rasmussen, C., McGuire, L., Dhakal, P., & Pelletier, J.D. (2017). Coevolution of soil and topography across a semiarid cinder cone chronosequence. *Catena*, 156, 338–352. URL: http://linkinghub.elsevier.com/retrieve/pii/S0341816217301479, doi:10.1016/j.catena.2017.04.025.

Rasmussen, C., Pelletier, J.D., Troch, P.a., Swetnam, T.L., & Chorover, J. (2015). Quantifying topographic and vegetation effects on the transfer of energy and mass to the critical zone. *Vadose Zone Journal*, 14. doi:10.2136/vzj2014.07.0102.

Reed, B.C., Brown, J.F., VanderZee, D., Loveland, T.R., Merchant, J.W., & Ohlen, D.O. (1994). Measuring phenological variability from satellite imagery. *Journal of Vegetation Science*, 5, 703–714. doi:10.2307/3235884.

Reich, P.B. (1995). Phenology of tropical forests: patterns, causes, and consequences. *Canadian Journal of Botany*, 73, 164–174. doi:10.1139/b95-020.

Restrepo, C., & Alvarez, N. (2006). Landslides and their contribution to land-cover change in the mountains of Mexico and Central America. *Biotropica*, 38, 446–457. doi:10.1111/j.1744-7429.2006.00178.x.

Rodríguez, S.R., Morales-Barrera, W., Layer, P., & González-Mercado, E. (2010). A quaternary monogenetic volcanic field in the Xalapa region, eastern Trans-Mexican volcanic belt: Geology, distribution and morphology of the volcanic vents. *Journal of Volcanology and Geothermal Research*, 197, 149–166. URL: http://dx.doi.org/10.1016/j.jvolgeores.2009.08.003, doi:10.1016/j.jvolgeores.2009.08.003.

Rodríguez-Veiga, P., Carreiras, J., Smallman, T.L., Exbrayat, J.F., Ndambiri, J., Mutwiri, F., Nyasaka, D., Quegan, S., Williams, M., & Balzter, H. (2020). Carbon stocks and fluxes in kenyan forests and wooded grasslands derived from earth observation and model-data fusion. *Remote Sensing*, 12. doi:10.3390/RS12152380.

Rohart, F., Gautier, B., Singh, A., & Lê Cao, K.A. (2017). mixOmics: An R package for 'omics feature selection and multiple data integration. *PLoS Computational Biology*, 13, 1–19. doi:10.1371/journal.pcbi.1005752.

Romero Uribe, H.M. (2017). Cambios en el almacén de carbono y nitrógeno edáficos en diferentes tipos de uso de suelo y a diferentes profundidades, en el centro de Veracruz, México. Master's thesis. Instituto de Ecología, A.C.. Xalapa, Veracruz, Mexico.

Rosenstock, T.S., Mpanda, M., Rioux, J., Aynekulu, E., Kimaro, A.A., Neufeldt, H., Shepherd, K.D., & Luedeling, E. (2014). Targeting conservation agriculture in the context of livelihoods and landscapes. *Agriculture, Ecosystems and Environment*, 187, 47–51. doi:10.1016/j.agee.2013.11.011.

Rossignol, J.P., Campos C, A., & Quantin, P. (1992). Las condiciones regionales de desarrollo de los tepetates en la zona Xalapa-Coatepec, Veracruz, México: Localización, condiciones ambientales y características generales, in: Zebrowski, C., Prat, C., Etchevers Barra, J., H.M., A.R., & Miranda, M.M. (Eds.), Terra. Suelos Volcanicos Endurecidos: Simposio Internacional. Mexico City, Mexico, pp. 233–240.

Rossiter, D.G., & Bouma, J. (2018). A new look at soil phenoforms – definition, identification, mapping. *Geoderma*, 314, 113–121. doi:10.1016/j.geoderma.2017.11.002.

Rovira, P., Sauras, T., Salgado, J., & Merino, A. (2015). Towards sound comparisons of soil carbon stocks: A proposal based on the cumulative coordinates approach. *Catena*, 133, 420–431. doi:10.1016/j.catena.2015.05.020.

Rozendaal, D.M., Bongers, F., Aide, T.M., Alvarez-Dávila, E., Ascarrunz, N., Balvanera, P., Becknell, J.M., Bentos, T.V., Brancalion, P.H., Cabral, G.A., & et al. (2019). Biodiversity recovery of neotropical secondary forests. *Science Advances*, 5. doi:10.1126/sciadv.aau3114.

Sanderman, J., Hengl, T., & Fiske, G.J. (2017). Soil carbon debt of 12,000 years of human land use. *Proceedings of the National Academy of Sciences of the United States of America*, 114, 9575–9580. doi:10.1073/pnas.1706103114.

Sarmiento, G. (1986). Ecological features of climate in high tropical mountains, in: Vuilleumier, F., & Monasterio, M. (Eds.), High Altitude Tropical Biogeography. Oxford University Press, Oxford, pp. 11–45.

Scheffler, D., Hollstein, A., Diedrich, H., Segl, K., & Hostert, P. (2017). AROSICS: An automated and robust open-source image co-registration software for multi-sensor satellite data. *Remote Sensing*, 9. doi:10.3390/rs9070676.

Schulp, C.J., & Verburg, P.H. (2009). Effect of land use history and site factors on spatial variation of soil organic carbon across a physiographic region. *Agriculture, Ecosystems and Environment*, 133, 86–97. doi:10.1016/j.agee.2009.05.005.

Senf, C., Pflugmacher, D., Heurich, M., & Krueger, T. (2017). A Bayesian hierarchical model

for estimating spatial and temporal variation in vegetation phenology from Landsat time series. *Remote Sensing of Environment*, 194, 155–160.

Sequeira, C.H., Wills, S.A., Seybold, C.A., & West, L.T. (2014). Predicting soil bulk density for incomplete databases. *Geoderma*, 213, 64–73. doi:10.1016/j.geoderma.2013.07.013.

Servicio Geológico Mexicano (2007a). Carta geológico-minera: Perote, e14-b26, Veracruz y puebla. Available at https://mapserver.sgm.gob.mx/Cartas_Online/geologia/1917_E14-B26_GM.pdf (2020-08-29).

Servicio Geológico Mexicano (2007b). Carta geológico-minera: Xalapa, e14-b27, Veracruz. Available at https://mapserver.sgm.gob.mx/Cartas_Online/geologia/1936_E14-B27_GM.pdf (2020-08-29).

Servicio Geológico Mexicano (2014). Carta geológico-minera: Ciudad cardel (josé cardel), e14-b38, Veracruz. Available at https://mapserver.sgm.gob.mx/Cartas_Online/geologia/1956_E14-B38_GM.pdf (2020-08-29).

Servicio Meterológico Nacional (2017). Datos climáticos diarios del CLICOM del SMN a través de su plataforma web del CICESE. Available at http://clicom-mex.cicese.mx (2018-10-30).

Shen, H., & Huang, J.Z. (2008). Sparse principal component analysis via regularized low rank matrix approximation. *Journal of Multivariate Analysis*, 99, 1015–1034. doi:10.1016/j.jmva.2007.06.007.

Siebert, L., & Carrasco-Núñez, G. (2002). Late-Pleistocene to precolumbian behind-the-arc mafic volcanism in the eastern Mexican Volcanic Belt; implications for future hazards. *Journal of Volcanology and Geothermal Research*, 115, 179–205. doi:10.1016/S0377-0273(01)00316-X.

Sierra, C.A., Müller, M., Metzler, H., Manzoni, S., & Trumbore, S.E. (2017). The muddle of ages, turnover, transit, and residence times in the carbon cycle. *Global Change Biology*, 23, 1763–1773. doi:10.1111/gcb.13556.

Sierra, C.A., & Müller, M. (2015). A general mathematical framework for representing soil organic matter dynamics. *Ecological Monographs*, 85, 505–524. doi:10.1890/15-0361.1.

Sierra, J., & Causeret, F. (2018). Changes in soil carbon inputs and outputs along a tropical altitudinal gradient of volcanic soils under intensive agriculture. *Geoderma*, 320, 95–104. doi:10.1016/j.geoderma.2018.01.025.

Silatsa, F.B., Yemefack, M., Tabi, F.O., Heuvelink, G.B., & Leenaars, J.G. (2020). Assessing countrywide soil organic carbon stock using hybrid machine learning modelling and legacy soil data in cameroon. *Geoderma*, 367, 114260. doi:10.1016/j.geoderma.2020.114260.

Slessarev, E., Feng, X., Bingham, N., & Chadwick, O. (2019). Landscape age as a major control on the geography of soil weathering. *Global Biogeochemical Cycles*, , 2019GB006266doi:10.1029/2019GB006266.

Sollins, P., & Gregg, J.W. (2017). Soil organic matter accumulation in relation to changing soil volume, mass, and structure: Concepts and calculations. *Geoderma*, 301, 60–71. doi:10.1016/j.geoderma.2017.04.013.

Steber, A., Brooks, K., Perry, C.H., & Kolka, R. (2007). Surface compaction estimates and soil

sensitivity in Aspen stands of the Great Lakes States. *Northern Journal of Applied Forestry*, 24, 276–281.

Stewart, C.E., Paustian, K., Conant, R.T., Plante, A.F., & Six, J. (2007). Soil carbon saturation: Concept, evidence and evaluation. *Biogeochemistry*, 86, 19–31. doi:10.1007/s10533-007-9140-0.

Stewart, V., Adams, W., & Abdulla, H. (1970). Quantitative pedological studies on soils derived from Silurian mudstones. *Journal of Soil Science*, 21, 248–255. doi:10.1111/j.1365-2389.1970.tb01174.x.

Stocker, B.D., Feissli, F., Strassmann, K.M., Spahni, R., & Joos, F. (2014). Past and future carbon fluxes from land use change, shifting cultivation and wood harvest. *Tellus, Series B: Chemical and Physical Meteorology*, 66. doi:10.3402/tellusb.v66.23188.

Stratoulias, D., Tolpekin, V., de By, R., Zurita-Milla, R., Retsios, V., Bijker, W., Hasan, M., & Vermote, E. (2017). A Workflow for Automated Satellite Image Processing: from Raw VHSR Data to Object-Based Spectral Information for Smallholder Agriculture. *Remote Sensing*, 9, 1048. URL: http://www.mdpi.com/2072-4292/9/10/1048, doi:10.3390/rs9101048.

Streher, A.S., Sobreiro, J.F.F., Morellato, L.P.C., & Silva, T.S.F. (2017). Land Surface Phenology in the Tropics: The Role of Climate and Topography in a Snow-Free Mountain. *Ecosystems*, 20, 1436'1453. doi:10.1007/s10021-017-0123-2.

Stuiver, M., & Polach, H.A. (1977). Discussion: reporting of ^{14}C data. *Radiocarbon*, 19, 355–363.

Szatmári, G., Pirkó, B., Koós, S., Laborczi, A., Bakacsi, Z., Szabó, J., & Pásztor, L. (2019). Spatio-temporal assessment of topsoil organic carbon stock change in Hungary. *Soil and Tillage Research*, 195, 104410. doi:10.1016/j.still.2019.104410.

Sánchez-González, A., Octavio-Aguilar, P., Barrientos-Lozano, L., & Meerow, A.W. (2019). Effect of elevation strata on morphological variation of two agave species with different niche amplitude. *International Journal of Plant Sciences*, 180, 892–901. doi:10.1086/703577.

Takahashi, T., & Dahlgren, R.A. (2016). Nature, properties and function of aluminum-humus complexes in volcanic soils. *Geoderma*, 263, 110–121. doi:10.1016/j.geoderma.2015.08.032.

Tashi, S., Singh, B., Keitel, C., & Adams, M. (2016). Soil carbon and nitrogen stocks in forests along an altitudinal gradient in the eastern Himalayas and a meta-analysis of global data. *Global Change Biology*, 22, 2255–2268. doi:10.1111/gcb.13234.

Tateno, R., Tatsumi, C., Nakayama, M., Takahashi, K., Kerfahi, D., & Adams, J. (2019). Temperature effects on the first three years of soil ecosystem development on volcanic ash. *Catena*, 172, 1–10. doi:10.1016/j.catena.2018.08.009.

Taylor-Rodriguez, D., Finley, A., Datta, A., Babcock, C., Andersen, H., Cook, B., Morton, D., & Banerjee, S. (2019). Spatial factor models for high-dimensional and large spatial data: An application in forest variable mapping. *Statistica Sinica*, 29, 1155–1180. doi:10.5705/ss.202018.0005.

Teillet, P., Guindon, B., & Goodenough, D. (1982). On the slope-aspect correction of multispectral scanner data. *Canadian Journal of Remote Sensing*, 8, 84–106.

Tewes, A., Hoffmann, H., Nolte, M., Krauss, G., Schäfer, F., Kerkhoff, C., & Gaiser, T. (2020).

How do methods assimilating sentinel-2-derived lai combined with two different sources of soil input data affect the crop model-based estimation of wheat biomass at sub-field level? *Remote Sensing*, 12. doi:10.3390/rs12060925.

Tifafi, M., Guenet, B., & Hatté, C. (2018). Large Differences in Global and Regional Total Soil Carbon Stock Estimates Based on SoilGrids, HWSD, and NCSCD: Intercomparison and Evaluation Based on Field Data From USA, England, Wales, and France. *Global Biogeochemical Cycles*, 32, 42–56. doi:10.1002/2017GB005678.

Tigges, J., Lakes, T., & Hostert, P. (2013). Urban vegetation classification: Benefits of multitemporal RapidEye satellite data. *Remote Sensing of Environment*, 136, 66–75. doi:10.1016/j.rse.2013.05.001.

Toledo-Garibaldi, M., & Williams-Linera, G. (2014). Tree diversity patterns in successive vegetation types along an elevation gradient in the mountains of eastern Mexico. *Ecological Research*, 29, 1097–1104. doi:10.1007/s11284-014-1196-4.

Trinh, T., Kavvas, M.L., Ishida, K., Ercan, A., Chen, Z.Q., Anderson, M.L., Ho, C., & Nguyen, T. (2018). Integrating global land-cover and soil datasets to update saturated hydraulic conductivity parameterization in hydrologic modeling. *Science of the Total Environment*, 631–632, 279–288. doi:10.1016/j.scitotenv.2018.02.267.

Tsai, C.C., Chen, Z.S., Kao, C.I., Ottner, F., Kao, S.J., & Zehetner, F. (2010). Pedogenic development of volcanic ash soils along a climosequence in northern taiwan. *Geoderma*, 156, 48–59. doi:10.1016/j.geoderma.2010.01.007.

Tsui, C.C., Tsai, C.C., & Chen, Z.S. (2013). Soil organic carbon stocks in relation to elevation gradients in volcanic ash soils of Taiwan. *Geoderma*, 209–210, 119–127. doi:10.1016/j.geoderma.2013.06.013.

Turek, M.E., de Jong van Lier, Q., & Armindo, R.A. (2020). Estimation and mapping of field capacity in Brazilian soils. *Geoderma*, 376, 114557. doi:10.1016/j.geoderma.2020.114557.

Turner, M.G., Donato, D.C., & Romme, W.H. (2012). Consequences of spatial heterogeneity for ecosystem services in changing forest landscapes: priorities for future research. *Landscape Ecology*, 28, 1081–1097. doi:10.1007/s10980-012-9741-4.

Vacca, S., Capra, G.F., Coppola, E., Rubino, M., Madrau, S., Colella, A., Langella, A., & Buondonno, A. (2009). From andic non-allophanic to non-andic allophanic inceptisols on alkaline basalt in mediterranean climate. a toposequence study in the marghine district (sardinia, italy). *Geoderma*, 151, 157–167. doi:10.1016/j.geoderma.2009.03.024.

Vázquez Ramírez, J. (2014). Fenología reproductiva de las comunidades vegetales del parque nacional Cofre de Perote, Veracruz, México. Master's thesis. Universidad Veracruzana. Xalapa, Veracruz, Mexico.

Veldkamp, E., Schmidt, M., Powers, J.S., & Corre, M.D. (2020). Deforestation and reforestation impacts on soils in the tropics. *Nature Reviews Earth Environment*, doi:10.1038/s43017-020-0091-5.

Verde, J.R., Camps Arbestain, M., & Macías, F. (2005). Expression of andic properties in soils from Galicia (NW Spain) under forest and agricultural use. *European Journal of Soil Science*, 56, 53–63. doi:10.1111/j.1365-2389.2004.00651.x.

Vermote, E.F., Tanre, D., Deuze, J.L., Herman, M., & Morcette, J.. (1997). Second simulation of the satellite signal in the solar spectrum, 6S: an overview. *IEEE Transactions on Geoscience and Remote Sensing*, 35, 675–686.

Vitasse, Y., Signarbieux, C., & Fu, Y.H. (2018). Global warming leads to more uniform spring phenology across elevations. *Proceedings of the National Academy of Sciences of the United States of America*, 115, 1004–1008. doi:10.1073/pnas.1717342115.

Vizcaíno-Bravo, Q., Williams-Linera, G., & Asbjornsen, H. (2020). Biodiversity and carbon storage are correlated along a land use intensity gradient in a tropical montane forest watershed, Mexico. *Basic and Applied Ecology*, 44, 24 – 34. URL: http://www.sciencedirect.com/science/article/pii/S1439179120300013, doi:https://doi.org/10.1016/j.baae.2019.12.004.

Vogel, J.S., Nelson, D.E., & Southon, J.R. (1987). ^{14}C background levels in an accelerator mass spectrometry system. *Radiocarbon*, 29, 323–323.

Vogelmann, H.W. (1973). Fog precipitation in the cloud forests of eastern Mexico. *Bioscience*, 23, 96–100. doi:10.2307/1296569.

Von Thaden, J., Manson, R.H., Congalton, R.G., López-Barrera, F., & Jones, K.W. (2021). Evaluating the environmental effectiveness of payments for hydrological services in Veracruz, méxico: A landscape approach. *Land Use Policy*, 100. doi:10.1016/j.landusepol.2020.105055.

Von Thaden, J., Manson, R.H., Congalton, R.G., López-Barrera, F., & Salcone, J. (2019). A regional evaluation of the effectiveness of Mexico's payments for hydrological services. *Regional Environmental Change*, 19, 1751–1764. doi:10.1007/s10113-019-01518-3.

Waldman, K.B., Vergopolan, N., Attari, S.Z., Sheffield, J., Estes, L.D., Caylor, K.K., & Evans, T.P. (2019). Cognitive biases about climate variability in smallholder farming systems in Zambia. *Weather, Climate, and Society*, 11, 369–383. doi:10.1175/WCAS-D-18-0050.1.

Walkley, A., & Black, I. (1934). An examination of the Degtjareff method for determining soil organic matter and a proposed modification of the chromic acid titration method. *Soil Science*, 37, 29–38.

Wang, X., Dannenberg, M.P., Yan, D., Jones, M.O., Kimball, J.S., Moore, D.J.P., van Leeuwen, W.J.D., Didan, K., & Smith, W.K. (2020). Globally consistent patterns of asynchrony in vegetation phenology derived from optical, microwave, and fluorescence satellite data. *Journal of Geophysical Research: Biogeosciences*, 125, e2020JG005732. URL: https://agupubs.onlinelibrary.wiley.com/doi/abs/10.1029/2020JG005732, doi:https://doi.org/10.1029/2020JG005732, arXiv:https://agupubs.onlinelibrary.wiley.com/doi/pdf/10.1029/2020JG005732. e2020JG005732 2020JG005732.

Ward, A., Dargusch, P., Thomas, S., Liu, Y., & Fulton, E.A. (2014). A global estimate of carbon stored in the world's mountain grasslands and shrublands, and the implications for climate policy. *Global Environmental Change*, 28, 14–24. doi:10.1016/j.gloenvcha.2014.05.008.

Waring, R.H., Coops, N.C., Fan, W., & Nightingale, J.M. (2006). MODIS enhanced vegetation index predicts tree species richness across forested ecoregions in the contiguous U.S.A. *Remote Sensing of Environment*, 103, 218–226. doi:10.1016/j.rse.2006.05.007.

Wendt, J.W., & Hauser, S. (2013). An equivalent soil mass procedure for monitoring soil organic carbon in multiple soil layers. *European Journal of Soil Science*, 64, 58–65. doi:10.1111/ejss.12002.

Whitaker, J., Ostle, N., Nottingham, A.T., Ccahuana, A., Salinas, N., Bardgett, R.D., Meir, P., & Mcnamara, N.P. (2014). Microbial community composition explains soil respiration responses to changing carbon inputs along an andes-to-amazon elevation gradient. *Journal of Ecology*, 102, 1058–1071. doi:10.1111/1365-2745.12247.

White, M.A., de Beurs, K.M., Didan, K., Inouye, D.W., Richardson, A.D., Jensen, O.P., O'Keefe, J., Zhang, G., Nemani, R.R., van Leeuwen, W.J., Brown, J.F., de Wit, A., Schaepman, M., Lin, X., Dettinger, M., Bailey, A.S., Kimball, J., Schwartz, M.D., Baldocchi, D.D., Lee, J.T., & Lauenroth, W.K. (2009). Intercomparison, interpretation, and assessment of spring phenology in North America estimated from remote sensing for 1982-2006. *Global Change Biology*, 15, 2335–2359. doi:10.1111/j.1365-2486.2009.01910.x.

Williams-Linera, G. (1997). Phenology of Deciduous and Broadleaved-Evergreen Tree Species in a Mexican Tropical Lower Montane Forest. *Global Ecology and Biogeography Letters*, 6, 115–127.

Williams-Linera, G. (2000). Leaf demography and leaf traits of temperate-deciduous and tropical evergreen-broadleaved trees in a Mexican montane cloud forest. *Plant Ecology*, 149, 233–244. doi:10.1023/A:1026508610236.

Williams-Linera, G., Manson, R., & Isunza-Vera, E. (2002). La fragmentación del bosque mesófilo de montaña y patrones de uso del suelo en la región oeste de Xalapa, Veracruz, México. *Madera y Bosques*, 8, 73–89.

Williams-Linera, G., Toledo-Garibaldi, M., & Hernández, C.G. (2013). How heterogeneous are the cloud forest communities in the mountains of central Veracruz, Mexico? *Plant Ecology*, 214, 685–701. doi:10.1007/s11258-013-0199-5.

Wilson, A.M., & Jetz, W. (2016). Remotely sensed high-resolution global cloud dynamics for predicting ecosystem and biodiversity distributions. *PLoS Biology*, 14, 1–20. doi:10.1371/journal.pbio.1002415.

Wood, S.N. (2003). Thin-plate regression splines. *Journal of the Royal Statistical Society (B)*, 65, 95–114.

Wood, S.N. (2011). Fast stable restricted maximum likelihood and marginal likelihood estimation of semiparametric generalized linear models. *Journal of the Royal Statistical Society (B)*, 73, 3–36.

WRB, I.W.G. (2007). World Reference Base for Soil Resources 2006, first update 2007.

Xia, H., Qin, Y., Feng, G., Meng, Q., Cui, Y., Song, H., Ouyang, Y., & Liu, G. (2019). Forest phenology dynamics to climate change and topography in a geographic and climate transition zone: The Qinling Mountains in Central China. *Forests*, 10. doi:10.3390/f10111007.

Yadav, V., Malanson, G.P., Bekele, E., & Lant, C. (2009). Modeling watershed-scale sequestration of soil organic carbon for carbon credit programs. *Applied Geography*, 29, 488–500. doi:10.1016/j.apgeog.2009.04.001.

Yang, F., Zhang, G.L., Yang, J.L., Li, D.C., Zhao, Y.G., Liu, F., Yang, R.M., & Yang, F. (2014).

Organic matter controls of soil water retention in an alpine grassland and its significance for hydrological processes. *Journal of Hydrology*, 519, 3086–3093. URL: http://linkinghub.elsevier.com/retrieve/pii/S002216941400849X, doi:10.1016/j.jhydrol.2014.10.054.

Yang, S., Cammeraat, E., Jansen, B., den Haan, M., van Loon, E., & Recharte, J. (2018). Soil organic carbon stocks controlled by lithology and soil depth in a peruvian alpine grassland of the andes. *Catena*, 171, 11–21. doi:10.1016/j.catena.2018.06.038.

Zeilhofer, P., Sanches, L., Vourlitis, G.L., & De Andrade, N.L.R. (2012). Seasonal variations in litter production and its relation with MODIS vegetation indices in a semi-deciduous forest of Mato Grosso. *Remote Sensing Letters*, 3, 1–9. doi:10.1080/01431161.2010.523025.

Zeng, L., Wardlow, B.D., Xiang, D., Hu, S., & Li, D. (2020). A review of vegetation phenological metrics extraction using time-series, multispectral satellite data. *Remote Sensing of Environment*, 237, 111511. URL: https://doi.org/10.1016/j.rse.2019.111511, doi:10.1016/j.rse.2019.111511.

Zhang, X., Friedl, M.A., Schaaf, C.B., Strahler, A.H., Hodges, J.C., Gao, F., Reed, B.C., & Huete, A. (2003). Monitoring vegetation phenology using MODIS. *Remote Sensing of Environment*, 84, 471–475. doi:10.1016/S0034-4257(02)00135-9.

Zhou, Y., Webster, R., Viscarra Rossel, R.A., Shi, Z., & Chen, S. (2019). Baseline map of soil organic carbon in tibet and its uncertainty in the 1980s. *Geoderma*, 334, 124–133. doi:10.1016/j.geoderma.2018.07.037.

Zhu, W., Tian, H., Xu, X., Pan, Y., Chen, G., & Lin, W. (2012). Extension of the growing season due to delayed autumn over mid and high latitudes in North America during 1982-2006. *Global Ecology and Biogeography*, 21, 260–271. doi:10.1111/j.1466-8238.2011.00675.x.

Zinke, P., Stangenberger, A., Post, W., & Olson, J. (1986). Worldwide soil carbon and nitrogen data. NDP-018, Carbon Dioxide Information Center, Oak Ridge National Laboratory. Available at https://data.ess-dive.lbl.gov/view/doi:10.3334/CDIAC/LUE.NDP018.

Zomer, R.J., Bossio, D.A., Sommer, R., & Verchot, L.V. (2017). Global sequestration potential of increased organic carbon in cropland soils. *Scientific Reports*, 7, 1–8. doi:10.1038/s41598-017-15794-8.